Bjørn Rune Sørås Rogne

Nanomechanical Testing of Iron and Steel

Thesis for the degree of Philosophiae Doctor

Trondheim, November 2014

Norwegian University of Science and Technology
Faculty of Engineering Science and Technology
Department of Engineering Design and Materials

NTNU – Trondheim
Norwegian University of
Science and Technology

NTNU
Norwegian University of Science and Technology

Thesis for the degree of Philosophiae Doctor

Faculty of Engineering Science and Technology
Department of Engineering Design and Materials

ISBN 978-82-326-0590-3 (printed ver.)
ISBN 978-82-326-0591-0 (electronic ver.)
ISSN 1503-8181

Doctoral theses at NTNU, 2014:339

Printed by NTNU-trykk

Preface

This doctoral thesis is submitted to the Norwegian University of Science and Technology (NTNU) for the degree of *Philosophiæ Doctor*. The work explores the nanomechanical properties of iron and steel by means of nano- and micro-scaled pillars which are loaded in compression. The thesis is comprised of an introductory section and three research papers that were published or submitted for publication in international journals.

This work was supported by the Department of Engineering Design and Materials (IPM), NTNU. The Research Council of Norway is acknowledged for the support to the Norwegian Micro- and Nano-Fabrication Facility, NorFab (Contract No.197411/V30), and for funding through the Petromaks Programme (Contract No.187389/S30). The author would also like to acknowledge financial support from ENI, Statoil, Total, Scana Steel Stavanger, JFE Steel, Nippon Steel Corporation, Brück Pipeconnections, Miras Grotnes, Bredero Shaw, Trelleborg, GE Oil and Gas, Aker Solutions and Technip as industrial partners in the Petromaks Programme.

The work was carried out in the NTNU NanoLab, Nanomechanical laboratory (IPM, NTNU) and EM lab (Department of Materials Science and Engineering, NTNU). The work started August 2010 under the supervision of Prof. Christian Thaulow (IPM, NTNU, Trondheim), Dr. Erling Østby[1] (DNV, Materials Laboratory, Høvik) and Prof. Afrooz Barnoush[2] (IPM, NTNU).

Bjørn Rune Sørås Rogne

Trondheim, December 2014

---

[1] E. Østby was formerly employed in SINTEF Materials and Chemistry, Department of Materials Integrity and Welding, Trondheim, Norway.

[2] A. Barnoush was formerly employed in Saarland University, Materials Science and Methods, Saarbrücken, Germany.

Abstract

In this thesis the mechanical properties of iron and steel nano- and micro-pillars were investigated. The pillars were machined with focused ion beam (FIB) milling and subsequently loaded in compression by a nanoindenter equipped with a flat-punch indenter. Two types of materials were tested:

- Martensite and retained austenite containing constituents (M–A constituents or M-A phases) formed in high strength low alloy steel after weld thermal simulation.
- 99.99% pure iron that was annealed to produce sufficiently large grains for producing single crystal pillars.

The compressive flow curves of the M–A containing pillars were obtained and the yield stresses were between 0.8–1.2 GPa. The scatter in results, experimental challenges, unknown underlying microstructure and the desire for a fundamental understanding directed the experiments to be conducted on ferritic iron. Three aspects were investigated:

- Quantification of the pillar size and strength relation.
- The type of operating slip system, determined from slip traces at the pillars' surface.
- The orientation dependency of the resolved shear stress.

The flow curves of iron showed characteristic features similar to those previously reported for bcc metals. The majority of slip traces, or slip bands, on the pillars' surface followed the $\{110\}\langle 111\rangle$ family of slip systems. The resolved shear stress revealed an orientation dependent relation, where pillar size and strain appear to have little effect. The observed twinning–antitwinning asymmetry was stronger than expected from previous experiments on mm-sized samples.

In the introductory part to the appended paper collection, the basis of the motivating background and objectives are described. Furthermore, a bacground to the material, main experimental techniques and the experimental observations during the pillar compression experiments are given.

Acknowledgements

During my PhD studies at NTNU many people have been important. I would like to use this opportunity to express my gratitude to supervisors, colleges, friends and family. The opportunity to start on a PhD study was brought to my attention during my master's degree by my supervisor Prof. Christian Thaulow. He has been of vital importance with his valuable ideas and thoughts throughout my work. I am especially thankful for his ability to balance high and explicit expectations against motivating, inspiring and sometimes crazy ideas. I greatly appreciate the support received from my co-supervisors Prof. Afrooz Barnoush and Dr. Erling Østby. Prof. Barnoush has given me valuable assistance in theoretical and experimental matters. His knowledge within theory and thoroughness when conducting experiments are highly appreciated. Dr. Østby has given me important input and insight on how to see the link between real industrial problems and experimental work. In addition to my formal supervisors I would like to thank Prof. Odd Magne Akselsen. Together with Dr. Østby, Prof. Akselsen has been an important and appreciated contact person at SINTEF providing valuable consultation and advice.

A special thanks goes to all my friends and colleagues at NTNU, particularly Antonio Alvaro, Masoud Asgari, Adina Başa, Christer Ersland, Håkon Gundersen, Nousha Kheradmand, Inga Ringdalen, Jørn Skogsrud, Sindre Bjørnøy, Robin Brenden, Kristine Greinan, Anette Hagen, Veronica Haugen, Jonatan Kuipers and Marius Vebner. You have all inspired me, given me advice, challenged me and made me feel good at work.

I am grateful for having a wonderful group of friends, some of which I have known since pre-kindergarten. I owe a lot to my close friends from home, Ingebrikt, Eivind, Lasse Rune, Kenneth, Martin, and all the others from “Hildregjengen”. Each and every one of you has always been an important social support throughout my life, with no exception during my PhD study. I would like to use this opportunity to thank you for

who you are and for your unique way of inspiring me. I truly appreciate that most of us have settled in Trondheim.

I would like to thank my family for all their love and encouragement. I am fortunate to have such wonderful parents, mum Margun Bente and dad Leif Arne, who raised me to dare to make my own decisions and always being there for me. To my brother, Bård Håkon, and sister Elbjør Alise, a sincere thank you for all your support and for challenging me. Thank you for always taking the blame when we were kids.

To my dearest, closest and newest family: you are the best! My soul mate Monica ♡, thank you for always being there, for your endless patience, for counselling and for helping me out with the writing process. I promise that I will never do a PhD again. Our sweet little girl Leah Aurora brought new perspectives in life with her curiosity for life and radiant energy. You are the most open minded researcher I have ever met. However, sometime I questions the way you document your research methods. To Monica's parents, Vigdis and John Ola, thank you for helping out with baby-sitting Leah, everyday challenges and relaxing weekends in Lensvik.

Bjørn Rune Sørås Rogne

Contents

Chapter 1

Introduction

Today iron and steel are widely used in construction and other applications. Enhanced mechanical properties, without the use of expensive alloying elements, can reduce the amount of steel used in constructions. The weight savings give huge economical and environmental benefits.

Iron, in its pure form, is generally weak in strength, with a yield stress typically around 20–30 MPa [1, 2], and has the ability to withstand large deformations. Those properties can be changed by alloying the iron with the appropriate alloying elements and applying the correct heat treatment and mechanical history. Thus, the mechanical properties can become ductile or strong. Modern steels can have a yield stress in excess of 2 GPa or withstand as much as 70% elongation. However, utilisation of extreme properties usually come with a cost: expensive alloying elements and complicated manufacturing processes. Additionally, most of the steels do not have a combination of both high strength and high ductility.

Modern steels obtain their strength and ductility from strengthening mechanisms in the microstructure, which operate at different length scales. Microstructural components, such as dislocation entanglements, solute atoms, precipitates and grain boundaries, hinder and restrict the movement of dislocations. Hence, the resistance to plastic flow, or the materials strength, increases. The details of the plastic deformation of complex microstructures cannot be fully understood and evaluated during traditional material testing at large scale, *e.g.*, mm-sized samples. Therefore, there is a need to explore the mechanical properties of the material at the length scale where the deformation mechanisms operate.

The mechanical properties of steels are, however, not only a consequence of the alloying elements, heat treatment and mechanical history. One example is tensile experiments of μm-sized iron whiskers, thin single crystal fibres, which have shown yield stresses up to 11 GPa [3]. The high strength is obtained when the whiskers lack defects from where deformation can initiate. The plasticity is obtained when fresh dislocations nucleate at the surface at much higher stresses. The potential strength of iron, and other metals, is much higher than utilised in today's engineering materials. An increased understanding of how the deformation mechanisms work can drive the development of tomorrow's materials towards strong, ductile and cost efficient materials. It can also form the basis for new nano-inspired materials and structures.

The advance in nanotechnology, with new equipments and test methods, open up for new and innovative ways of exploring materials. The material can be mechanically characterised at different length scales to evaluate the contributions from the microstructural building blocks. Local mechanical properties can be used as direct input in microstructure based models and numerical simulations, or to validate computational simulations such as dislocation dynamics and molecular dynamic simulations. The experimental observations can provide important observations for further refining of the models. Examples of microstructure based models are models considering the local approach to fracture [4–6], which use microstructural parameters to predict the fracture toughness and to understand the fracture behaviour of materials.

This work utilises two modern experimental techniques, the focused ion beam (FIB) and the nanoindenter, to explore local mechanical properties and deformation mechanisms of iron and steel by means of the microcompression test [7–9]. The FIB is used as a micro milling tool to produce pillars on the surface of a sample. The pillars can be positioned with high precision in the local microstructure of the sample. The pillars are subsequently loaded with a nanoindenter equipped with a flat-punch indenter for uniaxial loading. The logged force and displacement data are analysed to study the local mechanical properties. The data are, together with images of the pillars, studied to understand the operating deformation mechanisms. These results advance the knowledge of the small scale deformation of iron and steel.

The initial studies [10, 11] were carried out on high strength low alloy steels. The aim was to develop the understanding of the fracture initiation process through knowledge of the local mechanical properties. The results proved that the pillar compression technique can be used to obtain local compressive properties. However, experimental difficulties, unknown underlying microstructure, scatter in the results and the desire for a fundamental understanding led to further work [12, 13] conducted on ferritic iron.

1.1 Objective

The primary objective was to develop a fundamental understanding and knowledge of the local mechanical properties and deformation mechanisms of iron and steel. The focus was to quantitatively analyse the local stress–strain response using the micro-compression test and to explore the local deformation mechanisms.
Two types of materials were investigated:

- Martensite and retained austenite containing constituents (M–A constituents or M-A phases) formed in high strength low alloy steel after weld thermal simulation.
- 99.99% pure iron that was annealed to produce sufficiently large grains for producing single crystal pillars.

The objectives for the two materials can be summarised as follows:

- Determine the flow curve of M–A constituents and gain insight into its deformation mechanisms.
- Determine the size and orientation dependent flow curves of ferritic iron and characterise the deformation mechanisms. This include to determine the slip system, from slip traces formed at the pillars' surface, and to describe the orientation dependency of the resolved shear stresses.

1.2 Publications and Conference Contributions

The present study continues and expands research conducted through the PhD candidate's Master studies at NTNU [14, 15]. Three research papers [11–13], which have been published or accepted for publication, was prepared by the candidate during the progress of the PhD study:

Paper I

B. R. S. Rogne, C. Thaulow, and A. Barnoush.

Micromechanical Testing of Fracture Initiation Sites in Welded High-Strength Low-Alloy Steel.

Metallurgical and Materials Transactions A, 45A(4):1996–2003, 2014.

Abstract: Micropillar compression-tests were performed on martensite (M) and retained austenite (A) containing constituents formed in high-strength low-alloy steel after simulated thermal weld heat treatment. Due to the complicated fine microstructure of the constituent, the resulted stress–strain curves were further analyzed by considering the post-mortem scanning electron micrographs and the morphology of the deformation of the pillars. It was possible to obtain relevant data for the uniaxial stress–strain behavior of the M–A constituent in the studied steel. Microvickers measurements, which were converted to macroscopic yield stress by empirical relations, were compared with the micropillar compression test results. Comparison showed that these empirical relations are overestimating the obtained mechanical properties of the M–A constituents.

Paper II

B. R. S. Rogne and C. Thaulow.

Strengthening Mechanisms of Iron Micro Pillars.

Manuscript submitted to: *Philosophical Magazine*.

Abstract: We examine the size effect and strengthening mechanisms of bcc iron pillars. The single crystal pillars were machined with focused ion beam and tested with a nanoindentation device with the compression axis along the $\langle 001 \rangle$ crystallographic direction. We compare our test results with both older literature on whiskers and micro/macro specimens, and recent results from atomistic modelling. We find that the obtained results can be explained on the basis of current theories based on small scale plasticity.

Paper III

B. R. S. Rogne and C. Thaulow.

Effect of Crystal Orientation on the Strengthening of Iron Micro Pillars.

Manuscript submitted to: *Materials Science and Engineering A*.

Abstract: Micro pillar compression testing has been performed on bcc iron single crystals to determine the mechanical properties and deformation mechanisms and their dependency on size and crystal orientation. Slip traces on the surface of post-compressed pillars were scrutinised to determine the operating slip system. The size dependency of the flow curves was investigated and the power law constants, K and n, and the orientation dependency of the resolved shear stresses were determined.

The slip trace analysis revealed that the slip follows the $\{110\}\langle 111\rangle$ family of slip systems. The size dependency of the flow stresses follows the power law relation where the power law exponent n are in general between 0.5–0.8 and depend on orientation and the strain. The power law coefficient K increases as a function of strain. The shape is similar for the different loading directions, but varies in magnitude. The shear stress resolved to the $(\bar{1}01)[111]$ slip system shows an orientation dependent relation. Size and strain has little effect on this relation.

In addition, the PhD candidate co-authored the following paper [10]:

- V. G. Haugen, B. R. S. Rogne, O. M Akselsen, C. Thaulow, and E. Østby.
  Local Mechanical Properties of Intercritically Reheated Coarse Grained Heat Affected Zone in Low Alloy Steel.
  Materials & Design, 59:135–140, 2014.
  Abstract: Steels applied in arctic climates are subjected to low temperature. Since they undergo ductile-brittle transition with falling temperature, their fracture toughness must be addressed, particularly after welding. To predict their behaviour requires knowledge on local properties. Thus, the present study concerns nanomechanical testing of typical microstructures present in the intercritically reheated coarse grained heat affected zone of a 490 MPa forging. Such microstructures were achieved by weld thermal simulation of samples with 11 mm × 11 mm cross section and 100 mm length, using peak temperature of 1350 °C in the first cycle and 780 °C in the second cycle. Both cycles used cooling time $\Delta t_{8/5}$ of 5 or 10 s. This caused formation of M-A phases along prior austenite grain boundaries and mixture of bainite/tempered martensite in the bulk. Nanomechanical testing was performed by compression of nanopillars prepared in grain boundary located M-A phases and in the bulk of the grains. The results achieved

showed significant that the grain boundary phase possesses much higher strength than the grain bulk. It is also shown that there is large scatter in the stress-strain data, depending on the actual local microstructure being tested.

The PhD candidate has also contributed in the following conference presentations[1] and articles [16, 17]:

- B. R. S. Rogne, V. Haugen, C. Thaulow, and A. Barnoush.
  Steels Revisited by Nanomechanical Testing.
  Nano- and Micromechanical Testing in Materials Research and Development IV.
  Olhão, Algarve, Portugal. 6-11/10/2013. (Poster presentation)

- V. Haugen, B.R.S. Rogne, O.M. Akselsen, C. Thaulow, and E. Østby.
  On Local Properties of Microstructures in Welding.
  Proceedings of the Twenty-second (2012) International Offshore and Polar Engineering Conference (ISOPE). Rhodes, Greece. 17-22/6/2012, pp. 16–22. (Oral presentation and paper)

- R. Brenden, B. R. S. Rogne, and C. Thaulow.
  Mechanical Properties of Biological Hard Tissues.
  Nanobrücken II: Nanomechanical Testing Workshop & Hysitron User Meeting.
  Saarbrücken, Germany. 22-23/3/2012. (Poster presentation)

- B. R. S. Rogne and C. Thaulow.
  Investigation of Nanomechanical Test Methods on Arctic Steels.
  Proceedings of the Twenty-first (2011) International Offshore and Polar Engineering Conference. Maui, Hawaii, USA. 19-24/6/2011. pp. 426–431. (Oral presentation and paper)

1.2.1 Individual Contribution

- The PhD candidate's contribution to *Paper I–III* [11–13] was designing and performing the experiments, analysing the data and preparing the manuscripts.

- C. Thaulow has contributed with conception and design of experiments, discussions, advice and critical revision of *Paper I–III* [11–13].

---

[1] The presenting author is underlined.

- A. Barnoush took an active part in *Paper I* [11] co-writing part of the manuscript, editing and helping through the reviewing process. His discussions and advice helped shape the paper into its final form.

1.3 Main Findings

The findings from *Paper I–III* [11–13] can be summarised as follows:

Flow curves from M–A constituents were obtained from FIB milled pillars with diameters of 1 and 3 µm. The yield stresses ranged between 0.8–1.2 GPa. The possible sources of the scatter were discussed and it was concluded that the surface roughness and the microstructural inhomogeneities play crucial roles. The largest pillars showed the highest strength which can be explained by a very fine and complicated microstructure of the M–A constituents. The most reliable tests showed that the yield stress is approximately 1.2 GPa, which is in accordance with tests from other references [18, 19] on martensite. Microhardness measurements were obtained from M–A constituents and converted into tensile properties, by using empirical relationships, and further validates the results.

Single crystalline iron micro pillars were compressed along five crystallographic directions, $[\bar{1}49]$, $[\bar{2}35]$, [001], [011] and $[\bar{1}11]$, to investigate deformation mechanisms and strength as a function of pillar size. The diameters of the pillars ranged from 120 nm to 4.3 µm.

The stress–strain curves obtained from the experiments show similar characteristic features as previously reported (*e.g.* [20–22]) for other bcc metals. Yield stresses obtained from the experiments ranged from 237 MPa to 4.5 GPa, where the highest stresses were obtained from the smallest pillars. The flow stress and pillar diameter relation follows a power law relation. The power law exponent is typically between 0.5–0.8 and depends on the pillar orientation and the strain where it was obtained from. The exponent falls between results from previous investigations of bcc metals [21, 22]. The power law coefficient (unit: $\mathrm{MPa}\,\mu\mathrm{m}^n$) advanced similar to a flow curve as a function of strain undergoing a strain hardening like behaviour. The magnitude of the power law coefficient depends on orientation, but is similar in shape.

To set the work in perspective, the yield stresses of the pillars were compared to experimental data from older literature on whiskers [3] and micro/macro specimens [1, 23–25], and recent results from atomistic modelling [26]. The results fall between these experimental data, Figure 1.1 (the figure is based on Figure 7 in *Paper II* [12]).

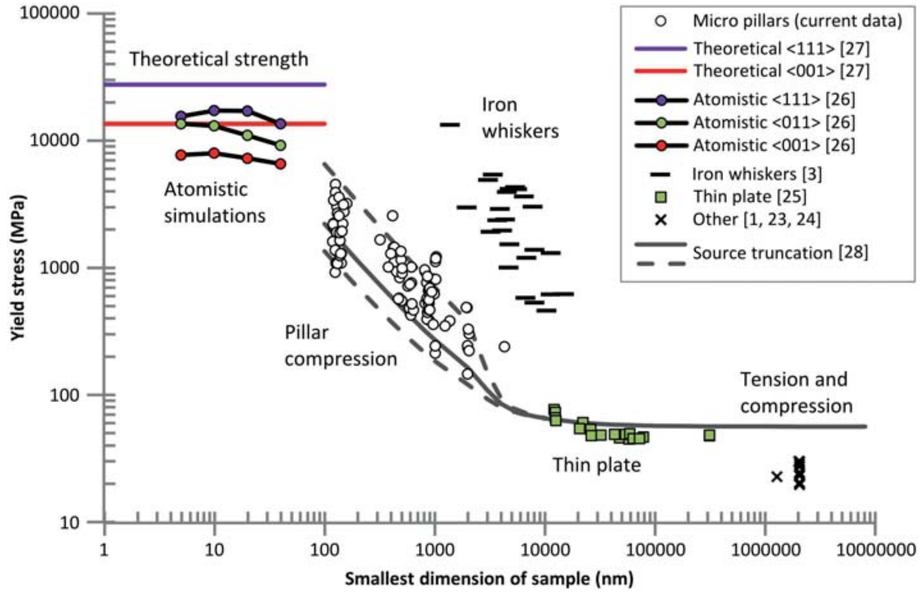

Figure 1.1: Yield stress of different sized single-crystal iron samples. Micro pillars (current data) consist of pillars compressed along the $[\bar{1}49]$, $[\bar{2}35]$, [001], [011] and $[\bar{1}11]$ crystallographic directions. Data for comparison were obtained from: theoretical strength [27], atomistic simulations [26], iron whiskers [3], thin plate [25] and other [1, 23, 24]. The size effect was predicted by the source truncation model [28]. The figure is based on Figure 7 presented in *Paper II* [12].

A procedure for evaluating the slip traces on the pillar surface was described and applied. The slip traces followed the $\{110\}\langle 111\rangle$ family of slip systems, except for orientation $[\bar{1}11]$ where the slip planes were not identified. The slip traces on pillars with orientations $[\bar{2}35]$, [001] and [011] followed the primary $(\bar{1}01)[111]$ slip system, *i.e.* the slip system of $\{110\}\langle 111\rangle$ type which encountered the highest shear stresses according to Schmid's law. Because of symmetry in the crystal, orientation [001] deformed on eight equivalent slip systems with two slip planes along each of the four slip directions. Correspondingly, orientation [011] deformed along four equivalent slip systems divided into two directions. Orientation $[\bar{1}49]$ followed mostly the primary $(\bar{1}01)[111]$

slip system, however, the deformation was in some pillars confined solely to the secondary $(101)[\bar{1}11]$ slip system or as a combination of both the primary and secondary slip systems.

The resolved shear stresses were calculated and evaluated in relation to orientation, pillar size and strain. The resolved shear stress was obtained by resolving the stresses to the $(\bar{1}01)[111]$ slip system by applying Schmid's law. The resolved shear stress increases with decreasing pillar diameter or increased strain and shows an orientation dependent relation. Pillar size and strain appear to have little effect on this relation. Pillars oriented in antitwinning orientations, *i.e.* where the shear stress is highest along the antitwinning direction of a $\{112\}$ plane, obtains a higher stress than when oriented in twinning orientations. When comparing the results with tensile experiments of mm-sized iron single crystals by Aono *et al.* [29], the twinning–antitwinning asymmetry are stronger for the compressed pillars.

1.4 Overview of the Thesis

This thesis consists of an introductory overview and three research papers [11–13]. The overview gives a theoretical basis to the research work and spans from Chapter 2 to Chapter 3. The papers are appended in the end in Chapter "Appended Papers".

The introductory overview gives a summary of selected topics that play an important role in the background of the published research results. Chapter 2 covers aspects related to the deformation of metals, with a focus on ferritic iron. This includes basic crystallographic aspects, dislocation theory and deformation of iron single crystals. Chapter 3 introduces the main experimental techniques, the focused ion beam and the nanoindenter. How the FIB interacts with the sample surface and how it can be used as a micro manufacturing tool for producing pillars is explained. Furthermore, the nanoindenter and how it is used as a compression device for pillars is presented, where the typical experimental outcomes are in focus.

The three papers are schematically summarized in Figure 1.2. The figure relates the investigated materials to the local microstructure of a polycrystalline sample containing hard and brittle particles. *Paper I* investigates the compressive properties of hard and brittle particles (M–A constituents) formed in a heat treated high strength low alloy steel. *Paper II* and *III* investigate ferritic iron single crystals and the effect of pillar size and orientation.

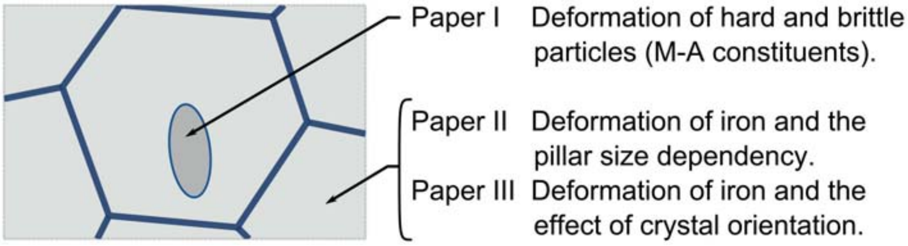

Figure 1.2: Illustration of the local microstructure of a polycrystalline sample containing hard and brittle particles. The local microstructure is related to the investigated materials in the three main papers [11–13].

Chapter 2

Deformation of Iron and Steel

The macroscale properties of crystalline materials are dictated by the underlying atomic structure. The movement of dislocations in the crystal structure produces the plastic deformation. The properties depend upon the available dislocations and how they move and interfere with obstacles in the microstructure. Pillar compression experiments are a useful tool to understand the mechanisms of plastic deformation. The technique probes a limited volume of material to obtain its compressive properties and can evaluate the strength of differently oriented crystals and the strengthening from grain boundaries.

This chapter gives an overview of how plastic deformation occurs in iron, with a focus on ferritic iron. The complexity and variations of steels are not covered. However, the basic concepts are applicable to most steels as well. Further reading can be found in textbooks within materials science [30, 31] and dislocation theory [32, 33].

2.1 Crystal Structures of Iron

At room temperature, pure iron has a *body centred cubic* (bcc) crystal structure as illustrated with the bcc unit cell in Figure 2.1(a). The bcc iron is named ferrite, or α-iron (α-Fe), and shares its crystal structure with several common metals, for instance manganese (Mn), molybdenum (Mo), niobium (Nb), tantalum (Ta), tungsten (W) and vanadium (V). At elevated temperatures the stable crystal structure of iron changes to *face centred cubic* (fcc), between 910–1400 °C, before it changes back to bcc beneath the melting temperature of 1538 °C. The fcc phase of iron is termed austenite, or γ-iron, and the bcc phase between 1400–1538 °C is known as δ-iron. The fcc structure is found in metals such as aluminium (Al), copper (Cu), gold (Au), lead (Pb), nickel (Ni), platinum (Pt) and silver (Ag).

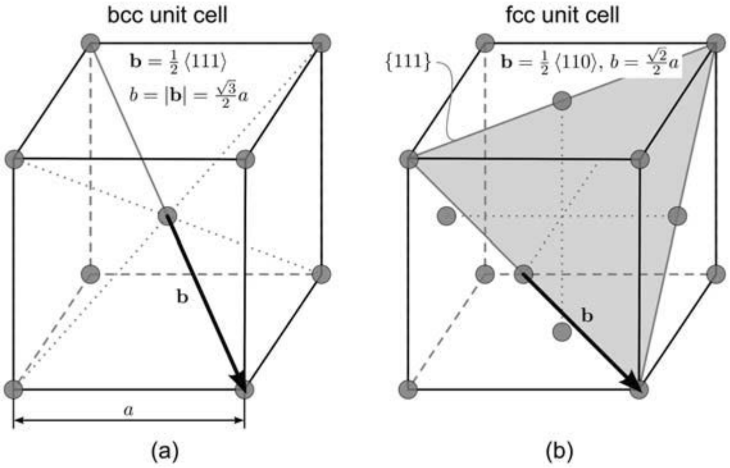

Figure 2.1: The (a) bcc and (b) fcc unit cell.

2.2 Crystal Defects

All real metals contain *imperfections* in the crystal lattice that disturb the local arrangement of the atoms. The imperfections can be point, line, surface and volume defects. The defects can modify the physical and mechanical properties of metals.

Point defects are small irregularities in the ordered crystal structure. In pure metal there exists two main types, vacancy and interstitial. The vacancy, or vacant atomic site, is an atom missing from its specific atomic site. The interstitial is an atom placed outside the lattice sites of the crystal. A vacancy and a self-interstitial atom of a pure metal are illustrated in Figure 2.2(a). Vacancies and interstitials are produced from plastic deformation and high energy particle radiation of the crystal and its thermodynamically stable concentration depends on the temperature. Impurity atoms can form point defects by taking up lattice sites in the original crystal, Figure 2.2(b). If the impurity atom replaces an atom site from the original lattice, it forms a substitutional impurity atom. An interstitial impurity atom takes the place between the ordered crystal lattice, similar to a self-interstitial atom.

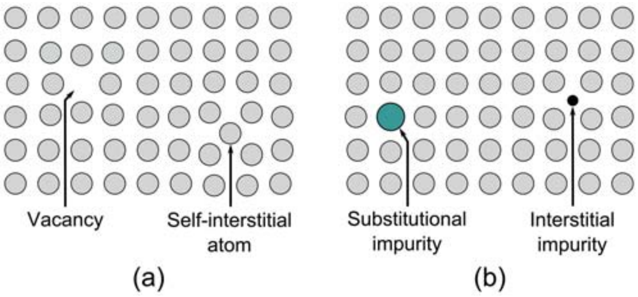

Figure 2.2: Point defects in a lattice. (a) Pure metal containing vacancy and self-interstitial atom. (b) Impurity atoms placed at substitutional and interstitial sites.

Dislocations are *line defects* and consist of displacement of the atom arrangement along a line. There are two basic types of dislocations, the edge and screw dislocation. Dislocations will be discussed in detail in the following section.

Surface defects, or a planar defects, are distortions that stretch out in an area. The grain boundary is the most common form of planar defects and are the plane between two crystals with different orientations. The atoms at the grain boundary are distorted. Other planar defects are stacking faults and twin boundaries.

Volume defects, or bulk defects, are larger defects that stretch out in the volume such as a void and a precipitate. The void is a small region with missing atoms and can be considered as clusters of vacancies. The precipitate is impurities clustered together in a small region and are often forming a different phase.

2.3 Dislocations

Deformation of a crystal takes place by the movement of dislocations and is called crystallographic slip. The dislocation responsible for the slip moves along the slip direction which always is parallel to its Burgers vector (**b**), which describes the direction and magnitude of the shortest lattice distortion. Slip steps at the surface are produced when dislocations move across the slip plane to the surface of the crystal.

The two basic types of dislocations are edge and screw dislocations. The *edge dislocation* moves in the slip plane parallel to its Burgers vector. For edge dislocations, the dislocation line is perpendicular to the Burgers vector and together they uniquely define the slip plane. Glide of an edge dislocation is limited to a specific slip plane.

Screw dislocation are dislocation where the Burgers vector is parallel to the dislocation line. Movement of a screw dislocation can take place along a slip plane. However, the dislocation line and Burgers vector do not define a unique slip plane, hence, the dislocation glide is not restricted to a specific plane.

Dislocations in real crystals are generally irregular in shape with a mixture of edge and screw character and are called *mixed dislocations.* A mixed dislocation is illustrated in Figure 2.3 and summarise the edge, screw and mixed dislocation. The dislocation line (red line in Figure 2.3) enters the crystal as a pure edge ($\perp$) and exits as a pure screw (↺). The part of the dislocation going through the crystal, between the pure edge and pure screw, is of mixed character.

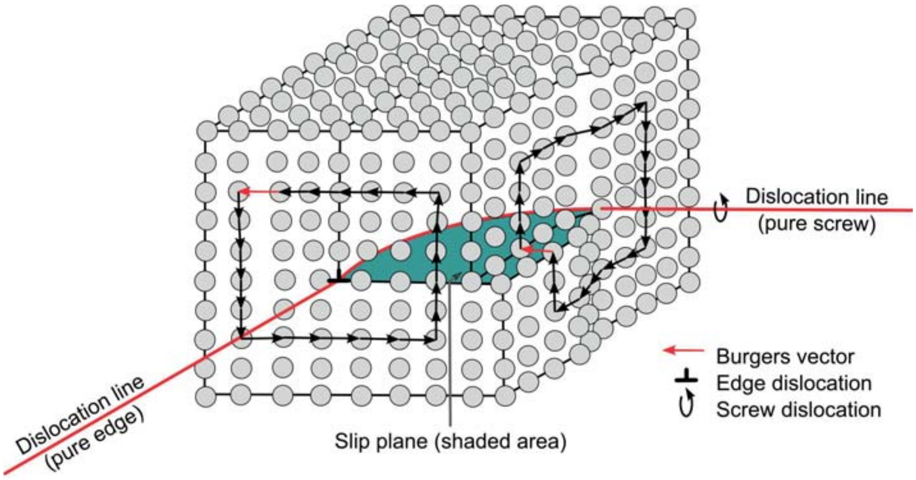

Figure 2.3: Mixed dislocation with segments of pure edge character, mixed character and pure screw character. The pure edge and pure screw segments are located at the surface of the crystal.

By applying *Burgers circuit* around the dislocation, it defines its Burgers vector. The Burgers circuit is a closed atom-to-atom path around the dislocation. If the same atom-to-atom path is made in a dislocation free crystal, the Burgers vector is required to close the path. The atom-to-atom paths in Figure 2.3 verifies that the pure edge got a Burgers vector perpendicular to the dislocation line, which together define the slip plane. In the same way, the pure screw obtains the same Burgers vector, but with the dislocation line parallel to the Burgers vector. The Burgers vector of the single mixed dislocation obtains the same Burgers vector. When the dislocation line lies at an arbitrary angle to the Burgers vector it is of mixed character.

2.4 Slip Directions and Planes

The deformation of cubic crystals is known to take palace along the close packed directions with steps corresponding to the shortest lattice vector, *i.e.*, the Burgers vector **b**.

The close packed direction in *fcc crystals* are along $\langle 110\rangle$ directions with $\mathbf{b} = \frac{1}{2}\langle 110\rangle$. The magnitude, or length, of Burgers vector ($b = |\mathbf{b}|$) in the fcc crystal is $b = \frac{\sqrt{3}}{2}a$. a is the lattice constant, or lattice parameter, of the cubic unit cell in Figure 2.1. The deformation follows slip planes which normally is the plane with the highest density of atoms, and corresponds to the $\{111\}$ planes in fcc crystals. One of the $\{111\}$ slip planes and one of its $\langle 110\rangle$ slip direction are illustrated in Figure 2.1(b). The combination of a slip plane and a slip direction lying on that plane is called a slip system. In total, there are four $\{111\}$ planes with three slip directions in each plane that combine into twelve $\{111\}\langle 110\rangle$ slip systems, Table 2.1.

In *bcc crystals* there are no true close packed directions, but the closest packed directions correspond to $\langle 111\rangle$ directions with $\mathbf{b} = \frac{1}{2}\langle 111\rangle$ and $b = \frac{\sqrt{3}}{2}a$. The bcc unit cell is illustrated in Figure 2.1(a), where Burgers vector is indicated as a vector.

There are three types of slip planes available along the $\langle 111\rangle$ directions. These are the $\{110\}$, $\{112\}$ and $\{123\}$ families of planes and are illustrated in Figure 2.4. The slip systems are summarised in Table 2.1.

Observation of slip directions and slip planes are often determined from *slip bands*, or slip traces, formed during deformation of samples with polished surfaces. The slip bands consist of a large number of slip steps. The apparent slip planes in bcc metals

Table 2.1: Families of slip systems and their slip planes and directions.

Crystal structure	Family of slip systems	Number of slip planes	Number of slip directions per plane	Number of slip systems
fcc	$\{111\}\langle 110\rangle$	4	3	12
bcc	$\{110\}\langle 111\rangle$	6	2	12
	$\{112\}\langle 111\rangle$	12	1	12
	$\{123\}\langle 111\rangle$	24	1	24

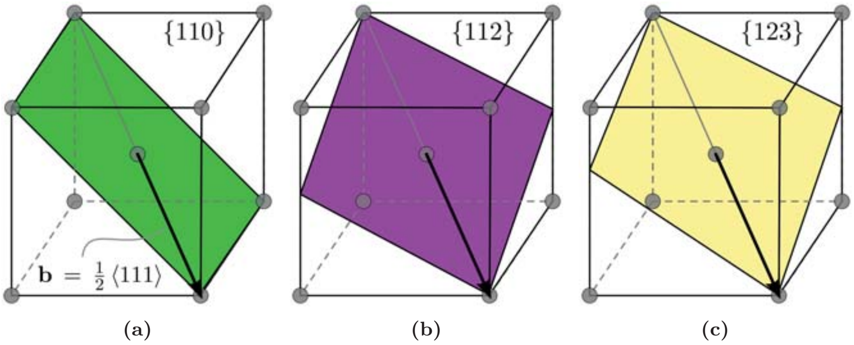

Figure 2.4: Slip planes in the bcc crystal. The (a) {110}, (b) {112} and (c) {123} families of planes.

depend on composition, crystal orientation, temperature and strain rate. The most frequently observed slip planes during deformation of iron at room temperature are of type {110} and {112} [24]. The observed slip bands are often observed to be wavy and ill-defined and follow the slip plane which encounters the highest shear stresses.

The huge amounts of possible slip planes along the same slip direction (48 possibilities along each slip direction) create the opportunity for screw dislocations to *cross slip.* During cross slip, the screw dislocation moves from one plane to another guided by the local stresses along its slip direction. Wavy slip bands indicate that cross slip happens easily. For this reason, the apparent slip plane is often found to follow the plane which encounters the highest shear stress along the slip direction, denoted as the maximum resolved shear stress plane (MRSSP). Since the MRSSP composes of collective slip from different slip systems it can in principle take any position along the slip direction. Figure 2.5 shows the intersection of {110} and {112} planes parallel to the [111] zone axis. The MRSSP is the plane that encounters the highest shear stress along the [111] direction. The location of the MRSSP is specified with the angle χ, which is defined as the angle between the $(\bar{1}01)$ plane and the MRSSP. χ is defined as positive when MRSSP lies between $(\bar{1}01)$ and $(\bar{1}10)$, and negative if it lies between $(\bar{1}01)$ and $(0\bar{1}1)$. [34–36]

An interesting feature of the {112} planes in bcc crystals is the lack of symmetry along the $\langle 111 \rangle$ slip directions. Because of the asymmetry, the dislocation behaviour

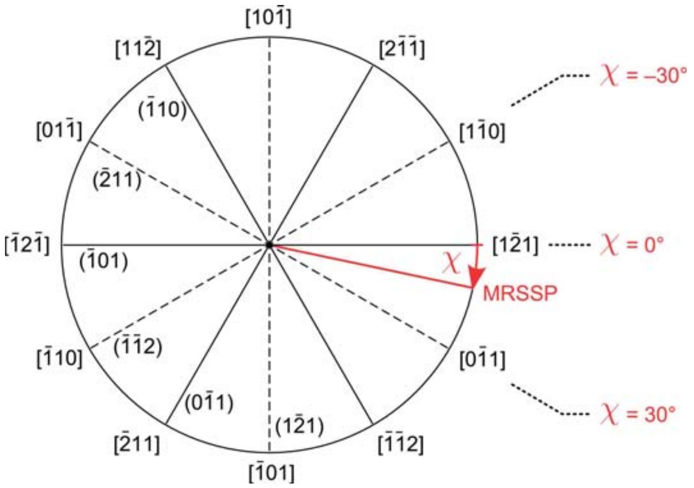

Figure 2.5: Orientation of the {110} and {112} planes, and the maximum resolved shear stress plane (MRSSP) of the [111] zone. The figure includes the plane normals. χ denotes the angle between the $(\bar{1}01)$ and the MRSSP. Figure modified from [33, Chapter 6].

depends on the direction of slip. Slip is easier when the dislocation moves in the twinning direction of {112} planes than in the antitwinning direction. The *twinning–antitwinning asymmetry* of the yield stress is observed even when the actual slip plane is not of type {112}. Some examples of the location of the MRSSP during compression and tension experiments are given in Table 2.2 and can be related to Figure 2.5. The shear stresses is highest on the {112} planes at $\chi = \pm 30^\circ$ and the slip direction is reversed if the loading mode changes from tension to compression. Dislocations moving in the twinning or antitwinning direction should not be confused with the deformation twinning mechanism which is observed at low temperatures and/or high strain rates.

Molecular dynamic simulations of dislocations give an insight into the nature of the dislocations. The *core structure* of the screw dislocation usually shows a non-planar character that takes the form as degenerate or non-degenerate. The degenerate, or polarised, core structure spreads the $\frac{1}{2}\langle 111 \rangle$ dislocation asymmetrically into three intercepting {110} planes as three fractional dislocations with a $\frac{1}{6}\langle 111 \rangle$ displacement each. The non-degenerate, or compact, core structure spreads symmetrically on the {110} planes with six fractional dislocations with a displacement of $\frac{1}{12}\langle 111 \rangle$ each. Non-screw dislocations form a planar dislocation core in form of either {110} or {112}. They

Table 2.2: Location of the maximum resolved shear stress plane (MRSSP) in relation to the twinning and antitwinning direction during uniaxial loading of bcc crystals. χ denotes the angle between the $(\bar{1}01)$ and the MRSSP.

χ (°)	**MRSSP**	**Slip direction in** **Tension**	**Compression**
30	$(\bar{2}11)$	Antitwinning	Twinning
0	$(\bar{1}01)$		
−30	$(\bar{1}\bar{1}2)$	Twinning	Antitwinning

move at much lower shear stresses than the screw dislocations and are not sensitive to non-shear stresses. [33]

2.5 Pole Figures

Pole figures are conventional ways of representing a set of crystallographic orientations. Strictly, the pole figures do not reveal the orientation of individual crystals, instead it visualises the orientation of particular crystallographic planes or directions. The pole figures are widely used in material science and give a relatively easy interpretation of crystallographic orientations, or textures. This section introduces two types of pole figures, the stereographic projection and the inverse pole figure.

The *pole figure* of a specific crystallographic plane can be obtained in the following way. The orientation of a particular plane is completely specified by one of its two plane normals, which point in opposite directions. If a unit sphere is drawn around the plane, with the plane normal intersecting the origin of the sphere, the plane normal intersect the unit sphere on the upper hemisphere in a point p, Figure 2.6(a). This point p is referred to as *the pole* of the plane and is uniquely representing the orientation of a single crystallographic plane. For cubic crystals the pole is identical to the crystallographic plane whit the same indices. The pole figure is obtained when the hemisphere is projected into two dimensions. The *stereographic projection* of the pole p in Figure 2.6 is obtained by projecting p to the plane of projection located at the upper pole. The projected point (p') is found by drawing a straight line from the lower pole (Q) through the point p and into the projection plane. To represent a collection of points, *e.g.* where each point represents a single grain or volume element of a polycrystalline sample, the

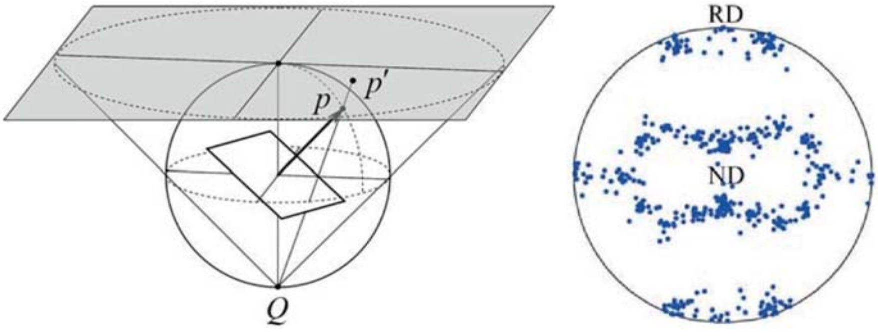

(a) (b)

Figure 2.6: (a) Projection of a crystallographic plane into the stereographic projection. The pole p of the plane is projected to the point p', which lies on the projection plane. (b) The {111} pole figure for a Cu texture. ND is the normal direction and RD is the rolling direction. Figures from [30, Chapter 3].

procedure above is repeated. The resulting pole figure gives a representation of the texture of the sample.

A typical pole figure of cubic crystals is the {111} pole figure, where the {111} planes are projected into the projection plane. The projection plane is conventionally the plane parallel to a sheet sample and is labelled with the normal direction (ND) to this plane and the rolling direction (RD), which normally is the transverse direction of highest symmetry. Figure 2.6(b) [30] shows an example of the {111} pole figure for a Cu texture.

The *inverse pole figure* (IPF) takes a different approach to visualise orientations. The IPF projects a vector pointing along a sample direction, *e.g.* along the growth direction of a crystal, into a plane determined by the local crystallographic orientation. Figure 2.7 shows the standard (001) stereographic projection of a cubic crystal where the plane of projection corresponds to the (001) plane, which acts as a local frame to the IPF. Due to high symmetry in the cubic crystal, all non-equivalent planes can be represented in each of the 24 stereographic triangles in Figure 2.7. The IPF is therefore often represented in the [001]–[011]–[$\bar{1}$11] *standard stereographic triangle* of the (001) stereographic projection, shaded area in Figure 2.7.

Pole figures or IPFs give a comprehensive representation of the texture of a sample

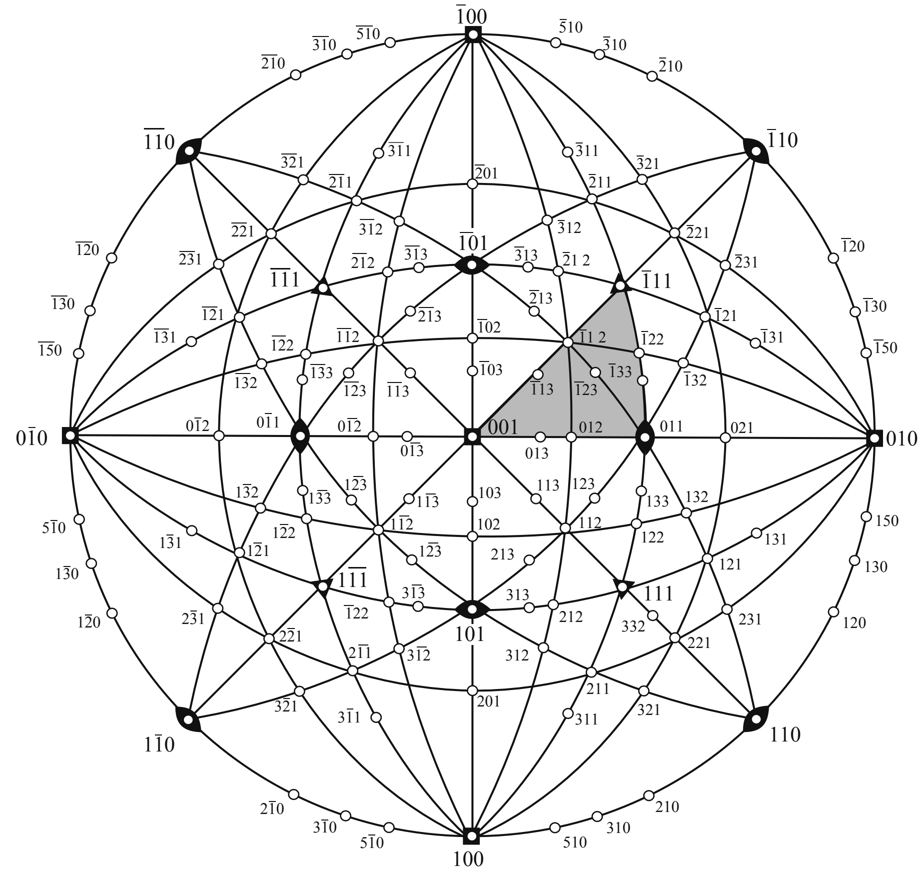

Figure 2.7: The standard (001) stereographic projection of a cubic crystal. The shaded area is the [001]–[011]–[$\bar{1}$11] standard stereographic triangle in the projection. Figure from [37, Chapter 4].

or a collection of sample orientations. The standard stereographic triangle is often used for colour coding of sample surfaces where the crystallographic orientations have been determined, for instance from electron backscatter diffraction (EBSD). The colour code is given with the IPF in Figure 2.8(a), which also visualises the orientation of five crystals. Example of an IPF-map from an EBSD scan of a polycrystalline Fe sample is seen in Figure 2.8(b). In the IPF-map, the crystal directions normal to the sample surface are coloured according to the standard stereographic triangle of the IPF in the upper left corner.

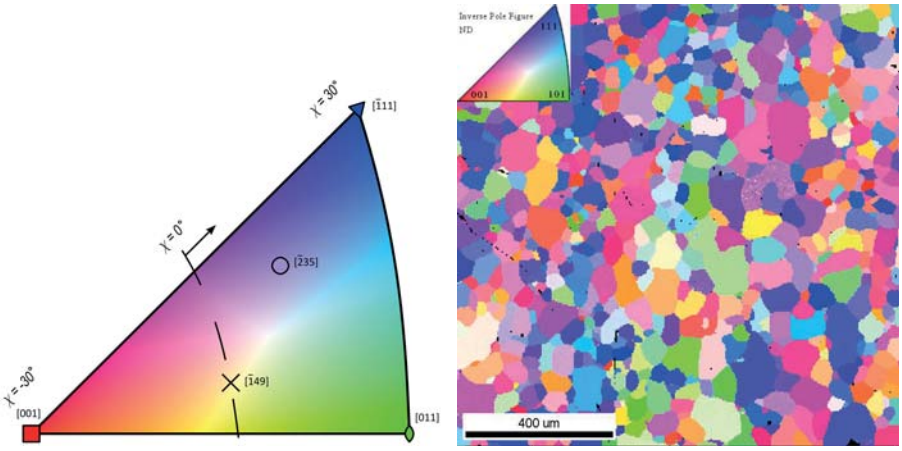

(a) **(b)**

Figure 2.8: (a) The [001]–[011]–$[\bar{1}11]$ triangle of the (001) stereographic projection of cubic crystals. The triangle includes orientation colour coding and visualises the orientation of five crystals. (b) The inverse pole figure (IPF) map obtained from electron backscatter diffraction mapping (EBSD) of a polycrystalline Fe sample.

2.6 Resolved Shear Stresses

The traditional way of analysing the resistance to plastic flow is by resolving the loading stress to a crystallographic defined slip plane along its slip direction. Figure 2.9 illustrates crystallographic slip along a slip system of a crystal loaded in tension. The component of the shear stress acting on the slip plane along the slip direction is obtained by using the *Schmid's law* in Equation (2.1a). The factor $S = \cos\varphi \cos\lambda$ is

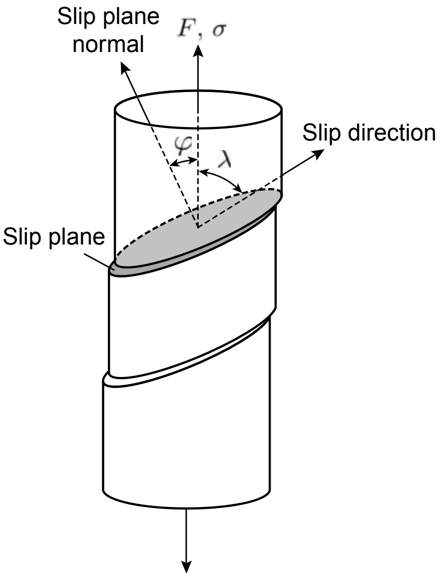

Figure 2.9: Crystallographic slip during tensile testing of a single crystal. φ is the angle between the loading direction and the slip plane normal and λ is the angle between the loading direction and the slip direction. Figure modified from [33, Chapter 3].

known as the Schmid factor. φ is the angle between the loading direction and the slip plane normal and λ is the angle between the loading direction and the slip direction. When the resolved shear stress (τ) reaches a critical value, where a dislocation on the slip plane starts to glide, it becomes equal to the critically resolved shear stress (τ_c). From the same geometrical relations the resolved shear strain (γ) on the slip plane along its slip direction can be calculated from the plastic strain (ε) in Equation (2.1b).

$$\tau = \sigma S \tag{2.1a}$$

$$\gamma = \frac{\varepsilon}{S} \tag{2.1b}$$

In a single crystal, there are several slip systems, even several families of slip systems, where slip can take place. If the dislocation glide on all of the slip systems are activated by the same τ_c we can use Equation (2.1a), or the Schmid factor S, to predict the activated slip system from a given crystallographic loading direction. If the loading direction changes, *e.g.* a different crystal is tested, the favoured slip system might change to a different slip system. As already presented, in the bcc crystal there are three families of slip systems, $\{110\}\langle 111\rangle$, $\{112\}\langle 111\rangle$ and $\{123\}\langle 111\rangle$, that are candidates for crystallographic slip.

If for example the $\{110\}\langle 111\rangle$ are assumed to be the only operating slip systems, and the crystallographic loading direction is related to the standard stereographic triangle (shaded area in Figure 2.7), according to Equation (2.1a) the slip system that encounters the highest S will be the $(\bar{1}01)[111]$. By considering both the $\{110\}\langle 111\rangle$ and $\{112\}\langle 111\rangle$, the slip systems that encounter the highest S will change depending on the crystallographic loading direction. The results are summarized in Figure 2.10(a) [38], where the crystallographic loading direction, represented by the standard stereographic triangle, is related to the slip system with the highest S. In Figure 2.10(b) [39] all the three families of slip systems, $\{110\}\langle 111\rangle$, $\{112\}\langle 111\rangle$ and $\{123\}\langle 111\rangle$, are considered. Note that the slip direction mainly corresponds to the [111] direction, but changes to $[\bar{1}11]$ direction near the 001 pole [39–41]. Another remark is that bcc crystal can violate

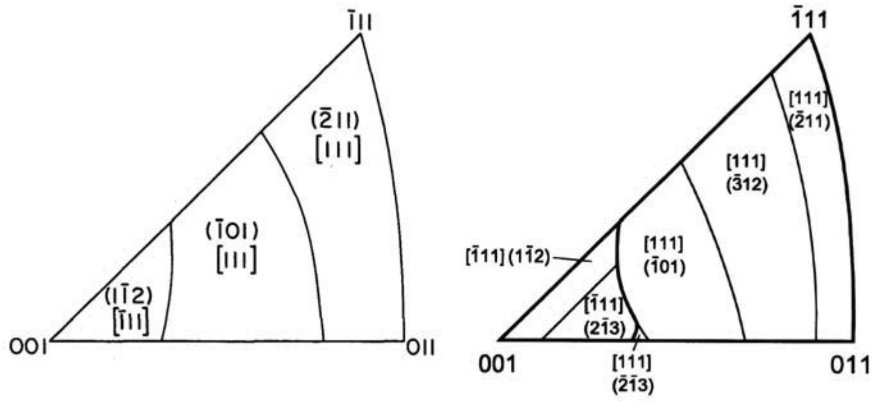

(a) (b)

Figure 2.10: Relation between the crystallographic loading direction and the slip system that encounters the highest Schmid factor in bcc metals. The loading direction is related to the standard stereographic triangle and the considered families of slip systems are (a) the $\{110\}\langle 111\rangle$ and $\{112\}\langle 111\rangle$ systems, and (b) $\{110\}\langle 111\rangle$, $\{112\}\langle 111\rangle$ and $\{123\}\langle 111\rangle$ systems. Figure (a) from [38] and (b) from [39].

the Schmids law [31, 33, 36], such as the twinning–antitwinning asymmetry presented in Section 2.4.

Screw dislocations in the bcc crystals have the ability to cross slip and the apparent slip plane follows the MRSSP (see Section 2.4 for further details and definitions). For this reason, the MRSSP has been used in several ways. It is for instance not uncommon to resolve the shear stress to the MRSSP (see *e.g.* [29, 35, 36, 39, 42]). This lead us to the χ–ψ diagram in Figure 2.11 [35]. The χ–ψ diagram compares the location of the MRSSP with the observed slip plane. ψ is the angle between $(\bar{1}01)$ plane and the experimentally determined slip plane [34, 35].

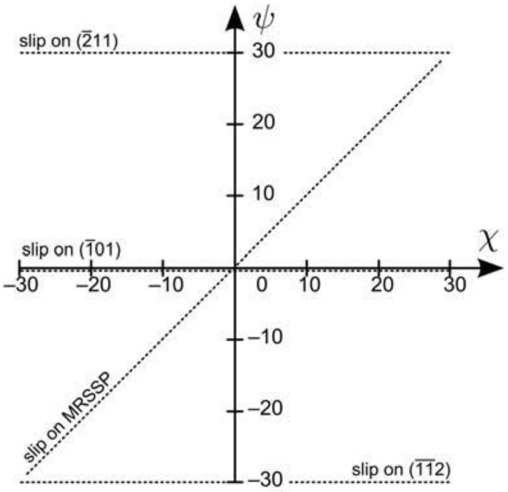

Figure 2.11: The χ–ψ diagram, where χ is the angle between the $(\bar{1}01)$ plane and the maximum resolved shear stress plane and ψ is the angle between $(\bar{1}01)$ plane and the experimentally determined slip plane. Based on figure from [35].

2.7 Strength of Iron Single Crystals

Experimental work on iron single crystals reveal that the resistance to plastic flow depends on factors such as temperature, strain rate, purity and loading direction of the crystal [24, 29, 33, 43]. The following pages give examples of flow curves and the yield stresses of iron single crystals deformed at different temperatures along various crystallographic orientations in tension, Figure 2.9. The presented data are from older literature with specimen sizes in the mm-range, which are further specified under each figure.

The *stress–strain curves*, or flow curves, from iron single crystals deformed in tension at room temperature obtain a shape that depends on the crystallographic orientation, see Figure 2.12. The flow curves show a upper and lower yield point. The work hardening, or strain hardening, depends on crystal orientation. Crystals with a loading axis at or near the boundary of the standard stereographic triangle obtain a higher strain hardening than the crystals located near the centre. Crystals located along the [001]–[011] line obtain flow curves that are nearly parabolic in shape. The other orientations show three stages of work hardening, schematically shown in Figure 2.13(c). *Stage I* work hardening, the so-called easy glide, starts after yielding where the deformation undergoes a moderate strain hardening at a constant strain hardening rate, with a linear appearance in the stress–strain curve. The strain hardening rate increases in *stage II* and decreases gradually into a parabolic shape in *stage III*. The extension of the three stages depend on crystal orientation. [43]

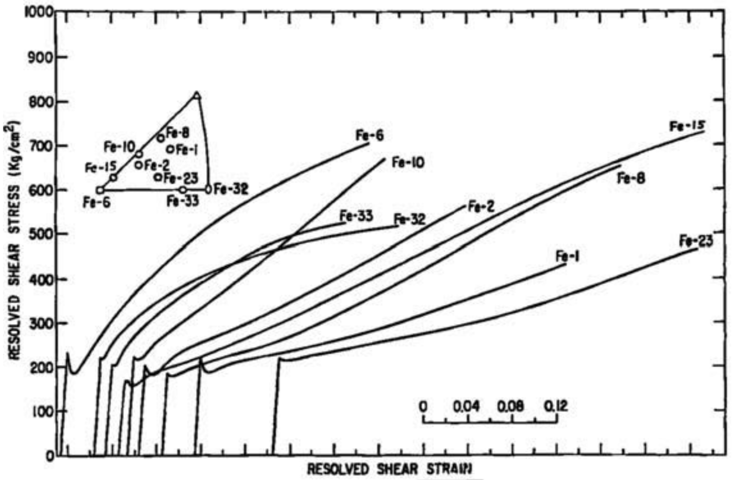

Figure 2.12: Orientation dependency of the stress–strain curves from iron single crystals. The tensile axis of the crystals are seen in the standard stereographic triangle and the curves were calculated from true stress–strain curves resolved by applying the Schmid factor. The samples got a rectangular cross section of 1.3×19.1 mm^2 and a length of 152.4 mm, with a gauge length of 25.4 mm. Figure from [43].

The resistance to plastic flow shows a strong temperature dependency and both the yield stress and the strain hardening increase with decreasing temperature, Figure 2.13(a) [24]. The three orientations, A, B and C, are related to its crystallographic tensile axis in Figure 2.13(b) [24].

The temperature dependency of the shear stress is shown in Figure 2.14. The shear stress (τ_y in Figures 2.14 and 2.15) was calculated from the tensile yield stress which

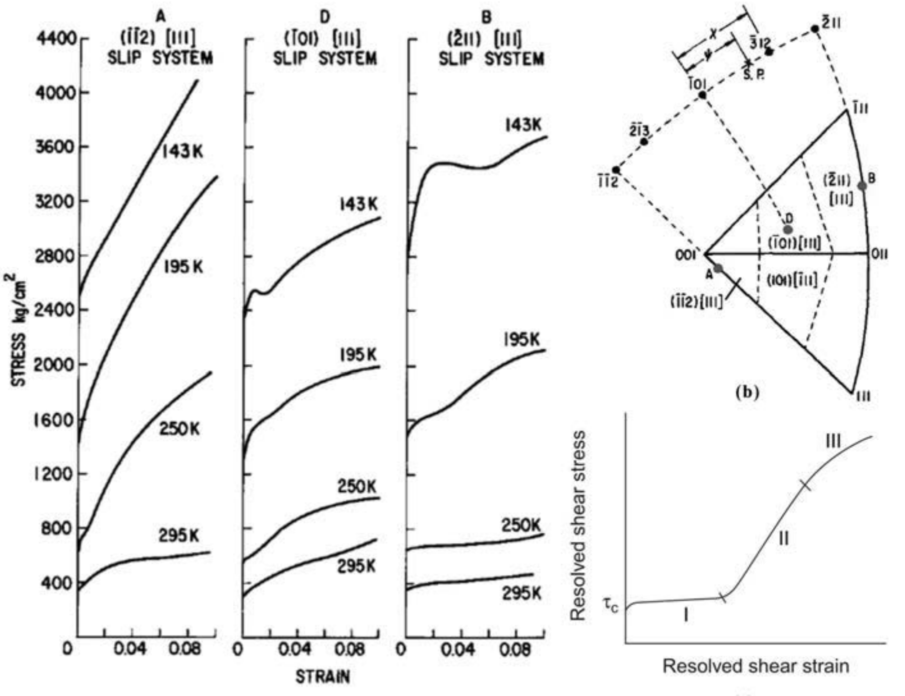

(a) (c)

Figure 2.13: Temperature and orientation dependency of the stress–strain curves from single crystals. (a) True stress–strain curves from tensile testing of three iron single crystals with orientations, A, B and C, at different temperatures. The samples got a nearly quadratic cross section of 2 × 2.5 mm^2 and the gauge length was 15 mm. The curves from the three orientations in (a) are related to its crystallographic tensile axis in the (b) standard stereographic projection. (c) Schematics of the resolved shear stress–strain curve of single crystals and its three stages of strain hardening. Figure (a) and (b) are modified from [24], and figure (c) from [33].

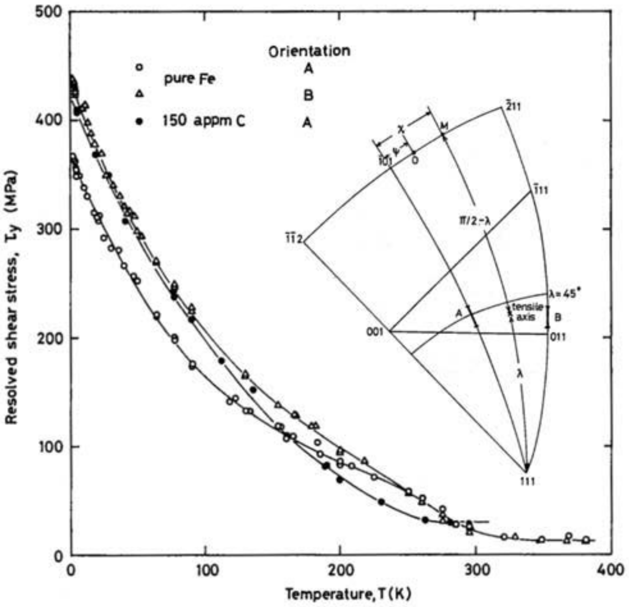

Figure 2.14: Temperature dependency of the shear stress. The shear stress was calculated from the tensile yield stress which was resolved to the maximum resolved shear stress plane (MRSSP) along the [111] direction. The samples got a circular cross section with 0.2 mm in diameter and a length of 20 mm, with a gauge length of 10 mm. Figure from [29].

was resolved to the MRSSP along the [111] direction. The yield stress, and the shear stress τ_y in Figure 2.14, increases rapidly as the temperature decreases. The yield stress is orientation independent around and above room temperature (273 K) but becomes increasingly orientation dependent as the temperature decreases. [29]

The orientation dependency of the shear stress τ_y is visualised as a function χ in Figure 2.15. The plateau stress above 67 °C (340 K), the athermal region, is measured to $\tau_\mathrm{y} = 15$ MPa and is independent on the orientation. At decreasing temperatures τ_y becomes gradually more orientation dependent. The orientation dependency becomes evident below −23 °C (250 K). Beneath −183 °C (90 K) the ratios

$$\frac{\tau_\mathrm{y}(\chi = -30^\circ)}{\tau_\mathrm{y}(\chi = 0^\circ)} = 1.12 \quad \text{(twinning direction) and}$$

$$\frac{\tau_\mathrm{y}(\chi = 30\,^\circ)}{\tau_\mathrm{y}(\chi = 0\,^\circ)} = 1.22 \ \text{ (antitwinning direction)}$$

become almost constant. [29]

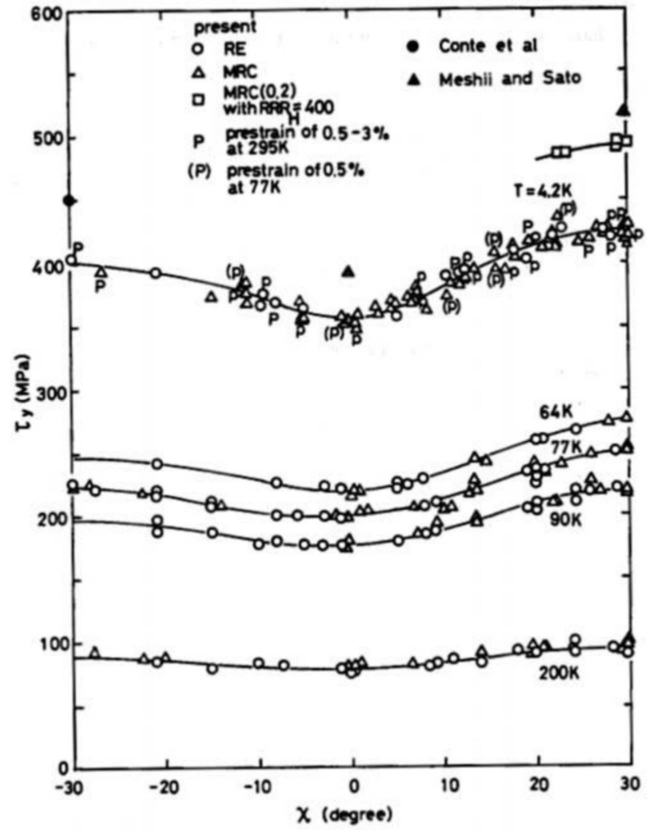

Figure 2.15: Orientation and temperature dependency of the shear stress. The shear stress was calculated from the tensile yield stress which was resolved to the maximum resolved shear stress plane (MRSSP) along the [111] direction. χ is the angle between MRSSP and the $(\bar{1}01)$ plane. The RE and MRC samples got a circular cross section with diameters ranging between 0.2–1 mm and a length of 20 mm, with a gauge length of 10 mm. Figure modified from [29].

Chapter 3

Experimental Techniques

Novel experimental techniques allow experiments to be conducted in new ways. Traditional material testing, like tensile experiments of mm-sized single crystals in Section 2.7, probes a large test volume. Large single crystals of iron are expensive and time consuming to produce. The results give a fundamental understanding of crystal plasticity, but are still very different from engineering materials. A method for exploring the material's mechanical properties at the length scale near the scale of the microstructural building blocks is therefore needed. An example of a new experimental technique used to explore material properties is the use of a focused ion beam (FIB) in combination with a nanoindenter. The FIB is used as a tool to manufacture micron and submicron specimens from specific regions of the sample surface. The specimen is subsequently loaded with the nanoindenter, equipped with a flat-punch indenter, to reveal its mechanical properties. Both engineering materials and idealised materials can be explored to solve scientific challenges and build up a fundamental understanding on how materials deform.

In this chapter, the basics behind the focused ion beam system and the nanoindenter system are described. Topics that are in focus are the ion beam and sample interaction, production of pillars, compression of pillars and deformation of pillars.

3.1 Micro Manufacturing

This section gives a brief introduction to the FIB system, how it is combined with a scanning electron microscope (SEM); how the ion beam interact with the sample surface and how pillars can be produced with the system. Main references for further reading in [44–46].

3.1.1 The Focused Ion Beam System

The *FIB system* accelerates and focuses a beam of ions towards the sample surface. During the ion–surface interaction the sample surface becomes slightly damaged by the colliding ions and particles from the sample surface are sputtered away. The sputtered particles can be collected to form an image of the surface or the technique can be used as a micro milling process by ramping up the ion current.

The traditional FIB system consist of a vacuum system and chamber, liquid metal ion source, ion column, sample stage, detectors, gas injection system and a computer that controls the instruments.

The *vacuum system* in a FIB system can be divided in two regions: source and ion column, and sample and detectors. The region of the source and ion column requires a high vacuum (typically 10^{-8} mbar) to avoid contamination and to prevent electrical discharge in the high voltage column. The sample and detector region requires a lower vacuum at about 10^{-6} mbar to keep a free ion path avoiding interaction between the gas molecules and the ion beam.

To produce an ion beam a *liquid metal ion source* (LIMS) is needed. The metal source is melted, ionised and pulled away from the source in a controlled manner. The metal source is attached to a non-reactive needle and surrounded with a coil heater. The coil heater is electrical feed and heats the metal source to a liquid state. The melted metal source is wetting the solid state needle. Beneath the needle tip, an extractor electrode is pulling the liquid metal to the needle tip forming a small point source. The surface tension and electrostatic tension shape the point source into a Taylor cone. The electrical field from the extractor electrode pulls off and ionises the metal by field evaporation.

The LIMS is usually made of gallium (Ga), because of its suitable properties. This include a high surface tension, low vapour pressure, low melting point (29.8 °C), reliable metal supply and long lifetime. The consumable Ga metal wet the needle to form a point source. The needle is usually made of tungsten (W) to avoid degradation of the needle geometry. When using Ga and W respectively as metal source and needle material the needle tip diameter is between 2–5 µm and the formed Ga Taylor cone obtains a diameter between 2–5 nm.

In the *ion column* the ion beam extracted from the LIMS is accelerated and focused down towards a sample attached to the sample stage. Besides the LIMS it is mainly composed of two lenses and an aperture. The first lens is the condenser lens directing the ion beam downward the ion column. When the ions meet the aperture, only the beam centre part will pass. After the beam reduction, from the adjustable aperture diameter, the second lens is focusing the beam toward a point on the sample surface. To obtain a thin beam at the sample surface, a correct beam voltage, aperture diameter and working distance is important. The thinnest beam is obtained with high voltage, small aperture diameter and short working distance.

The *sample stage* can usually move in five axes: x, y, z, rotational and tilt axis. The stage is often as large as 300 mm and has to be very stable to perform accurate positioning. Thermal stability is a key parameter to avoid both inaccurate positioning and specimen drift.

Image detectors in FIB are typical a multi-channel plate or an electron multiplier. A multi-channel plate is mounted directly above the sample and collects the secondary electrons (SE). There are two types of electron multipliers. One that collect secondary electrons and another collecting positive charged secondary ions (SI). The electron multiplier is placed in an angle of 45° to the ion beam.

Often the FIB system includes a *gas delivery system* that allows site specific deposition or enhanced etching. The gas is delivered in controlled amount into the camber. Use of gas injection needles allow the gas to be applied close to the point of interest usually about 100 µm over the surface. A deposition material is forming by letting a gas adsorb on the sample surface near the needle outlet. When the ion beam strikes, the gas will break down and form a thin deposit layer at the surface. By repeating this deposition process, the material builds up. The deposition process is a balance between milling and deposition. Too high ion beam current will mill away the deposited layer and into the sample. The deposited material can be a metal (W, Pt and C are common) or an insulator (different glass types). Chemically enhanced sputtering or etching can be done by applying selected gases to specific specimen material.

The SEM–FIB System

The FIB system is often combined with a SEM so that it is possible to image the sample surface simultaneously as the surface is being manipulated by the FIB, Figure 3.1(a). The combined *FIB–SEM system* extends the possibilities to produce complex shapes and perform advanced characterisations. The SEM can be used to deposit very low energy deposition that do not damage the underlying surface. Three-dimensional (3D) information is easy to obtain by switch between SEM imaging and milling off thin material slices. The stepwise images are then representing 3D pictures of a small volume. Instead of electron imaging, one can perform element mapping in form of x-ray energy dispersive spectrometry (XEDS) and crystallographic analysis using electron backscatter diffraction (EBSD) detection.

The FIB–SEM system used in this study was a Helios NanoLab™ DualBeam™ produced by FEI, Figure 3.1(b). The chamber holds a pressure lower than 2.6×10^{-6} mbar. Mounted inside the chamber ceiling is a SEM column, FIB column, Everhart–Thornley detector (ETD), three gas injection needles and a lift out finger. The lift out finger is mainly used to lift out transmission electron microscopy (TEM) samples prepared by the FIB. The SEM column is supplied with a through–the-lens detector (TLD). The ETD is of the type scintillator–photomultiplier, while TLD is a scintillator. The stage is 150 mm in diameter and can move in five axes with a piezo-driven stage.

3.1.2 Ion–Solid Interaction

To get a brief understanding of how the FIB interact with the sample surface an introduction to the *ion–solid interaction* is needed. When a high energy Ga^+ ion hits the sample surface it will interfere with the surface material trough elastic and inelastic interactions as illustrated in Figure 3.2 [46].

The *inelastic energy transfer* happens when the ion energy is transferred to electrons in the sample. This results in ionisation followed by emission of SE and electromagnetic radiation from the sample. In the *elastic interaction* the Ga^+ ion collides into the sample atoms followed by series of collisions in form of a collision cascade. If the kinetic energy transfer, from the Ga^+ ion into a sample atom, exceeds a critical value, the displacement energy, the atom will be displaced out of position. The displaced atom will further interact with other atoms and might result in several displaced atoms.

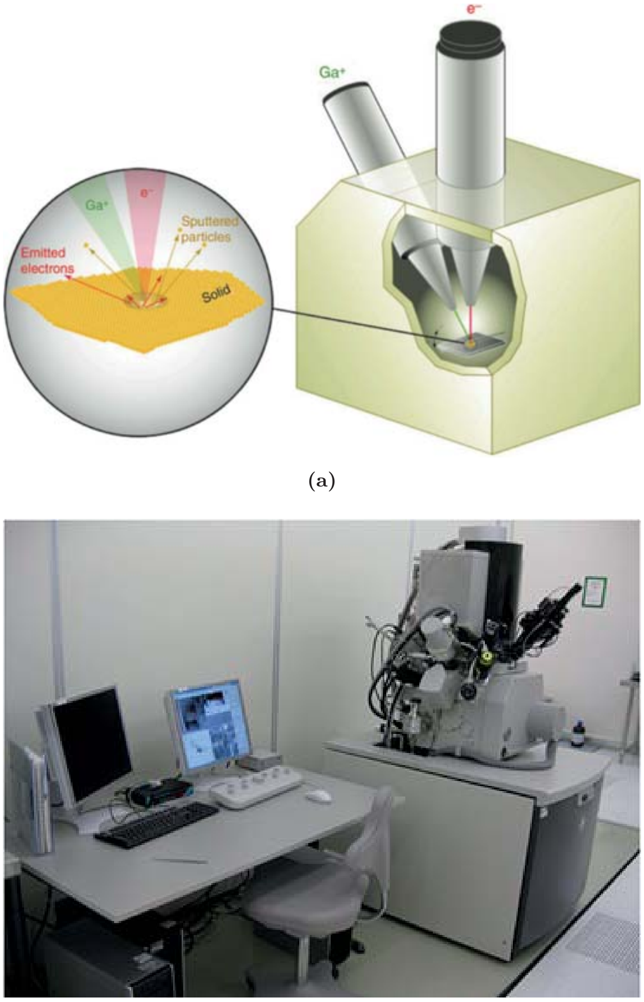

(a)

(b)

Figure 3.1: The combined FIB–SEM system. (a) Schematic illustration of the FIB–SEM system with expanded view of the ion beam and electron beam interacting with the surface. (b) The Helios NanoLab$^{\text{TM}}$ DualBeam$^{\text{TM}}$ system from FEI that was used in this study. Figure (a) from [46].

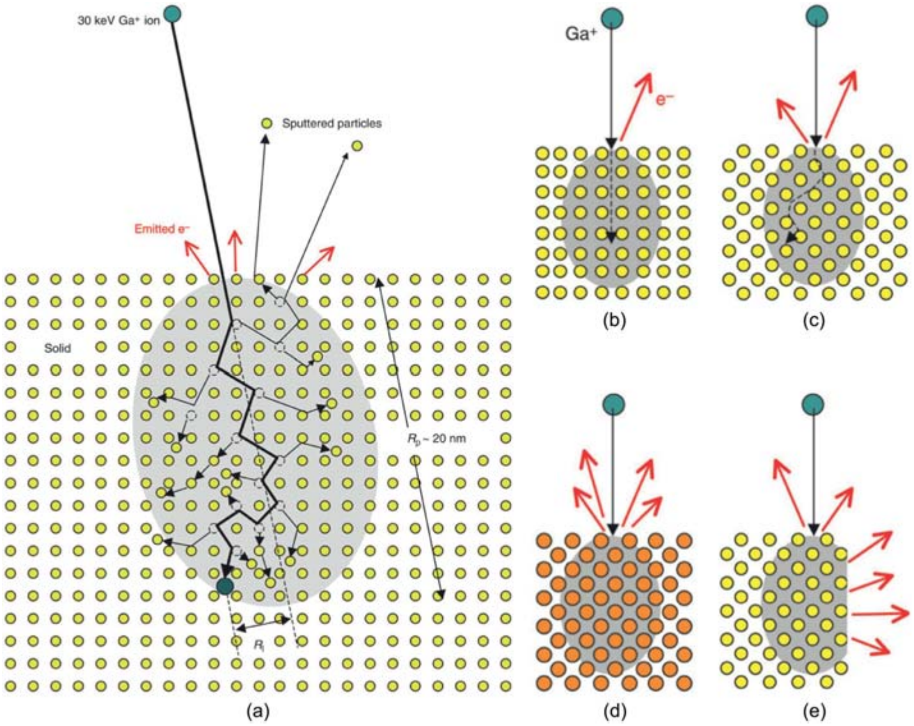

Figure 3.2: The ion–solid interaction. (a) The collision cascade for a 30 keV Ga$^+$ ion. When the ion enters the sample surface secondary electrons and sputtered particles are ejected from the surface. The Ga$^+$ ion is left implanted at a statistical projected range (R_p) and lateral range (R_l). The ion–solid interaction are effected by (b)–(c) variation in crystallographic orientation, (d) higher nucleus mass and (e) geometrically differences at the sample surface. Figures from [46].

Consequently, the collision cascade in a crystalline material can form an amorphous region. A surface atom displaced out of position might emit from the surface as sputtered particles. The sputtered particles can be charged or neural secondary particles. Eventually the Ga^+ atom stops, implanted into the sample surface.

Imaging

The ejected SE and positive charged SI can be collected to form an image. Standard imaging mode is to collect the ion induced SE to form a raster image. However, the ion induced SI image is frequently used and has some benefits. The two imaging techniques show mostly complementary information, but the ion induced SI picture is less effected by charging up effects. Insulating materials at the surface will be implanted with positive charged Ga^+ ions and the positive charged regions attract the emitted negative charged SE. Hence, no electrons will be collected for these regions and they appear as dark regions in SE image. This type of artefact is not seen in the ion induced SI picture since the positive charged particles are not retained back to the surface.

Picture contrast is obtained when the sputtering of SE or SI changes direction or amount. This is due to change in the crystal orientation, composition or topography of the sample. The parameters that effect the picture contrast is illustrated in Figure 3.2(b) to (e). Figure 3.2(b) and (c) illustrate differences in crystallographic orientation for a crystalline material, where in (b) the Ga^+ ion easily moves deep into the sample by channelling and in (c) the Ga^+ ion early collides into sample atoms. An increased nucleus mass, in (d), causes atomic number contrast and interaction near an edge, in (e), causes topographic contrast.

The SE and SI are produced for every frame in a raster image and collected by a detector. The FIB–SEM system allows the SEM to capture images while the FIB column is used for other applications. The ion induced SE image in Figure 3.3 [46] shows channelling and topographic contrast of a Cu sample with FIB produced shapes in the surface. The ion channelling effect makes it possible to produce images with clear contrast of the individual grain present. Standard beam current for FIB imaging are between 1–50 pA, where the high resolution images are obtained from the lowest beam currents.

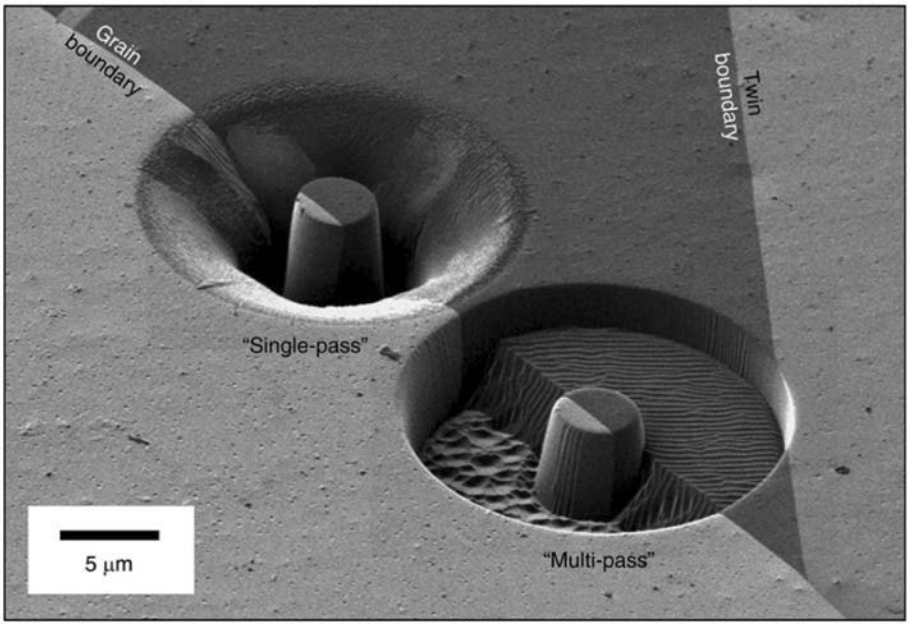

Figure 3.3: Ion induced secondary electron image of grain boundary in Cu with shapes produced by 30 keV Ga$^+$ beam. Figure from [46].

Milling

During imaging, particles are sputtered away from the surface in a low current milling process. By increasing the ion current, and hence the sputtering rate, the process becomes a micro milling process. The FIB milling allows material to be removed from the sample surface to form desired shapes. Usually the milling is done using predefined patterns or by making own scripts. The sputtering rate of the milling process depends mainly on the same parameters as for FIB imaging, where bright regions in the image indicates a strong signal from emitted electrons or sputtered particles.

New issues appear when material is removed fast from the surface. The sputtered particles might not move away from the sputtering site and rather settle down on a nearby surface as a redeposited layer. This *redeposition* becomes of great concern when the milled geometry contains a high aspect ratio. For instance, when trying to mill a deep ⊔-shaped trench it turns out as a ⋁-shaped trench. This happens because of the competition between the material removal and the material redeposition. Redeposition rate is highest for materials with a high material removal rate. To avoid, or minimise, redeposition the sputtering rate can be reduced, the milled geometry can be changed to a smaller aspect ratio or by introducing a gas that restrain the redeposition process. The sputtering rate is easiest reduced by regulating the incidence angle of the ion beam or reducing the ion beam current. The change in milling settings are illustrated in Figure 3.3 where the two regions were produced with the same ion dose but with different scan settings.

When milling in grains with variations in microstructure and grain orientation it is hard to obtain an even sputtering rate. The lowest sputtering rate is observed when the ion can move freely between the sample atoms by ion channelling, illustrated in Figure 3.2(b). The local differences in sputtering rate is seen in Figure 3.3 during milling at a grain boundary in a Cu sample. FIB milling is in general obtained with a relatively high currents, between 28 pA and 21 nA.

3.1.3 Pillar Production

Pillars produced by FIB milling have been widely used for the last decade as compression specimens at the micron and submicron scale. The specimens are typically ranging from several tens of micrometres to some few hundred nanometres. Large specimens are time consuming to produce and small specimens are limited by the FIB milling resolution. For crystalline or poly phase materials the specimens can be located in a single crystal, poly crystal or poly phase sample allowing to extract deformation behaviour of a specific crystallographic orientation or determine grain boundary effects.

The most used pillar type is the circular cross section geometry often referred to as pillar or column. Examples of literature with circular pillar geometries can be found in [8, 47–49]. Rectangular and quadratic cross section geometries has also been made [8, 50–53].

There exist two *milling methods* to produce cylindrical shaped pillars, lathe milling method [7, 8] and the top-down method [9]. In the lathe milling method, the FIB is oblique to the surface, Figure 3.4(a) [48], while in the top-down method the beam is perpendicular to the surface, Figure 3.4(b) [49]. Pillars milled with the top-down method are easy and fast to produce, but result in a varying cross section with a tapering, as seen in Figure 3.4(b). For a pillar with a height to diameter ratio between

2–3 the taper angle (α) is usually ranging between 2–5° [48]. Control of the pillar height is another challenge especially when milling in materials with polycrystalline or poly phases where the milling rate is varying within the pillar. Loading of tapered pillars leads to a non-uniform applied stress field within the sample that results in an inhomogeneous deformation. Consequently, the flow stress determination becomes inaccurate and the strain hardening becomes artificially high [48].

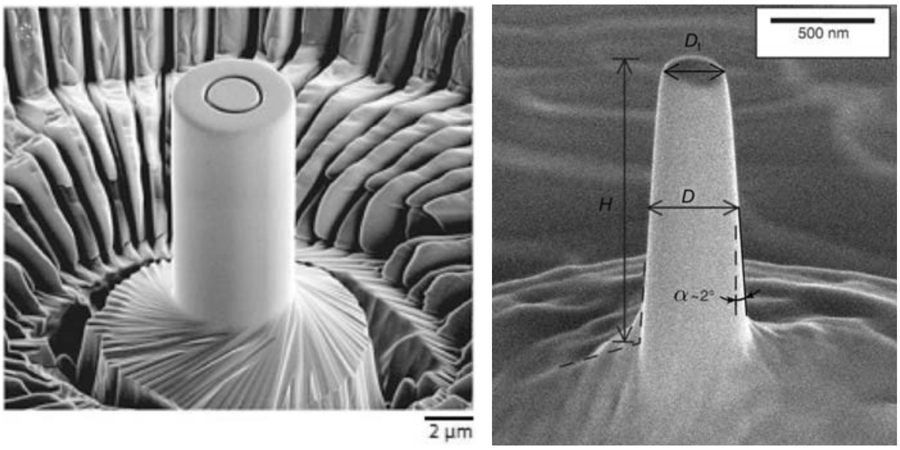

(a) Lathe milling

(b) Top–down milling

Figure 3.4: Pillar milled by using (a) using lathe milling method and (b) FIB beam perpendicular to the surface. Picture (a) from [48] and (b) modified from [49].

A lot of the problems concerning tapered pillars are reduced by fabricating cylindrical pillars with the lathe milling method, see Figure 3.4(b). The method secure a uniform cross section and a controlled pillar height. This way to produce pillars is more time consuming and limits the pillar dimensions to larger than about two micrometre in diameter. Another advantage is the ability to mill in polycrystalline or poly phase materials with difference in milling properties [8, 48].

3.2 Nanomechanical Testing

In the current work a *nanoindenter* was used to deform the pillars. In the following section, the nanoindenter is introduced as a high resolution tool for applying load and measuring displacement. A comprehensive introduction to nanoindentation testing can be found in [54].

3.2.1 Nanoindenter

The objective of a nanoindenter is to transfer a controlled load to an accurately shaped indenter that is in contact with the specimen surface. The load can be applied from an expanding piezoelectric element, movement of a coil in a magnetic field or electrostatically. The instrument is typically load-controlled and the range of applicable loads vary typically from under 1 μN and up to several mN. During the indentation process, the indenter is pushed into the sample surface by the applied load. During this process, the load and displacement of the indenter are logged and analysed to determine material properties of interest. The typical properties to obtain from a nanoindentation test are hardness and reduced elastic modulus. However, it can provide information on cracking, creep, strain hardening, phase transformation, fracture toughness and energy absorption.

Indenters, or nanoindenter tips, exists in standardised geometries, such as Berkovich, Knoop and cube-corner indenters, or can be tailor made for its purpose. They are usually fixed to a shaft and can be changed if necessary. Figure 3.5 shows example of a Berkovich indenter and a flat-punch, or flat-top, indenter.

The device used in this work was a TI 750 Ubi™ nanoindentation system from Hysitron equipped with a Performech® control unit, Figure 3.6. Central parts of the system are the optical camera, TriboScanner, transducer and sample stage, and are seen in Figure 3.6(b). The optical camera sends a top-down view of the sample surface to the software, which is used to navigate on the sample. The sample stage can move in three axes and are used to position the sample. The system can switch between the optical position, with the optical camera's focal plane at the surface, and contact mode, where the indenter approaches and obtains contact with the sample. The TriboScanner is equipped with a piezo scanner that moves in three axes and are used for the fine positioning of the indenter and for producing scanning probe images (SPI) of

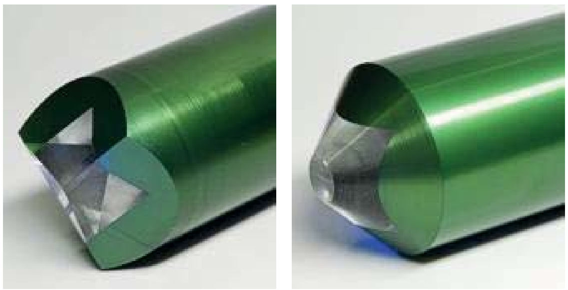

(a) (b)

Figure 3.5: Example of (a) Berkovich and (b) flat-punch indenter geometries. Figures from [55].

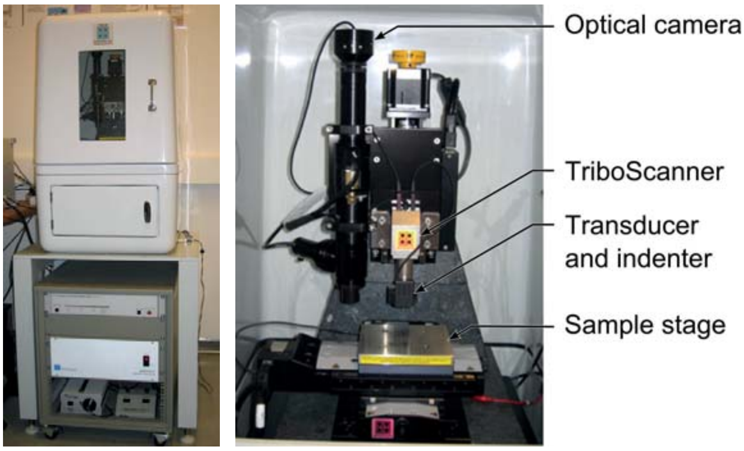

(a) (b)

Figure 3.6: (a) The Hysitron TI 750 Ubi$^{\text{TM}}$ nanoindentation system and (b) central parts behind the enclosure of the system.

the surface. The three-plate capacitive force/displacement transducer is patented by Hysitron and applies the force electrostatically, Figure 3.7. The indenter is mounted to the centre plate that is attached with springs and can freely move in the normal direction. The top and bottom plates are the driver plates where a modulating signal is applied. The modulating electrical potential applied to the centre plate produces an electrostatic actuated force that moves the centre plate and the nanoindenter tip. The force imposed to the indenter becomes the electrostatic actuated force plus the force produced by the extended springs. The displacement is calculated from measured current signals.

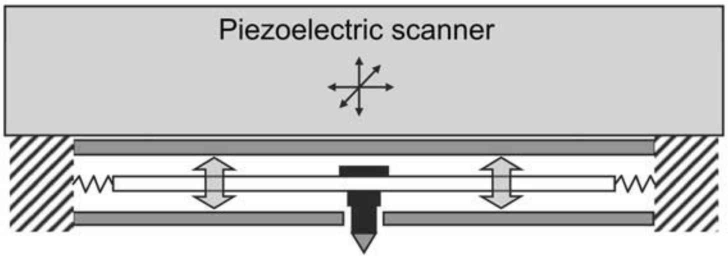

Figure 3.7: Schematics over the patented three-plate capacitive force/displacement transducer by Hysitron. Figure from [54].

In the current experiments the pillars were loaded with a flat-ended diamond indenter, as illustrated in Figure 3.5(b), from Synton-MDP in the open-loop load control mode. The high resolution and low drift during measurements make the instrument well suited for loading of FIB prepared pillars.

3.2.2 Pillar Compression

During a regular nanoindentation test, where an indenter is deformed into a flat surface, the obtained data are analysed by contact theory to calculate material properties (see *e.g.* [54]). The theory considers the interaction between the indenter and the sample surface. However, when the sample surface contain a geometrical feature, like a FIB milled pillar, different equations must be considered. For instance, the measured displacement is likely to be a combination of responses inside the pillar as well as in the material beneath the pillar and into the indenter.

Figure 3.8(a) illustrates the initial contact between the indenter and the pillar. The pillar is still attached to the material where it was machined. At this point, the contact load is close to zero. In a perfect experiment, full contact is obtained between the end-surface of the flat-punch indenter and the top-surface of the pillar. When the first load F is applied by the nanoindenter the measured deformation (Δ_{Measured}), which already is corrected for the machine compliance, will be combined into the pillar, the material under the pillar and into the end-surface of the indenter, Figure 3.8(b). Δ_{Measured} is hence expressed as the sum

$$\Delta_{\text{Measured}} = \Delta_{\text{Pillar}} + \Delta_{\text{Base}} + \Delta_{\text{Indenter}} \tag{3.1}$$

, where the subscripts refer to the pillar, material under the pillar base and into the indenter, respectively. If it is assumed that the geometrical changes during loading can be neglected, and that the material beneath the base of the pillar and into the indenter behave like isotropic linear elastic materials, the deformations can be estimated in the following way:

Sneddon [56] solved the force–displacement equation for a rigid flat-ended cylindrical punch that is loaded into an isotropic linear elastic material. The resulting displacement is described by the equation

$$\Delta = F\frac{(1-\nu^2)}{d\,E} \tag{3.2}$$

, where d is the indenter diameter, and ν and E are the Poisson's ratio and the Young's modulus of the loaded material, respectively. The displacement beneath the indenter

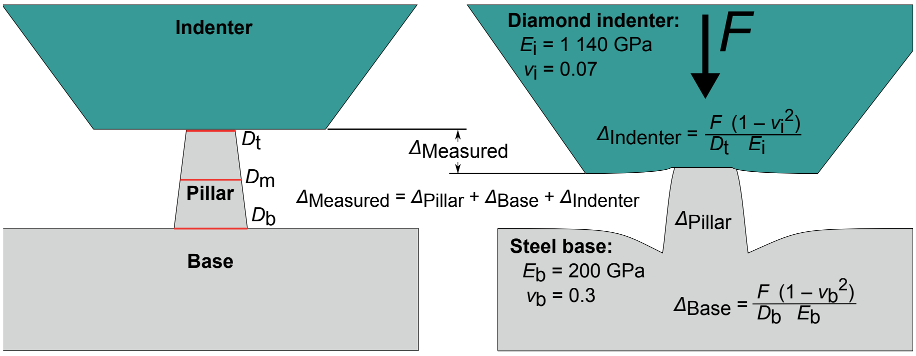

(a) (b)

Figure 3.8: Schematics of the elastic deformation during loading of a pillar. Indenter, pillar and sample (a) before and (b) during loading.

surface can then be estimated from Equation (3.2). The base of the pillar, with the diameter $d = D_\mathrm{b}$, corresponds to the rigid indenter and the loaded material, the material under the pillar base, got the properties $\nu = \nu_\mathrm{b}$ and $E = E_\mathrm{b}$. In the same manner, the deformation from the top-surface of the pillar, with the diameter $d = D_\mathrm{t}$, produces a deformation into the indenter, with the properties $\nu = \nu_\mathrm{i}$ and $E = E_\mathrm{i}$. For a diamond indenter and a steel sample, the elastic displacement under the pillar is about one order of magnitude smaller than into the indenter. By combining Equation (3.2), with the constants as described above, with Equation (3.1) the displacement inside the pillar becomes equal to:

$$\Delta_\mathrm{Pillar} = \Delta_\mathrm{Measured} - F\left(\frac{1-\nu_\mathrm{b}^2}{D_\mathrm{b}\,E_\mathrm{b}} + \frac{1-\nu_\mathrm{i}^2}{D_\mathrm{t}\,E_\mathrm{i}}\right) \tag{3.3}$$

The correction above, with or without accounting for the displacement into the indenter, has been applied by several authors previously, *e.g.* [9, 49, 57, 58]. The base might not always behave like an isotropic linear elastic material, however, in many circumstances the stresses will be distributed to a larger region early under the pillar base so that a minimum of plasticity takes place. The same applies for the indenter that got a much higher strength than the rest of the system. The exact displacements of and around the pillar are challenging to estimate, but applying such corrections produce a more accurate measurement of the displacement inside the pillar. When considering a stress–strain curve for general comparison the effort in registering all the pillar measurements and applying corrections to the displacements might not be worth it, however it is essential when estimating parameters such as the elastic modulus.

The stresses and strains inside the pillar can be calculate from the logged force and displacement data in a variety of forms. The nominal stress σ and nominal strain ε use the original, or initial, cross section area A_o and height H_o of the pillar to convert the indenter force F and displacement Δ:

$$\sigma = \frac{F}{A_\mathrm{o}} \tag{3.4a}$$

$$\varepsilon = \frac{\Delta}{H_\mathrm{o}} \tag{3.4b}$$

The pillars produced by the top-down milling obtains a tapering, quantified by the taper angle α in Figure 3.4(b). Consequently, A_o will depend on where on the pillar it is calculated from. The deformation often initiates at the upper part of the pillar.

Therefore, the use of a cross section in this region might be the best selection for evaluating the stresses at which plasticity starts. On the other hand, if the aim is to look at the elastic response the cross section near the mid-height are a better choice for easy interpretation. The nominal stress–strain are accurate when the deformation is limited to some few percent of strains ($\varepsilon \lesssim 5\%$). At these levels, the geometrical changes caused by plasticity are small. When the deformation causes geometrical changes to the pillar this should be accounted for by applying the appropriate stress–strain calculations. For a material that deforms uniformly and continuously, the equations for the true stress σ_T and true strain ε_T

$$\sigma_\mathrm{T} = \frac{F}{A} \tag{3.5a}$$

$$\varepsilon_\mathrm{T} = \ln\left(1 + \frac{\Delta}{H_\mathrm{o}}\right) \tag{3.5b}$$

are applied. A is the actual cross section area which increases during loading. The nominal stress–strain values can be converted to true stress–strain values by the relations:

$$\sigma_\mathrm{T} = \sigma(1 + \varepsilon) \tag{3.6a}$$

$$\varepsilon_\mathrm{T} = \ln(1 + \varepsilon) \tag{3.6b}$$

Notice that Equations (3.5) and (3.6) require that F and Δ are defined as negative during compression.

Early in the compression experiment, the deformation is minimal, it do not cause much geometrical changes and the nominal and true stress–strain values are almost the same. If the pillar is deformed severely the deformation can be uniform throughout the pillar or localised to a part of the pillar. The true stress–strain values obtained from Equation (3.5) are well suited for the uniform deformation. When the deformation is localised it is often confined to the upper part of the pillar, often along defined planes across the pillar, and the formulas become inaccurate. Hence, the most accurate stress calculations depend on the type and the amount of the deformation. The best measurements are obtained by measuring the cross section where the deformation happened and calculate the stresses acting on the region. In crystalline materials the stress–strain can be converted to resolved shear stresses τ by applying Equation (2.1a). τ is well suited for localised deformation where the deformation happens by crystallographic slip on a defined slip plane along its slip direction.

3.2.3 Deformation of Pillars

The *microcompression test* was introduced for about a decade ago [7–9] and have been applied on a vast variation of materials, see references [48, 59–61] for reviews on the topic. The deformation of pillars differs in several ways from experiments conducted at a larger scale, *e.g.* deformation of mm-sized single crystals as presented in Section 2.7. This section introduces some of the characteristic features observed during pillar compression testing, with a focus on bcc metals.

Figure 3.9 [47] presents a set of *stress–strain curves* from [001] oriented W pillars over a range of diameters. The flow curves of the largest pillars ($D \gtrsim 1$ μm) are relatively smooth, with a smooth transition from elastic deformation to continuous plastic flow. Smaller pillars ($D \lesssim 1$ μm) obtain a jerky appearance in the flow curves. The deformation contain rapid strain bursts separated by loading segments, which appear to be nearly linear elastic. The transaction from smooth to jerky plastic flow is related to the underlying dislocation structure and the dislocation density (ρ). The pillar diameter where the transition happens is typically set equal to the average length between dislocations:

$$l_\rho = \frac{1}{\sqrt{\rho}} \tag{3.7}$$

The flow stresses from the pillars increase rapidly as the pillar diameter decreases. It was early established that the plastic flow of FIB prepared pillars follows the power law relation:

$$\sigma = K{D_\mathrm{t}}^{-n} \tag{3.8}$$

K is the power law coefficient and n is the power law exponent. The size effect for fcc metals follows the same scaling, with $n \approx 0.6$ [48], while in bcc metals n spans over a larger range, between 0.2–1 [21, 22, 47, 62–64]. Several forms of the scaling law and models have been developed for the physical interpretation of the size dependent plastic flow in fcc and bcc metals, see [65] for an overview.

The pillar diameter plotted against the stress, at a defined strain, become linear related in a double logarithmic plot. Figure 3.10 shows the flow stress against the pillar diameter for the bcc metals W and Nb, and for comparison fcc Au. The pillars were loaded along [001] direction and the flow stresses differ between the datasets (see the legend). It is usual to compare the stresses early after yielding with the stresses

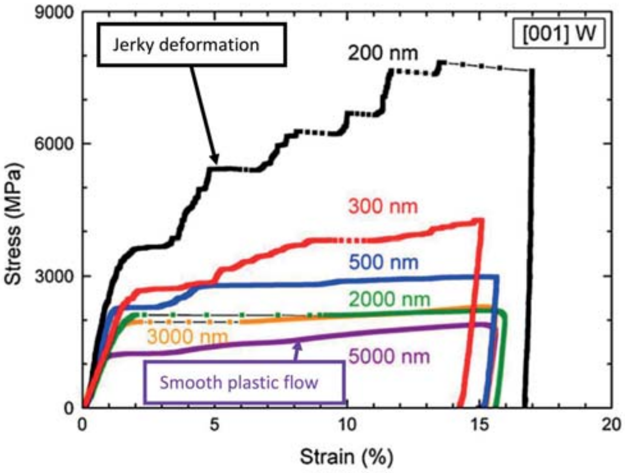

Figure 3.9: Stress–strain curves for [001] oriented W pillars over a range of diameters. Figure modified from [47].

after a portion of plastic flow. The point of yielding is not always straight forward to determine during pillar compression experiments. The stress at the first visible displacement burst, the offset yield point or the plastic stress early after yielding, *e.g.* at 2.5% strain, is often used to represent the yield stress. The stress near yielding is typically compared to the stress after 5–10% deformation. The comparison are used to quantify the strain hardening of the pillars.

The power law exponent in the bcc metals W, Nb and Ta are found to be orientation independent for the investigated crystal orientations [22, 67], while Mo shows an orientation dependency [68]. A stronger correlation are seen between n and the test temperature T, where n approaches the values of fcc metals when T approaches the critical temperature (T_c) [22, 47, 62]. The critical temperature, or the athermal temperature, is the temperature above which the flow stress becomes insensitive to the test temperature. Figure 3.11 shows the relation between the exponent (defined as $-n$ in Figure 3.11) and the normalised test temperature T/T_c.

Compression of pillars are typically done in a load controlled setup, where the load are incrementally increased according to a predefined loading rate ($\dot{F}$). The material responds with displacement bursts, corresponding to the strain bursts in Figure 3.9.

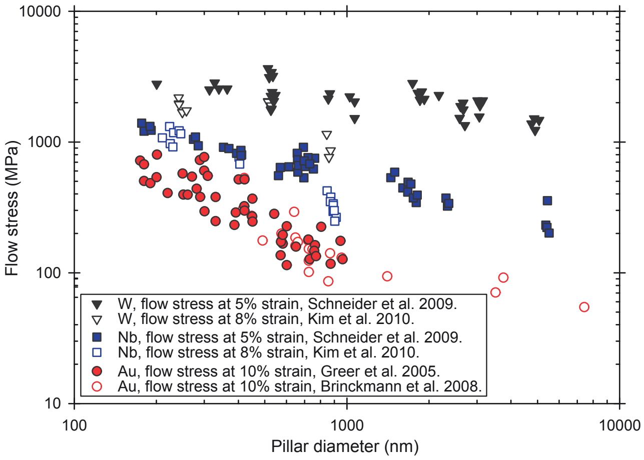

Figure 3.10: Plot of pillar diameter against flow stress for the bcc metals W [21, 47] and Nb [21, 47], and fcc Au [9, 66]. The flow stresses differ between the datasets (see the legend) and the pillars was compressed along ⟨001⟩ axes.

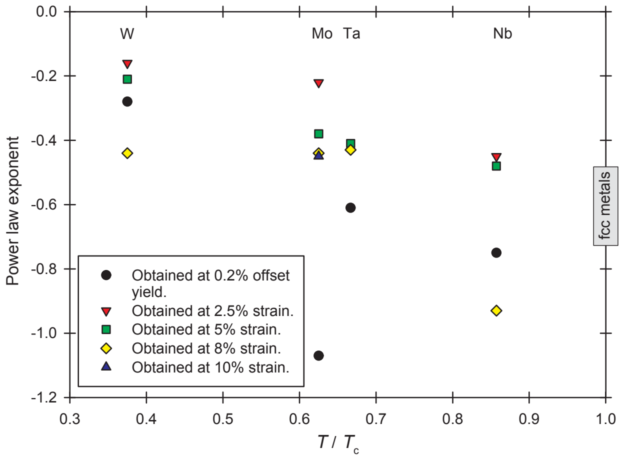

Figure 3.11: The power law exponent dependency on the normalised athermal temperature T/T_c. The power law exponents (defined as negative in the plot) was calculated from stresses obtained at different strains (see the legend) for pillars compressed along ⟨001⟩ axes. Data in the figure were obtained from [21, 22, 47, 66].

In a setup with displacement control the material responds with load drops, or stress drops in the flow curve, during the applied displacement rate ($\dot{\Delta}$).

Few pillar compression studies of bcc pillars have explored the *slip system* responsible for the plastic deformation [53, 69–71]. Based on SEM observations of slip bands, Kim *et al.* [70] reported that Nb pillars loaded along $\langle 001 \rangle$ axes most likely deformed along $\{110\}$ planes. Marichal *et al.* [53] deformed W pillars, loaded along [155] and [256] axis of pillars with circular and quadratic cross sections. They described how $\{112\}$ slip traces can form from elementary steps on two $\{110\}$ planes and used *in situ* Laue diffraction measurements during compression to verify the elementary deformation. Slip traces of the deformed surface, seen from SEM images, show steps along $\{112\}$ and $\{110\}$ planes. Another observation of slip planes were done by Xie *et al.* [71]. From *in situ* TEM observations, they reported that single crystal ferrite "nanoblades" of a HSLA steel glided initially on the $(0\bar{1}1)$ plane when loading in $[\bar{2}\bar{1}1]$ direction. The slip bands were overall wavy as an effect of collective deformation of multiple slip planes.

References

[1] T. L. Altshuler and J. W. Christian. The mechanical properties of pure iron tested in compression over the temperature range 2 to 293 °K. *Philosophical Transactions of the Royal Society of London. Series A, Mathematical and Physical Sciences*, 261 (1121):253–287, 1967.

[2] D. F. Stein, J. R. Low Jr, and A. U. Seybolt. The mechanical properties of iron single crystals containing less than 5×10^{-3} ppm carbon. *Acta Metallurgica*, 11 (11):1253–1262, 1963.

[3] S. S. Brenner. Tensile strength of whiskers. *Journal of Applied Physics*, 27(12): 1484–1491, 1956.

[4] A. Martín-Meizoso, I. Ocaña Arizcorreta, J. Gil-Sevillano, and M. Fuentes-Pérez. Modelling cleavage fracture of bainitic steels. *Acta Metallurgica et Materialia*, 42 (6):2057–2068, 1994.

[5] A. Lambert-Perlade, A. F. Gourgues, J. Besson, T. Sturel, and A. Pineau. Mechanisms and modeling of cleavage fracture in simulated heat-affected zone microstructures of a high-strength low alloy steel. *Metallurgical and Materials Transactions A*, 35A(3A):1039–1053, 2004.

[6] A. Pineau. Development of the local approach to fracture over the past 25 years: Theory and applications. *International Journal of Fracture*, 138(1):139–166, 2006.

[7] M. D. Uchic, D. M. Dimiduk, J. N. Florando, and W. D. Nix. Sample dimensions influence strength and crystal plasticity. *Science*, 305(5686):986–989, 2004.

[8] M. D. Uchic and D. A. Dimiduk. A methodology to investigate size scale effects in crystalline plasticity using uniaxial compression testing. *Materials Science and Engineering A*, 400:268–278, 2005.

[9] J. R. Greer, W. C. Oliver, and W. D. Nix. Size dependence of mechanical properties of gold at the micron scale in the absence of strain gradients. *Acta Materialia*, 53 (6):1821–1830, 2005.

[10] V. G. Haugen, B. R. S. Rogne, O. M. Akselsen, C. Thaulow, and E. Østby. Local mechanical properties of intercritically reheated coarse grained heat affected zone in low alloy steel. *Materials & Design*, 59:135–140, 2014.

[11] B. R. S. Rogne, C. Thaulow, and A. Barnoush. Micromechanical testing of fracture initiation sites in welded high-strength low-alloy steel. *Metallurgical and Materials Transactions A*, 45A(4):1996–2003, 2014.

[12] B. R. S. Rogne and C. Thaulow. Strengthening mechanisms of iron micro pillars. Manuscript submitted to *Philosophical Magazine*, 2013.

[13] B. R. S. Rogne and C. Thaulow. Effect of crystal orientation on the strengthening of iron micro pillars. Manuscript submitted to *Materials Science and Engineering A*, 2014.

[14] B. R. S. Rogne. Stål for arktiske forhold – teorier, tester og metoder. Project thesis (in norwegian), Norwegian University of Science and Technology, 2009.

[15] B. R. S. Rogne. Application of focused ion beam (FIB) on arctic steels. Master's thesis, Norwegian University of Science and Technology, 2010.

[16] B. R. S. Rogne and C. Thaulow. Investigation of nanomechanical test methods on arctic steels. *Proceedings of the Twenty-first (2011) International Offshore and Polar Engineering Conference*, pages 426–431, 2011.

[17] V. Haugen, B. R. S. Rogne, O. M. Akselsen, C. Thaulow, and E. Østby. On local properties of microstructures in welding. *Proceedings of the Twenty-second (2012) International Offshore and Polar Engineering Conference*, pages 16–22, 2012.

[18] J. L. Stewart, L. Jiang, J. J. Williams, and N. Chawla. Prediction of bulk tensile behavior of dual phase stainless steels using constituent behavior from micropillar compression experiments. *Materials Science and Engineering A*, 534:220–227, 2012.

[19] Y. Mine, K. Hirashita, H. Takashima, M. Matsuda, and K. Takashima. Microtension behaviour of lath martensite structures of carbon steel. *Materials Science and Engineering A*, 560:535–544, 2013.

[20] J. R. Greer, C. R. Weinberger, and W. Cai. Comparing the strength of f.c.c. and b.c.c. sub-micrometer pillars: Compression experiments and dislocation dynamics simulations. *Materials Science and Engineering A*, 493(1-2):21–25, 2008.

[21] J.-Y. Kim, D. Jang, and J. R. Greer. Tensile and compressive behavior of tungsten, molybdenum, tantalum and niobium at the nanoscale. *Acta Materialia*, 58(7): 2355–2363, 2010.

[22] A. S. Schneider, C. P. Frick, B. G. Clark, P. A. Gruber, and E. Arzt. Influence of orientation on the size effect in bcc pillars with different critical temperatures. *Materials Science and Engineering A*, 528(3):1540–1547, 2011.

[23] D. F. Stein and J. R. Low Jr. Effects of orientation and carbon on the mechanical properties of iron single crystals. *Acta Metallurgica*, 14(10):1183–1194, 1966.

[24] W. Spitzig and A. Keh. Orientation and temperature dependence of slip in iron single crystals. *Metallurgical and Materials Transactions B*, 1(10):2751–2757, 1970.

[25] M. Fukamachi. Surface orientation dependence of the tensile strength of plates of iron single crystal. *Japanese Journal of Applied Physics*, 11(9):1259–1264, 1972.

[26] C. H. Ersland and C. Thaulow. *Modeling of size and strain rate effects in compression tests of iron nanopillars*, pages 1–11. in *Atomistic modeling of failure in iron*, C.H. Ersland, Ph.d. diss. Norwegian University of Science and Technology, 2012.

[27] M. Friák, M. Šob, and V. Vitek. Ab initio calculation of tensile strength in iron. *Philosophical Magazine*, 83(31-34):3529–3537, 2003.

[28] T. A. Parthasarathy, S. I. Rao, D. M. Dimiduk, M. D. Uchic, and D. R. Trinkle. Contribution to size effect of yield strength from the stochastics of dislocation source lengths in finite samples. *Scripta Materialia*, 56(4):313–316, 2007.

[29] Y. Aono, E. Kuramoto, and K. Kitajima. Plastic deformation of high-purity iron single crystals. *Reports of Research Institute for Applied Mechanics (Kyushu University)*, 29(92):127–193, 1981.

[30] A. J. Schwartz, M. Kumar, B. L. Adams, and D. Field. *Electron Backscatter Diffraction in Materials Science*. Springer Science+Business Media, 2 edition, 2010.

[31] A. Argon. *Strengthening Mechanisms in Crystal Plasticity*. OUP Oxford, 2012.

[32] J. P. Hirth and J. Lothe. *Theory of Dislocations*. John Wiley & Sons, 2 edition, 1982.

[33] D. Hull and D. J. Bacon. *Introduction to Dislocations*. Elsevier Science, 5 edition, 2011.

[34] G. I. Taylor. The deformation of crystals of β-brass. *Proceedings of the Royal Society of London. Series A, Containing Papers of a Mathematical and Physical Character*, 118(779):1–24, 1928.

[35] G. Taylor. Thermally-activated deformation of bcc metals and alloys. *Progress in Materials Science*, 36:29–61, 1992.

[36] A. Seeger and W. Wasserbäch. Anomalous slip – a feature of high-purity body-centred cubic metals. *physica status solidi (a)*, 189(1):27–50, 2002.

[37] E. J. Mittemeijer. *Fundamentals of Materials Science: The Microstructure–Property Relationship Using Metals as Model Systems*. Springer, 2010.

[38] R. G. Garlick and H. B. Probst. Investigation of room-temperature slip in zone-melted tungsten single crystals. *Transactions of the Metallurgical Society of AIME*, 230:1120–1125, 1964.

[39] A. Seeger. Experimental evidence for the {110} ↔ {112} transformation of the screw-dislocation cores in body-centred cubic metals. *physica status solidi (a)*, 201 (4):R21–R24, 2004.

[40] W. Fahrenhorst and E. Schmid. Über die plastische dehnung von α-eisenkristallen. *Zeitschrift für Physik*, 78(5-6):383–394, 1932.

[41] A. J. Opinsky and R. Smoluchowski. The crystallographic aspect of slip in body-centered cubic single crystals. I. Theoretical considerations. *Journal of Applied Physics*, 22(11):1380–1384, 1951.

[42] G. I. Taylor and C. F. Elam. The distortion of iron crystals. *Proceedings of the Royal Society of London. Series A, Containing Papers of a Mathematical and Physical Character*, 112(761):337–361, 1926.

[43] A. S. Keh. Work hardening and deformation sub-structure in iron single crystals deformed in tension at 298 °K. *Philosophical Magazine*, 12(115):9–30, 1965.

[44] L. A. Giannuzzi. *Introduction to Focused Ion Beams: Instrumentation, Theory, Techniques and Practice*. Springer Science+Business Media, 2005. 357 pages.

[45] N. Yao. *Focused Ion Beam Systems: Basics and Applications*. Cambridge University Press, 2007.

[46] C. A. Volkert and A. M. Minor. Focused ion beam microscopy and micromachining. *MRS Bulletin*, 32(5):389–395, 2007.

[47] A. S. Schneider, D. Kaufmann, B. G. Clark, C. P. Frick, P. A. Gruber, R. Monig, O. Kraft, and E. Arzt. Correlation between critical temperature and strength of small-scale bcc pillars. *Physical Review Letters*, 103(10):105501/1–4, 2009.

[48] M. D. Uchic, P. A. Shade, and D. M. Dimiduk. Plasticity of micrometer-scale single crystals in compression. *Annual Review of Materials Research*, 39:361–386, 2009.

[49] C. A. Volkert and E. T. Lilleodden. Size effects in the deformation of sub-micron Au columns. *Philosophical Magazine*, 86(33-35):5567–5579, 2006.

[50] D. Kiener, C. Motz, and G. Dehm. Dislocation-induced crystal rotations in micro-compressed single crystal copper columns. *Journal of Materials Science*, 43(7): 2503–2506, 2008.

[51] D. Kiener, C. Motz, and G. Dehm. Micro-compression testing: A critical discussion of experimental constraints. *Materials Science and Engineering A*, 505(1-2):79–87, 2009.

[52] D. Kaufmann, A. S. Schneider, R. Mönig, C. A. Volkert, and O. Kraft. Effect of surface orientation on the plasticity of small bcc metals. *International Journal of Plasticity*, 49:145–151, 2013.

[53] C. Marichal, H. Van Swygenhoven, S. Van Petegem, and C. Borca. {110} slip with {112} slip traces in bcc tungsten. *Scientific Reports*, 3:1–7, 2013.

[54] A. C. Fischer-Cripps. *Nanoindentation*. Springer, 3 edition, 2011.

[55] Synton-MDP. Micro Diamond Points. Downloaded 2. June 2010. `http://www.synton-mdp.ch`/images/produkte/.

[56] I. N. Sneddon. The relation between load and penetration in the axisymmetric boussinesq problem for a punch of arbitrary profile. *International Journal of Engineering Science*, 3(1):47–57, 1965.

[57] H. Zhang, B. E. Schuster, Q. Wei, and K. T. Ramesh. The design of accurate micro-compression experiments. *Scripta Materialia*, 54(2):181–186, 2006.

[58] C. P. Frick, B. G. Clark, S. Orso, A. S. Schneider, and E. Arzt. Size effect on strength and strain hardening of small-scale [111] nickel compression pillars. *Materials Science and Engineering A*, 489(1-2):319–329, 2008.

[59] O. Kraft, P. A. Gruber, R. Mönig, and D. Weygand. Plasticity in confined dimensions. *Annual Review of Materials Research*, 40(1):293–317, 2010.

[60] J. R. Greer and J. T. M. De Hosson. Plasticity in small-sized metallic systems: Intrinsic versus extrinsic size effect. *Progress in Materials Science*, 56(6):654–724, 2011.

[61] R. Krahne, G. Morello, A. Figuerola, C. George, S. Deka, and L. Manna. Physical properties of elongated inorganic nanoparticles. *Physics Reports*, 501(3-5):75–221, 2011.

[62] A. S. Schneider, C. P. Frick, E. Arzt, W. J. Clegg, and S. Korte. Influence of test temperature on the size effect in molybdenum small-scale compression pillars. *Philosophical Magazine Letters*, 93(6):331–338, 2013.

[63] J.-Y. Kim and J. R. Greer. Size-dependent mechanical properties of molybdenum nanopillars. *Applied Physics Letters*, 93(10):101916/1–3, 2008.

[64] J.-Y. Kim and J. R. Greer. Tensile and compressive behavior of gold and molybdenum single crystals at the nano-scale. *Acta Materialia*, 57(17):5245–5253, 2009.

[65] S.-W. Lee and W. D. Nix. Size dependence of the yield strength of fcc and bcc metallic micropillars with diameters of a few micrometers. *Philosophical Magazine*, 92(10):1238–1260, 2012.

[66] S. Brinckmann, J.-Y. Kim, and J. R. Greer. Fundamental differences in mechanical behavior between two types of crystals at the nanoscale. *Physical Review Letters*, 100(15):155502/1–4, 2008.

[67] D. Kaufmann, R. Mönig, C. A. Volkert, and O. Kraft. Size dependent mechanical behaviour of tantalum. *International Journal of Plasticity*, 27(3):470–478, 2011.

[68] A. S. Schneider, B. G. Clark, C. P. Frick, P. A. Gruber, and E. Arzt. Effect of orientation and loading rate on compression behavior of small-scale Mo pillars. *Materials Science and Engineering A*, 508(1-2):241–246, 2009.

[69] C. R. Weinberger, B. L. Boyce, and C. C. Battaile. Slip planes in bcc transition metals. *International Materials Reviews*, 58(5):296–314, 2013.

[70] J.-Y. Kim, D. Jang, and J. R. Greer. Insight into the deformation behavior of niobium single crystals under uniaxial compression and tension at the nanoscale. *Scripta Materialia*, 61(3):300–303, 2009.

[71] K. Y. Xie, Y. B. Wang, S. Ni, X. Z. Liao, J. M. Cairney, and S. P. Ringer. Insight into the deformation mechanisms of α-Fe at the nanoscale. *Scripta Materialia*, 65 (12):1037–1040, 2011.

Appended Papers

Paper I

B. R. S. Rogne, C. Thaulow, and A. Barnoush.

Micromechanical Testing of Fracture Initiation Sites in Welded High-Strength Low-Alloy Steel.

Metallurgical and Materials Transactions A, 45A(4):1996–2003, 2014.

Is not included due to copyright

Paper II

B. R. S. Rogne and C. Thaulow.

Strengthening Mechanisms of Iron Micro Pillars.

Manuscript submitted to: *Philosophical Magazine.*

Philosophical Magazine
Vol. 00, No. 00, 00 Month 201x, 1–14

MANUSCRIPT

Strengthening Mechanisms of Iron Micro Pillars

B.R.S. Rogne[a*] and C. Thaulow[a]

[a]*Department of Engineering Design and Materials, Norwegian University of Science and Technology, No-7491 Trondheim, Norway*

(*Received 17 November 2013; Received in revised form 5 October 2014*)

We examine the size effect and strengthening mechanisms of bcc iron pillars. The single crystal pillars were machined with focused ion beam and tested with a nanoindentation device with the compression axis along the ⟨001⟩ crystallographic direction. We compare our test results with both older literature on whiskers and micro/macro specimens, and recent results from atomistic modelling. We find that the obtained results can be explained on the basis of current theories based on small scale plasticity.

Keywords: SEM; FIB; pillar compression testing; deformation mechanisms; plastic deformation; micromechanics; size effect; bcc iron

1. Introduction

The use of micro pillar compression testing [1–3] is becoming increasingly important in material science. The method have been growing in popularity due to the relatively simple and cost efficient procedures involved and the ability to extract material properties and examine deformation mechanisms in a restricted material volume. Micro or nano pillars can be precisely positioned at specific locations on the sample surface to study its resistance to plastic flow and gain insight to the underlying dislocation mechanisms. The focus of this study is to investigate the size dependent behaviour of the flow curve of iron ⟨001⟩ oriented nano and micro pillars and to gain insight to the operating dislocation mechanisms. Mechanical testing of focused ion beam (FIB) milled pillars at micron and nano scale has revealed that the size of the test sample do affect the test results. The increased strength with reduced size follow a power law that explains the general relationship (see [4–7] for reviews on the topic):

$$\sigma = K{D_\mathrm{t}}^{-n} \tag{1}$$

σ is the flow stress, D_t is the top-surface diameter of a cylindrical sample, K is the power law coefficient and n is the power law exponent.

It is generally agreed that the size strengthening is caused by change in dislocation mechanisms as the sample size is changed. The surface in the limited volume

---

[*] Corresponding author. Email: bjorn.rogne@ntnu.no

ISSN: xxxx-xxxx print/ISSN xxxx-xxxx online

DOI: x
http://www.informaworld.com

can cause dislocations to move out of the surface and leave the sample in a dislocation starved condition [2, 8, 9], or enhance the dislocations' ability to self-multiply near the surface [10, 11]. In addition, the dislocation sources, which becomes truncated because of the limited volume [12, 13], restricts the plasticity. Results on single crystal micro pillars have been published for a wide range of fcc [2, 10, 14–21](and references therein) and bcc metals [10, 18, 22–37]. However, there have not yet been published a thorough investigation of the size effect of bcc iron. This work investigates the size dependent mechanical behaviour and its mechanisms of $\langle 001 \rangle$ oriented bcc iron pillars.

In macroscopic samples the dislocations are available in a rich variety of configurations and the resistance for the dislocation to glide through the crystal, the critical resolved shear stress (τ_c), is dictated by the available sources and obstacles in the crystal. In tensile and compression experiments on pure single crystal of iron [38–40], conducted at room temperature and at quasistatic strain rates, the lowest τ_c is in the range of 10–15 MPa.

The available slip planes for bcc metals are of type $\{110\}$, $\{112\}$ and $\{123\}$. The selection of activated slip planes depends on the crystallographic loading axis, purity of the crystal, and experimental factors such as temperature and imposed strain rate [41, 42]. It is frequently claimed that at room temperature there is not enough energy to activate deformation along $\{123\}$ planes. However, experimental determination of the slip planes in iron at room temperature have identified all the three combinations in addition to slip traces that do not corresponds to a true crystallographic slip plane [40]. The latter deformation is observed along the maximum resolved shear stress plane (MRSSP) or on a non-crystallographic slip (NCS) plane. Deformation on the NCS plane is explained by collective deformation on several non-parallel active slip planes that appears to be slip traces along a non-existing slip plane. Spitzig and Keh [40] investigated the orientation and temperature dependence of slip in purified iron single crystals and found that the active slip planes depended on the loading direction of the crystal. At room temperature crystals located with a tensile axis in the centre of the standard stereographic triangle deformed through $\{110\}$ slip while in the periphery the deformation happened on a $\{112\}$ planes or a NCS plane [40]. Theoretical analysis done with kink-pair nucleation models identified slip predominately on the $\{112\}$ planes [41, 43]. Recently *in situ* transmission electron microscopy (TEM) tests [44] observed that dislocations are dominated by deformation on the $\{110\}$ plane when the tensile axis is in the centre of the stereographic triangle. These observations strengthen the observations by Spitzig and Keh [40].

The size strengthening of bcc iron was first investigated by Brenner [45] in 1956. He measured the tensile strength (equivalent to the upper yield stress) of iron whiskers that approached the theoretical value. The tested whiskers were almost defect free single crystals and the trend was evident — smaller is stronger. At that time the high strength of the small crystals, was explained by the lack of defects in small crystals and that large whiskers' growth is prone to produce defects. Fukamachi [46] established a size effect based on tensile tests of thin plates made of single crystal iron. He observed a strengthening effect when the plate thickness became less than about 30 µm. The strengthening was explained by the presence of dislocation loops where the dislocation segments that is parallel to the surface tends to move out through the surface. The dislocation segments of mixed character will consequently be straightened out and contribute less to the plasticity.

Atomistic simulations of single crystal iron nano pillars have been performed on defect free crystals at zero Kelvin and at strain rate ($\dot{\varepsilon}$) of 5×10^7 s^{-1} [47]. Even in these extreme conditions, the compressive strength (equivalent to upper yield

Table 1. Chemical composition of the iron sheet given in ppm by weight.

Al	C	Co	Cr	Cu	N	Ni	O	P	Si	Ta
13	27	17	4.3	4.9	2	9.1	69	1.4	22	< 10

stress) is not as high as theoretically predicted [48].

This paper presents the size effect for bcc iron micro and nano pillars loaded along the $\langle 001 \rangle$ crystallographic direction. The pillar diameters are ranging from some few hundreds of nanometers to some few microns. The size effect is explain based on novel dislocation theories and find that our data fit a mathematical expression originally developed for fcc metals.

2. Materials and experimental procedures

2.1. *Materials*

The test specimens are fabricated from an 1 mm thick cold rolled sheet of 99.99% pure iron, Table 1. The sheet was cut into 8 × 8 mm^2 square pieces with a fine cut-off grinding wheel before being ground with SiC paper, and polished with diamond particles and colloidal silica suspension. The samples were heat treated in a high vacuum furnace at 923 K (650°C) for 5 hours in order to produce enlarged grains. Final surface preparation was done by electropolishing to remove the surface deformations. After heat treatment, an average grain size of 29 ± 16 µm was measured.

Selected regions from the sample were scanned with a field emission scanning electron microscope (FE-SEM) where electron backscatter diffraction (EBSD) signals were detected. The indexed crystallographic orientations of the grains were evaluated in order to pick grains that had crystallographic $\langle 001 \rangle$ directions normal to the sample surface. In total 4 grains, within maximum 2° deviation from the desired orientation, were selected and used for FIB preparation of pillars.

2.2. *Pillar production*

Micro pillar specimens were milled out and imaged using a FIB/SEM DualBeam$^{\text{TM}}$ system (FEI Helios NanoLab$^{\text{TM}}$). The specimens were manufactured in a two-step procedure with an acceleration voltage of 30 kV. The first step uses a bitmap milling pattern to mill out an array of iron stumps at a high milling current (between 9 to 3 nA). The array was placed inside selected grains, Figure 1 (a). The second step uses a circular milling pattern at a lower current (920 to 93 pA) to refine the final shape, i.e. transform the stumps into pillars with final shape (Figure 1 (b)). Additional individual pillars were also produced from circular milling patterns in both the two steps. The second step is essential to minimize the sputtering rate and the energy spread of the beam. Consequently, this reduces the material redeposition and the size of the ion beam so that a well-defined pillar shape with a small taper angel (α) can be produced. 40 pillars were successfully tested and used in the analyses. The pillar diameter (D_{t}), measured at the top surface, ranged from about 140 nm to 4.3 µm. The aspect ratio, defined as the ratio between the pillar height (H) and D_{t}, varied between 2–4, except for some few of the largest specimens that had a slightly lower aspect ratio. The taper angle α varied between 1–5° with the largest tapering on the smallest pillars.

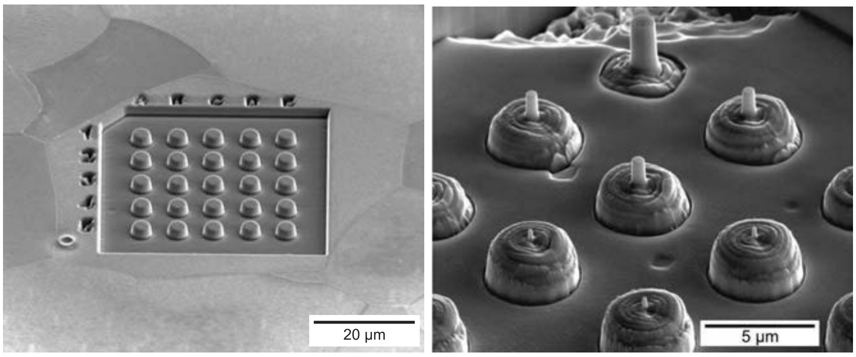

(a) (b)

Figure 1. SEM micrographs showing (a) an array of pre-milled stumps from the first high current milling step and (b) pillar samples after the second low current milling step.

2.3. *Nanomechanical testing*

After manufacturing, the sample was transferred to a Hysitron TI 750 Ubi™ nanoindentation system with a Performech® control unit and loaded with a flat-punch diamond indenter from Synton-MDP in the open-loop load control mode. The flat punch tip had a diameter of 5 µm and a 60° cone angle. Before loading, the tip was positioned approximately over the pillar from the optical position of the instrument and further adjusted by using the tip scan mode to identify the accurate position of the pillar [49]. The well-defined array of pillars made it possible to load a fraction of the samples without using the tip scanning prior compression. The logged force (F) and displacement (Δ) output were converted to engineering stress (σ) and engineering strain (ε) by using H and D_{t} in the calculations. The load functions consisted of a constant loading rate ($\dot{F}$) up to a maximum load followed by a rapid unloading. The applied $\dot{F}$ varied between 6–160 $\mu\mathrm{N\,s^{-1}}$ and were chosen so that the stress rate ($\dot{\sigma}$); calculated as $\dot{\sigma} = \dot{F}/A$, where $A = (\pi/4)D_{\mathrm{t}}{}^2$; was close to 200 $\mathrm{MPa\,s^{-1}}$. The loading rate was fast enough to avoid a measurable influence from system drift in the smallest pillars. The corresponding strain rate $\dot{\varepsilon}$ is about 1×10^{-3} $\mathrm{s^{-1}}$ based on a linear strain rate $\dot{\varepsilon} = \dot{\sigma}/E$, with the Young's modulus (E) of 200 GPa. By choosing a constant $\dot{\sigma}$ we avoid strain/stress rate effects that could complicate the interpretation of the results.

2.4. *Analysis of slip traces*

Traces of crystallographic slip, or slip bands, on the pillar surface have been compared with the slip traces calculated from EBSD scan. The slip systems considered in the analysis were of type $\{110\}\langle 111\rangle$ and $\{112\}\langle 111\rangle$. In the selected orientation $\langle 001\rangle$, the slip direction $\langle 111\rangle$ have four symmetrical directions as illustrated in Figure 2 (a). Along each direction there is one preferred plane of type $\{112\}$ and two of type $\{110\}$ as shown in Figure 2 (b) and (c), respectively. The Schmid factor (S) of the two types are $S_{\{112\}} = 0.47$ and $S_{\{110\}} = 0.41$, where the subscript indicates the family of planes.

As initial condition the slip plane normals for the two families of planes are defined together with the unit cube and transformed into the grain orientation. The rotation transformation matrix uses the Euler angles, of type Bunge, from the grain orientation to rotate the vectors. The grain orientations were obtained from

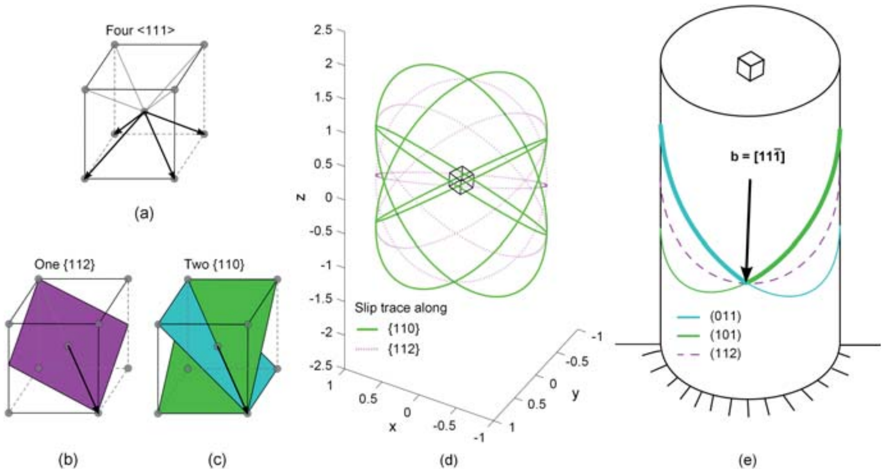

Figure 2. Illustration of (a) the four symmetrical slip directions of type ⟨111⟩ in the bcc unit cell, (b) the favourably positioned slip plane of type {112} along one of the slip directions, (c) the two favourably positioned slip plane of type {110} along one of the slip directions, (d) calculated slip traces on the surface of a cylindrical pillar and (e) plot of slip traces along one of the directions.

the EBSD scan and represent the average value of the grain. The z-coordinate of the transformed planes were calculated by sweeping along a circle in the z-plane, or the cylinder surface, to form an elliptic intersection. Before EBSD scanning and SEM imaging, the stage was carefully aligned to a reference position. The stage rotation and tilting from the reference position were registered and used to define the camera view of the 3D plot. The resulting plot is seen in Figure 2 (d) and includes the most favourable, in terms of the Schmid factor S, slip traces. In Figure 2 (e) the slip traces from planes gliding along one of the slip directions are drawn on a cylindrical pillar.

The pillars used in the slip trace analysis had a diameter close to 1 μm and were only plastically deformed to some few percent. The limited amount of plastic deformation makes it possible to observe the slip traces on the pillars surface and to minimize geometrical changes and crystal rotation that happens during severe loading. The orientation, with loading along the ⟨001⟩ direction, were selected in such a way that the samples were expected to deform in multiple slip along one or both of the slip systems of type {110} ⟨111⟩ or {112} ⟨111⟩ as illustrated in Figure 2.

3. Results

3.1. *Crystallographic slip*

Figure 3 shows a selection of SEM micrographs of slightly deformed micro pillars with diameters from 150 nm to 1 μm. The slip traces on the pillar surface are clearly visible for the largest pillars and less resolved on the smallest pillars. To avoid wrong indexing of the slip traces only the largest pillars were considered. One of the pillars that had D_{t} close to 1 μm is shown in Figure 4, viewed from three positions. Because of the four symmetrical slip directions, we observe the same type of slip traces in all the three views. Along each of the four symmetric ⟨111⟩ glide directions there are two equivalent {110} planes and one {112} plane. The three possibilities are drawn on Figure 2 (e). Close examination of the slip traces near the top-surface reveals that the slip actually happens partly on the two non-parallel slip planes of type {110}, marked by thick lines in Figure 4 (c). If the

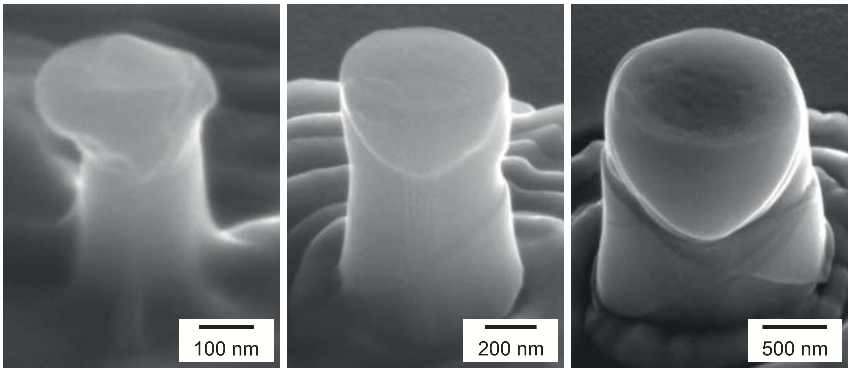

(a) (b) (c)

Figure 3. Post compression SEM micrographs of pillar with diameters close to (a) 150 nm (b) 500 nm and (c) 1 µm. The deformation was limited to some few percentage of strain.

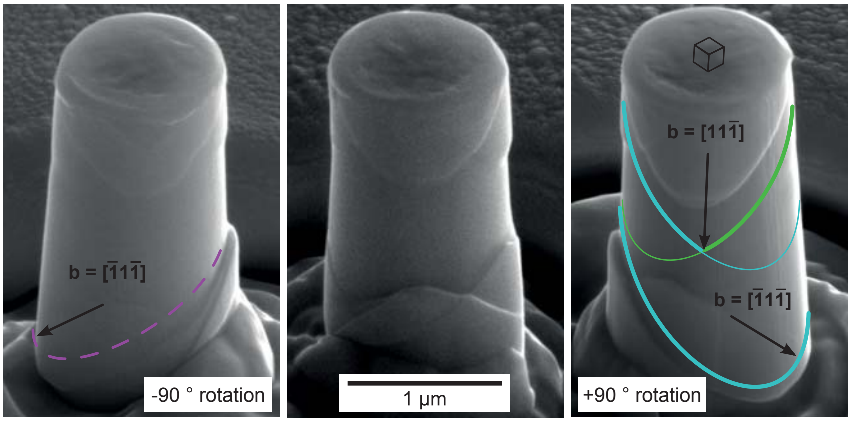

(a) (b) (c)

Figure 4. Post compression SEM micrographs of one pillar with diameter close to 1 µm. The pillar is viewed from three different positions, (a), (b) and (c), where the stage has been rotated 90° between the views. Selected slip directions and slip traces are indicated on the pillar surface.

slip direction is taken to be the $[11\bar{1}]$ direction, the slip traces corresponds to glide partly on (101) and (011) planes. Another slip trace close to the base corresponds to slip along $[1\bar{1}\bar{1}]$ direction on the (011) plane. In some few cases the slip traces matches slip on {112} planes, like in the dashed line in Figure 4 (a).

Overall, the slip traces corresponded very well with the calculations. The slip planes along one or two of the slip directions are sometimes governing the plastic deformation. Slip planes of type {110} with $S_{\{110\}} = 0.41$ are most frequently observed. Other slip planes, that appear to be from both the {110} and {112} families, are occasionally activated. This is presumable a consequence of geometrical changes during plasticity and changes in loading condition. Now and then, the slip traces were undefined and can correspond to activation of a combination of several slip systems, possible through cross slip.

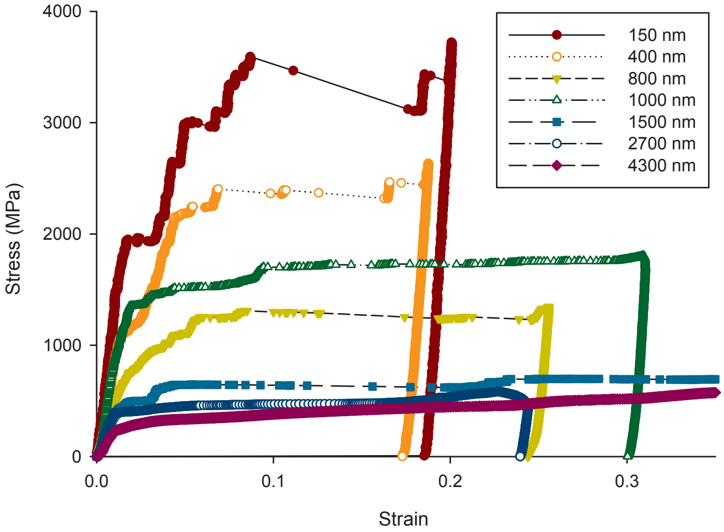

Figure 5. Stress–strain curves of ⟨001⟩ oriented pillars with diameter ranging from 150 nm to 4.3 μm. The pillar diameter of the samples are indicated in the legend.

3.2. *Flow curves and the power law relation*

Selections of representative stress–strain curves for different sized pillars are shown in Figure 5. For the pillars with $D_t < 1$ μm the selected stress–strain curve undergoes a plastic flow at intermediate stresses, i.e., other pillars of the same size deformed at both higher and lower flow stresses. The largest pillars show a smooth plastic flow through the stress–strain curves with a moderate strain hardening. For the smaller pillars ($D_t < 1$μm) the initial plastic flow, up to about $\varepsilon < 0.1$, is rather smooth with only small strain bursts. In this region, the strain hardening is much higher than for the largest pillars. At increased strains the bursts becomes larger and appears as rapid strain bursts separated by segments with linear elastic loading [8, 50]. The same characteristics have frequently been observed for both fcc and bcc materials (e.g. [10, 15, 29, 30, 33]).

To quantify the size–strengthening effect the yield stress (σ_y), defined as the stress at 0.2% offset strain, was plotted as a function of D_t in the double logarithmic plot in Figure 6. The power law relation in Equation (1) describes empirically the strengthening. In the curve fitting n was calculated to be 0.60 and K to be 702 MPa μm^n. In order to report values that are comparable to references in the literature, similar values were extracted for the flow stress at 2.5 ($\sigma_{2.5\%}$) and 5% strain ($\sigma_{5\%}$), and are summarized in Table 2. The exponent does not vary much with the strain and is in the upper range of the earlier reported values for bcc metals (where n typically is in the range 0.2–0.5) and near the lower range for fcc metals (0.6–1.0). According to Schneider et al. [25, 30, 51] the measured exponent n for bcc metals depends on the test temperature (T) and approaches the values of fcc metals when the temperature goes towards the critical temperature (T_c), the so-called athermal temperature. T_c is the temperature above which the flow stress becomes insensitive to the test temperature. The exponent data obtained from $\sigma_{2.5\%}$ and $\sigma_{5\%}$ should, in terms of experimental conditions, be directly comparable to the values reported in [25, 30, 51]. The critical temperature of iron is about

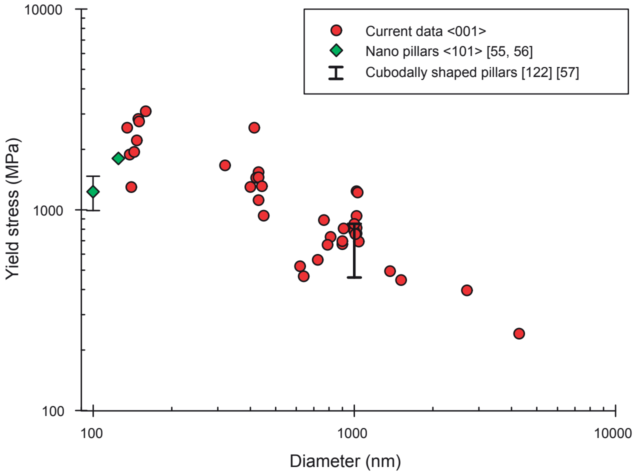

Figure 6. Yield stress (σ_y), stress at 0.2% offset strain, as a function of pillar diameter (D_t) for $\langle 001\rangle$ oriented pillars. Comparable values from compression of nano pillars [55, 56] and cuboidal shaped pillars [57] are added for comparison. The smallest dimension of the sample was used for plotting results from [57].

Table 2. Overview of the exponent (n) and coefficient (K) in the power law obtained at different stress definitions.

	n	K (MPaμm^n)
σ_y	0.60	702
$\sigma_{2.5\%}$	0.55	808
$\sigma_{5\%}$	0.59	1023

330 K [52, 53], hence the ratio $T/T_c = 298/330 = 0.9$. The exponents found in the current experiments fit remarkably well with the expected values from the trend found by Schneider et al. [25, 30, 51], where the extrapolated exponent is about 0.45 if the stress is measured at 2.5% strain and close to 0.55 if it is measured at 5% strain. Recently, Malygin [54] explained the size effect in the framework of a dislocation-kinetic approach. The results show that the exponent should increase rapidly towards values found for fcc metals as the test temperature approaches the critical temperature. This is in accordance with the current results.

4. Discussion

4.1. *Slip systems*

The slip trace analysis revealed that the majority of slip traces were of type {110}. However, the crystallographic slip in bcc metals is known to be complex and several possible mechanisms must be taken into consideration: available slip systems, cross slip and NCS. The bcc metals deform along the closest packed $\langle 111\rangle$ directions on one, or a combination of the {110}, {112} and {123} families of crystallographic slip planes [58]. The large number of possible slip planes close to each other (12 planes for each of the 4 slip directions) complicates the slip trace analysis and introduces uncertainties in picking the wrong plane even for idealised slip traces that only follows one plane. A small rotation of the crystal, which usually happens during plastic deformation of single crystals, can potentially bias the analysis. In the current analysis, only the two most frequently reported slip planes [40–42], of type {110} and {112}, were considered. Because of the repeatability of the analysis we believe that the determined planes are correct and that they predominantly are of type {110}. In some few instances, the slip traces was identified to follow {112} planes. However, the calculated slip traces (Figure 2 (d)) indicates that crystallographic slip on {112} planes should produce slip traces that appear as nearly horizontal lines on the pillar surface. Such nearly horizontal line is seen as pink dashed line in Figure 2 (d) and has not been observed on the pillar surface. Second, the slip might not entirely happen along one defined slip plane. NCS [59], i.e. where the slip appears to occur on an undefined slip plane, is readily observed at and above room temperature. In this type of deformation, the movement of the screw dislocations is determined by the local stresses and the different types of nearby planes through cross slip. Such deformation traces have a wavy appearance and are ill-defined. The slip traces in the present investigations appear as well-defined and not wavy. Hence, we conclude neither the NCS nor the contribution from cross-slip are determinant mechanisms in the current experiments.

Caillard [44] recently investigated the dislocation motion when straining along the $[1\bar{4}3]$ axis of a thin film of iron at room temperature through *in situ* TEM experiments on a high purity iron (C, N, O and Si was 2.5-4 ppm by weight). He observed the {110} planes as the preferred slip plane. Landau et al. [56] studied iron nano pillars compressed along the $\langle 101 \rangle$ axes and identified the {110} as the most likely slip planes. This is in accordance with our results where the {110} planes were activated despite higher shear stresses on the {112} planes.

4.2. *Strengthening mechanisms*

4.2.1. Impurity elements

Strengthening mechanisms in single crystal plasticity, such as interstitial solute atoms and dislocation density, may be important contributors and effect the deformation behaviour in pillars. The shear strength of large samples, in mm size, of high purity single crystal iron can go below 10 MPa [52, 60] at room temperature. Increased amounts of impurity elements produce, in general, more obstacles in the crystal that hinder the movement of dislocations and cause an increased shear strength. Since our material is not an ultrapure iron (see Table 1) it contains defects that will increase the resistance to plastic flow. Previous studies on iron with varying impurity contents [39, 61] confirm the importance of interstitial solute atoms in the strengthening of crystals. Based on these results we estimate a strengthening effect of C and O, Table 1, to about 40 MPa. The strengthening from impurities will be the same in all pillar dimensions, and should not influence on the size dependence as described in Section 3.2 and discussed in Section 4.2.4.

4.2.2. Dislocation density

In well annealed samples, the typical dislocation density (ρ) is in the range of 10^{10}–10^{12} m^{-2} [58]. Since the material used was a polycrystalline iron sample, where series of pillars were tested in 4 different grains, the local ρ is expected to vary significantly. For instance, due to annealing effects, the ρ will be lower near the grain boundary than in the centre of the grain, and also depend on the grain size. In a recent TEM study of dislocation structure in as-grown and prestrained Mo alloy fibres by Sudharshan Phani et al. [62], the observed dislocation density and their distribution were correlated with stress–strain curves obtained by Bei et al. [63]. The stress–strain curves were obtained from pillar compression experiments where the 4% prestrained fibers with a diameter of about 550 nm deformed similar to the

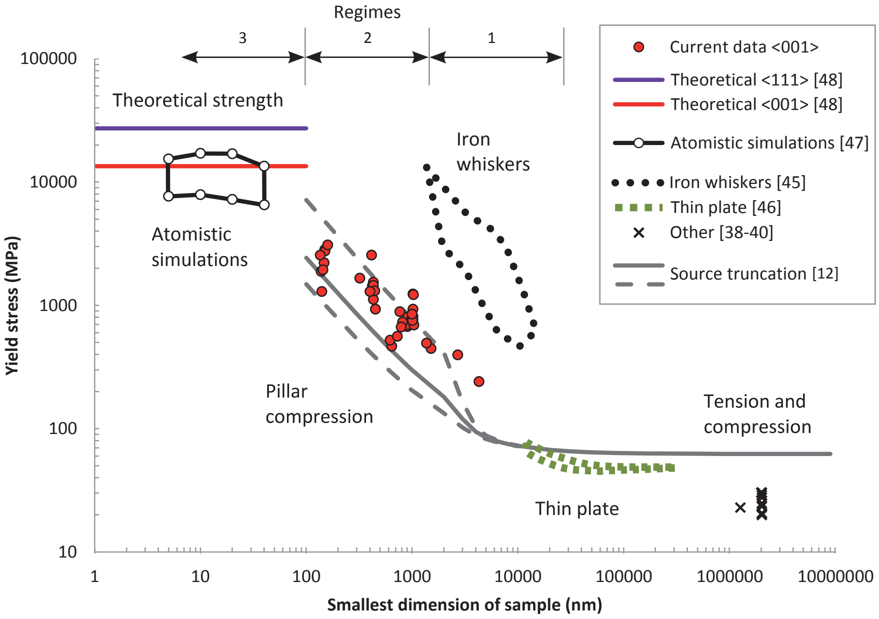

Figure 7. Yield stress (σ_y) of different sized single crystal iron samples. Range of data from the literature are included for comparison and were obtained from: theoretical [48], atomistic simulations [47], iron whiskers [45], thin plate [46] and other [38–40]. The predicted size effect was calculated based on the source truncation model [12]. The upper and lower limits (dashed grey lines), of the model, were obtained by reducing or increasing the dislocation segment length by one standard deviation.

submicron pillars in Figure 5. The scatter in yield stresses are comparable to our results in Figure 6, with a variation between the lowest and highest value of about 3 times.

4.2.3. Size dependence

The current results are plotted together with available data on single crystal iron samples of various types in Figure 7. As upper strength limit we used the calculations of the theoretical tensile strength based on density functional theory calculations [48]. Here the upper limit for loading along [001] was 12.7 GPa and along [111] was 27.3 GPa. Results from molecular dynamic (MD) simulations of defect-free single crystal iron nano pillars [47] were conducted at 0 K and at a strain rates of 5×10^7 s^{-1} and are therefore different from the experiments. Plasticity starts at the base of the pillar by emitting dislocations from the surface that consequently moves upwards through the crystal. The atomistic simulations, with surface nucleated dislocations, can be considered as an upper limit to the micro pillar compression experiments. As seen in Figure 7, the strength levels from MD simulations were lower than the density functional theory calculations.

Experimentally, Brenner [45] measured the fracture stress of iron whiskers with results that approached the theoretical value. The whiskers were single crystals close to defect free and the deformation was expected to nucleate from the surface. The σ_y obtained in the current experiments were in the same range as for the iron whiskers, but for samples that were at least one order of magnitude smaller. The difference is likely to be caused by the fact that the micro pillars were not defect free and the plasticity can start as soon as the stress is high enough for moving an existing dislocation.

In terms of initial dislocation density and impurities, the experimental results from Fukamachi [46] should coincide with the present material. Fukamachi investigated the effect of surface orientation on tensile testing of thin metal plates loaded in the [110] direction. Tensile and compression experiments on single crystal iron [38–40], conducted at room temperature and at quasistatic strain rates, give a low yield stress of about 20–30 MPa.

We now compare our results with the source truncation model by Parthasarathy et al. [12]. In the calculations we use shear modulus $G = 77.5$ GPa and magnitude of Burgers vector $b = 0.248$ nm, and assume a dislocation density $\rho = 1{\times}10^{12}\ \mathrm{m}^{-2}$ and internal friction stress $\tau_0 = 16$ MPa (corresponding to $S_{\{110\}} \cdot 40$ MPa). Further it is assumed a distribution of source length (distance from dislocation pinning point to the nearest surface) with related standard deviation as presented by Parthasarathy et al. [12]. In the source truncation model it is assumed that one out of the 12 slip systems of type $\{110\}\,\langle 111\rangle$ is favoured and the slip happens at about 45° from the loading axis. The upper and lower limits are obtained by reducing or increasing the dislocation segment length by one standard deviation. The resulting prediction from this model is presented in Figure 7 and falls within the same range as the present pillar compression data points.

4.2.4. Regimes of deformation

The plastic deformation of iron single crystals shows size dependent features that can be related to the underlying dislocation structure. In large single crystal samples, the initial dislocation structure exists in a variety of configurations. The plastic flow initiates when the stress is high enough to move the first dislocations. The first dislocations can move over relatively large distances before interacting with other dislocations, so-called easy glide. The interactions form barriers for further slip and cause work hardening of the crystal. In small single crystal samples, the included dislocation structure is expected to vary between individual samples [64]. The manufacturing process of the sample can truncate the existing dislocations [12, 13] or possibly form new ones, e.g. from the FIB-induced damage [65]. When the first dislocations start to move, the movement is restricted by the nearby sample surface.

Based on current theories, we summarize the plastic deformation of iron single crystals into three regimes. The regimes are indicated in the upper part of Figure 7 and are similar to those presented by Kraft et al. [5]. The experimental results obtained in this work mainly fall under Regime 2, the intermediate regime, and will be discussed in relation to the data presented in Figure 7 and current theories.

Regime 1 is the *bulk-like regime*, where the stress–strain curves are relatively smooth. In this regime, the samples are typically a few microns or larger. The sample includes larger dislocation segments and parts of dislocation structures [64]. When comparing the flow curves to mm-sized single crystal samples, the flow stress is the highest in the µm-sized samples and the work hardening is about equal [14, 21, 28, 30]. However, the limited volume constrains the dislocation movements and interactions and causes a strengthening effect [5].

The two largest pillars in this study have smooth flow curves, Figure 5, with a work hardening that is within the expected range for stage II work hardening during deformation of iron single crystals [38, 66]. In this stage, dislocations from different slip systems interact and form barriers to slip. The relatively high work hardening is not surprising since the crystal is oriented so that slip can happen along four crossing directions (see Figure 2). If several dislocations are present in the pillar, the first gliding dislocations are likely to interact and form junctions with other dislocations in the pillar resulting to work hardening. From the applied source truncation model, it was estimated that the two largest pillars include two and six dislocation segments, where the largest pillar includes the most dislocations. This indicates that these pillars are likely to include several dislocations which may interact already at the initial dislocation movements.

The thin film experiments by Fukamachi [46] revealed a strengthening effect as the film thickness became less than about 30 μm thick, Figure 7. A similar dimension is found if the size–yield stress data from Brenner's [45] iron whiskers are extrapolated to bulk yield stresses. Based on these experimental observations we speculate that there is a transition where the bulk-like regime transfers into the bulk at about 30 μm. In this larger volume, several dislocations and dislocation sources can exist and operate: the volume is large enough for dislocations to entangle into dislocation networks and dislocation cell structures without being significantly affected by the nearby surface.

Regime 2 is the *intermediate regime* for which the stress–strain curve presents irregular plastic flow with elastic segments and strain bursts, for load controlled experiments. Since the sample is smaller than the average distance between dislocations ($l_\rho = \rho^{-1/2}$, which in this study is ≈ 1 μm), it is likely that few and small dislocation segments are present in the sample. The truncated dislocation segments need a higher stress to operate in a stochastic way. The smaller the segment, or sample, the higher the stress necessary for deformation. Mobile dislocation segments may move to the free surface and annihilate [2, 8, 9], or possibly multiply on the way [10, 11, 18].

Experimental observations show that pre-existing dislocations in pillars from fcc metals tend to move out and annihilate at the pillar surface [2, 8, 9]. On the contrary, pillars from bcc materials appear to have a built in self-multiplication mechanism [10, 11], where dislocations in the pillar multiply on the way towards the surface and form new dislocations rather than removing them from the pillar volume. The self-replication mechanism in bcc pillars has been attributed to the lower mobility of the screw dislocation compared to the faster edge dislocations. The difference in mobility is largest at low temperatures and for metals with a high critical temperature T_c. Since $T_\mathrm{c} = 330$ K is near the test temperature ($T = 298$ K) for iron, the mobility of screw dislocations is similar to that of edge dislocations. As resulted from dislocation dynamics simulations by Lee et al. [37], in such conditions, the few dislocations that exist in the pillar are expected to move out and annihilate at the pillar's surface. The tested iron pillars with $D_\mathrm{t} \lesssim 1$ μm are expected to include very few dislocation segments. Hence, the dislocations are expected to move out and annihilate at the pillars' surfaces.

Regime 3 is the *surface nucleation regime* and has a plastic flow characterized by large elastic segments and abrupt strain bursts, where the stress is typically several GPa. The small volume makes it unlikely that dislocation segments from the initially annihilated dislocation structure exists in the sample. For plasticity to occur, dislocations have to propagate from defects introduced during the focused ion beam fabrication [26, 65, 67].

Three of the smallest pillars, where $D_\mathrm{t} \approx 150$ nm, reaches the highest yield stresses between 2.7–3.1 GPa, Figures 6 and 7. This is only about 45% lower than the values predicted from MD simulation of a pillar with the same loading direction and a diameter of 40 nm [47]. An important difference, however, is that the MD pillar is initially defect free and that the deformation initiates when new dislocations nucleate from the surface of the pillar. The difference in yield stress between the experiments and MD simulation seems to be a consequence of the difference in the initial defect structure and the deformation mechanisms when the plasticity starts. Lowry et al. [67] obtained a similar dissimilarity in results when comparing the yield stress from FIB milled Mo pillars with annealed pillars, which were free of defects.

5. Conclusions

Single crystalline iron micro pillars were compressed along the ⟨001⟩ direction in order to investigate deformation mechanisms and size dependent strength. The analysed slip traces of pillars revealed that the preferred slip plane was of type {110} even if the maximum resolved sheer stress plane corresponded to a {112} plane. The size dependent flow curves show similar characteristic features as previously reported for other bcc metals. The result was compared with existing experimental results on single crystal iron and current theories on small scale plasticity. The current dataset falls in between results from previous investigations of bcc metal pillars.

Acknowledgements

The authors would like to thank Dr. Inga Gudem Ringdalen from SINTEF and Dr. Afrooz Barnoush from NTNU for interesting discussions. We further acknowledge the cooperation with Saarland University in Germany for assistance and help with heat-treatment and electropolishing of samples. One of the authors (B.R.S. Rogne) wishes to thank NTNU for the funding of his Ph.D. work. The Research Council of Norway is acknowledged for the support to the Norwegian Micro- and Nano-Fabrication Facility, NorFab (197411/V30).

References

[1] M.D. Uchic, D.M. Dimiduk, J.N. Florando, and W.D. Nix, Science 305 (2004), p. 986.
[2] J.R. Greer, W.C. Oliver, and W.D. Nix, Acta Mater. 53 (2005), p. 1821.
[3] M.D. Uchic and D.A. Dimiduk, Mater. Sci. Eng. A 400 (2005), p. 268.
[4] M.D. Uchic, P.A. Shade, and D.M. Dimiduk, Ann. Rev. Mater. Res. 39 (2009), p. 361.
[5] O. Kraft, P.A. Gruber, R. Mönig, and D. Weygand, Ann. Rev. Mater. Res. 40 (2010), p. 293.
[6] J.R. Greer and J.T.M. De Hosson, Prog. Mater. Sci. 56 (2011), p. 654.
[7] R. Krahne, G. Morello, A. Figuerola, C. George, S. Deka, and L. Manna, Phys. Rep. 501 (2011), p. 75.
[8] J.R. Greer and W.D. Nix, Phys. Rev. B 73 (2006), p. 245410.
[9] D. Kiener and A.M. Minor, Nano Lett. 11 (2011), p. 3816.
[10] J.R. Greer, C.R. Weinberger, and W. Cai, Mater. Sci. Eng. A 493 (2008), p. 21.
[11] C.R. Weinberger and W. Cai, Proc. Natl. Acad. Sci. U. S. A. 105 (2008), p. 14304.
[12] T.A. Parthasarathy, S.I. Rao, D.M. Dimiduk, M.D. Uchic, and D.R. Trinkle, Scr. Mater. 56 (2007), p. 313.
[13] S.I. Rao, D.M. Dimiduk, M. Tang, T.A. Parthasarathy, M.D. Uchic, and C. Woodward, Philos. Mag. 87 (2007), p. 4777.
[14] D.M. Dimiduk, M.D. Uchic, and T.A. Parthasarathy, Acta Mater. 53 (2005), p. 4065.
[15] C.A. Volkert and E.T. Lilleodden, Phil. Mag. 86 (2006), p. 5567.
[16] Z.W. Shan, R.K. Mishra, S.A.S. Asif, O.L. Warren, and A.M. Minor, Nat. Mater. 7 (2008), p. 115.
[17] C.P. Frick, B.G. Clark, S. Orso, A.S. Schneider, and E. Arzt, Mater. Sci. Eng. A 489 (2008), p. 319.
[18] S. Brinckmann, J.Y. Kim, and J.R. Greer, Phys. Rev. Lett. 100 (2008), p. 155502.
[19] D. Kiener and A.M. Minor, Acta Mater. 59 (2011), p. 1328.
[20] D. Kiener, Z. Zhang, S. Sturm, S. Cazottes, P.J. Imrich, C. Kirchlechner, and G. Dehm, Philos. Mag. 92 (2012), p. 3269.
[21] A.S. Schneider, D. Kiener, C.M. Yakacki, H.J. Maier, P.A. Gruber, N. Tamura, M. Kunz, A.M. Minor, and C.P. Frick, Mater. Sci. Eng. A 559 (2013), p. 147.

[22] J.Y. Kim and J.R. Greer, Appl. Phys. Lett. 93 (2008), p. 101916.
[23] J.Y. Kim, D. Jang, and J.R. Greer, Scr. Mater. 61 (2009), p. 300.
[24] A.S. Schneider, B.G. Clark, C.P. Frick, P.A. Gruber, and E. Arzt, Mater. Sci. Eng. A 508 (2009), p. 241.
[25] A.S. Schneider, D. Kaufmann, B.G. Clark, C.P. Frick, P.A. Gruber, R. Mönig, O. Kraft, and E. Arzt, Phys. Rev. Lett. 103 (2009), p. 105501.
[26] S. Shim, H. Bei, M.K. Miller, G.M. Pharr, and E.P. George, Acta Mater. 57 (2009), p. 503.
[27] J.Y. Kim and J.R. Greer, Acta Mater. 57 (2009), p. 5245.
[28] A.S. Schneider, B.G. Clark, C.P. Frick, P.A. Gruber, and E. Arzt, Philos. Mag. Lett. 90 (2010), p. 841.
[29] J.Y. Kim, D. Jang, and J.R. Greer, Acta Mater. 58 (2010), p. 2355.
[30] A.S. Schneider, C.P. Frick, B.G. Clark, P.A. Gruber, and E. Arzt, Mater. Sci. Eng. A 528 (2011), p. 1540.
[31] S.M. Han, T. Bozorg-Grayeli, J.R. Groyes, and W.D. Nix, Scr. Mater. 63 (2010), p. 1153.
[32] D. Kaufmann, R. Mönig, C.A. Volkert, and O. Kraft, Int. J. Plast. 27 (2011), p. 470.
[33] L. Huang, Q.J. Li, Z.W. Shan, J. Li, J. Sun, and E. Ma, Nat. Commun. 2 (2011).
[34] J.Y. Kim, D. Jang, and J.R. Greer, Int. J. Plast. 28 (2012), p. 46.
[35] J.L. Stewart, L. Jiang, J.J. Williams, and N. Chawla, Mater. Sci. Eng. A 534 (2012), p. 220.
[36] S.M. Han, G. Feng, J.Y. Jung, H.J. Jung, J.R. Groves, W.D. Nix, and Y. Cui, Appl. Phys. Lett. 102 (2013), p. 041910.
[37] S.W. Lee, Y. Cheng, I. Ryu, and J.R. Greer, Sci. China Tech. Sci. 57 (2014), p. 652.
[38] T.L. Altshuler and J.W. Christian, Phil. Trans. R. Soc. Lond. A 261 (1967), p. 253.
[39] D.F. Stein and J.R. Low Jr, Acta Metall. 14 (1966), p. 1183.
[40] W. Spitzig and A. Keh, Metall. Mater. Trans. B 1 (1970), p. 2751.
[41] D. Ali, N. Mushtaq, and M. Butt, J. Mater. Sci. 46 (2011), p. 3812.
[42] T. Yalcinkaya, W.A.M. Brekelmans, and M.G.D. Geers, Modell. Simul. Mater. Sci. Eng. 16 (2008), p. 085007.
[43] D. Brunner and J. Diehl, Phys. Status Solidi A 124 (1991), p. 455.
[44] D. Caillard, Acta Mater. 58 (2010), p. 3493.
[45] S.S. Brenner, J. Appl. Phys. 27 (1956), p. 1484.
[46] M. Fukamachi, Jpn. J. Appl. Phys. 11 (1972), p. 1259.
[47] C.H. Ersland and C. Thaulow, *Modeling of size and strain rate effects in compression tests of iron nanopillars*, in *Atomistic modeling of failure in iron*, C.H. Ersland, ed., Ph.d. diss. Norwegian University of Science and Technology, 2012 (2012), pp. 1–11.
[48] M. Friák, M. Šob, and V. Vitek, Philos. Mag. 83 (2003), p. 3529.
[49] N. Kheradmand and H. Vehoff, Adv. Eng. Mater. 14 (2012), p. 153.
[50] K.S. Ng and A.H.W. Ngan, Philos. Mag. 88 (2008), p. 677.
[51] A.S. Schneider, C.P. Frick, E. Arzt, W.J. Clegg, and S. Korte, Philos. Mag. Lett. 93 (2013), p. 331.
[52] M. Feller-Kniepmeier and M. Hundt, Scr. Metall. 17 (1983), p. 905.
[53] H. Matsui, S. Moriya, S. Takaki, and H. Kimura, Trans. Jpn. Inst. Met. 19 (1978), p. 163.
[54] G.A. Malygin, Phys. Solid State 54 (2012), p. 1220.
[55] Q. Guo and J.R. Greer, Scr. Mater. 66 (2012), p. 272.
[56] P. Landau, Q. Guo, P. Hosemann, Y. Wang, and J.R. Greer, Mater. Sci. Eng. A 612 (2014), p. 316.
[57] D. Kaufmann, A.S. Schneider, R. Mönig, C.A. Volkert, and O. Kraft, Int. J. Plast. 49 (2013), p. 145.
[58] D. Hull and D.J. Bacon, *Introduction to Dislocations*, 4th ed., Butterworth-Heinemann, Oxford, 2001.
[59] G.I. Taylor and C.F. Elam, Proc. R. Soc. Lond. A 112 (1926), p. 337.
[60] D.F. Stein, J.R. Low Jr, and A.U. Seybolt, Acta Metall. 11 (1963), p. 1253.
[61] B.W. Christ and G.V. Smith, Metall. Trans. 1 (1970), p. 827.
[62] P. Sudharshan Phani, K.E. Johanns, G. Duscher, A. Gali, E.P. George, and G.M. Pharr, Acta Mater. 59 (2011), p. 2172.
[63] H. Bei, S. Shim, G.M. Pharr, and E.P. George, Acta Mater. 56 (2008), p. 4770.
[64] D.M. Norfleet, D.M. Dimiduk, S.J. Polasik, M.D. Uchic, and M.J. Mills, Acta Mater. 56 (2008), p. 2988.
[65] D. Kiener, C. Motz, M. Rester, M. Jenko, and G. Dehm, Mater. Sci. Eng. A 459 (2007), p. 262.
[66] A.S. Keh, Philos. Mag. 12 (1965), p. 9.
[67] M.B. Lowry, D. Kiener, M.M. LeBlanc, C. Chisholm, J.N. Florando, J.W. Morris Jr, and A.M. Minor, Acta Mater. 58 (2010), p. 5160.

Paper III

B. R. S. Rogne and C. Thaulow.

Effect of Crystal Orientation on the Strengthening of Iron Micro Pillars.

Manuscript submitted to: *Materials Science and Engineering A.*
DOI: 10.1016/j.msea.2014.10.067

Effect of Crystal Orientation on the Strengthening of Iron Micro Pillars

Bjørn Rune Sørås Rogne[a,*], Christian Thaulow[a]

[a] *Department of Engineering Design and Materials, Norwegian University of Science and Technology, No-7491 Trondheim, Norway*

Abstract

Micro pillar compression testing has been performed on bcc iron single crystals to determine the mechanical properties and deformation mechanisms and their dependency on size and crystal orientation. Slip traces on the surface of post-compressed pillars were scrutinised to determine the operating slip system. The size dependency of the flow curves was investigated and the power law constants, K and n, and the orientation dependency of the resolved shear stresses were determined.

The slip trace analysis revealed that the slip follows the $\{110\}\langle 111\rangle$ family of slip systems. The size dependency of the flow stresses follows the power law relation where the power law exponent n are in general between 0.5–0.8 and depend on orientation and the strain. The power law coefficient K increases as a function of strain. The shape is similar for the different loading directions, but varies in magnitude. The shear stress resolved to the $(\bar{1}01)[111]$ slip system shows an orientation dependent relation. Size and strain has little effect on this relation.

Keywords: pillar compression testing, deformation mechanisms, micromechanics, size effect, orientation dependency, bcc iron

---

1. Introduction

In the past, mechanical testing of single crystal metals were performed on large crystals [1–3]. The preparation and characterization of single crystals are often difficult and time-consuming, especially when it comes to growing large iron crystals [4]. New experimental techniques, such as pillar compression testing [5–11], have allowed detailed examinations of the deformation mechanisms. With this technique, nano- and micro pillars are machined from specific locations of the sample to study the resistance to plastic flow and gain insight into the underlying dislocation mechanisms. In this paper we investigate the effect of size and crystallographic orientation of pillars made from iron crystals.

Mechanical testing of metals at micro- and nano scale has revealed that the strength increases as the size of the test specimen is reduced. The relationship is expressed according to a power law

$$\sigma = K D_{\mathrm{t}}^{-n} \tag{1}$$

where σ is the flow stress, D_{t} is the top-surface diameter of a cylindrical sample, K is the power law coefficient and n is the power law exponent. Today it is generally agreed that the size strengthening is caused by a change in dislocation mechanisms. The existing dislocation sources become truncated because of the limited volume [12]. The increased ratio between surface area and volume in the small pillars can also cause dislocations to move out to the surface and leave the sample in a dislocation starved condition [13, 14]. Results on metal single crystal micro pillars have been published for a wide range of fcc [7, 15–23] and bcc [18, 20, 24–38] metals. However, a thorough investigation of the orientation dependency of the size effect of bcc iron has not yet been published.

In a recent paper [39] we examined the size effect of iron pillars with [001] crystallographic orientation. The underlying deformation mechanisms in the specific size regimes can be summarized from Fig. 1:

1. *The bulk-like regime* reveals smooth stress–strain curves. In this region larger dislocation segments and parts of dislocation substructures will exist in the pillar, but the limited volume will constrain the dislocation movements and interactions, and cause a strengthening effect [9].
2. *The intermediate regime* presents stress–strain curves with irregular plastic flow, where portions of the curve consists of elastic loadings and strain

---

[*] Corresponding author. Tel.: +47 73593917; fax: +47 73594129.
Email address: `bjorn.rogne@ntnu.no` (Bjørn Rune Sørås Rogne)

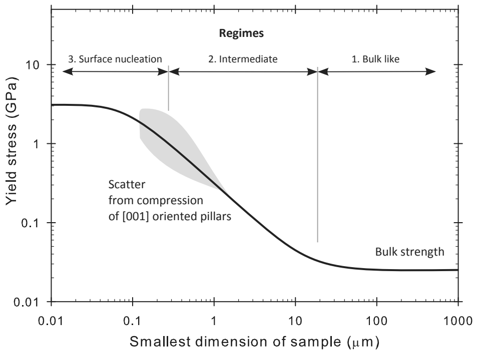

Figure 1: Yield stress as a function of the smallest dimension of the iron sample. Three size regimes and the scatter from [001] oriented pillars from [39] are indicated in the figure.

   bursts, for load controlled experiments. Since the pillar diameter is less than the average distance between dislocations, it is likely that small dislocation segments exist in the pillars. The truncated dislocation segments need a higher stress to operate in a stochastic way. The smallest segments, or pillars, need the highest stresses to deform. Mobile dislocation segments may move to the free surface and annihilate, possibly multiplying on the way [13, 14, 40].

3. *The surface nucleation regime* has a stress–strain curve characterized by large elastic segments and abrupt strain bursts, where the stress is typically several GPa. The small volume makes it unlikely that dislocation segments from the initially annihilated dislocation structure is included in the pillar. For plasticity to occur dislocations are nucleated from small notches or defects at the surface introduced during the focused ion beam (FIB) fabrication.

The observed macroscopic slip traces during tension testing of iron single crystals depends strongly on the purity of the crystal, temperature, strain rate, sample size and loading direction [1–3, 41]. In the detailed study by Aono et al. [41] the samples were heavily deformed at 200 K and no slip lines could be determined. At lower temperatures (77 K) the slip lines are usually parallel and depends on loading direction. The resent transmission electron microscopy (TEM) study by Caillard [42] looks at the dislocation motion when straining along the $[1\bar{4}3]$ axis of a thin iron film at room temperature. The deformation was concluded to happen with a Burgers vector (**b**) of $\mathbf{b} = 1/2[\bar{1}\bar{1}1]$ where the dislocations glide on $(\bar{1}10)$ plane.

In the present paper we extend the investigations to include 4 crystal orientations, loaded along the $[\bar{1}49]$, $[\bar{2}35]$, [011] and $[\bar{1}11]$ directions. The orientations were selected in such a way that the samples were expected to deform either in single slip, with orientation of $[\bar{1}49]$ and $[\bar{2}35]$, or in multiple slip, with orientation of [001], [011] and $[\bar{1}11]$, along one or both the slip systems of type $\{110\}\langle111\rangle$ and $\{112\}\langle111\rangle$. The pillar diameters ranged from hundreds of nanometers to a few microns. Our aim was to reveal the underlying deformation mechanisms' dependency on orientation and pillar size.

2. Materials and experimental procedures

2.1. Materials

The material used was a 99.99 % pure iron plate. The 1 mm thick cold rolled plate was cut into 8×8 mm^2 square pieces with a fine cut-off grinding wheel before being ground with SiC paper, and polished with diamond particles and colloidal silica suspension. The samples were then heat treated in a high vacuum furnace at 923 K (650 °C) for 5 h in order to produce enlarged grains. Final surface preparation was performed by electropolishing to remove the surface deformations. The average grain size after the heat treatment was measured to 29 ± 16 μm. Selected regions from two samples (A and B) where studied with a field emission scanning electron microscope (FE-SEM) and electron backscatter diffraction (EBSD). The indexed crystallographic orientations of the grains were evaluated in order to pick grains that had a detected plane normal, direction normal to the sample surface, within 2° from the desired family of directions. In total 10 grains that consisted of the 4 orientations $[\bar{1}49]$, $[\bar{2}35]$, [011] and $[\bar{1}11]$ were selected and used for further production and testing. An overview is given in Table 1. Results for [001] oriented pillars from [39] are in several instances included for comparison and the original data have been further analysed in this paper. All orientations are visualized in the [001]–[011]–$[\bar{1}11]$ triangle in the [001] stereographic projection of cubic crystals in Fig. 2. χ in the figure representents the angle between the maximum resolved shear stress plane (MRSSP), the plane which encounters the highest shear stresses along [111] direction, and the $(\bar{1}01)$ plane [43, 44]. χ is defined as positive when MRSSP lies between $(\bar{1}01)$ and $(\bar{1}10)$, and negative if it lies between $(\bar{1}01)$ and $(0\bar{1}1)$.

Table 1: Overview of tested pillars. Values from loading direction [001] were obtained from [39] for comparison.

Orientation	χ (°)	Sample	Number of tested grains	Number of tested pillars	Diameter range (nm)
$[\bar{1}49]$	0	A	2	34	120–2100
$[\bar{2}35]$	14	A and B	3	29	120–2100
[001]	-30	A	4	40	140–4300
[011]	30	B	2	13	470–2000
$[\bar{1}11]$	30	A and B	3	17	130–2000

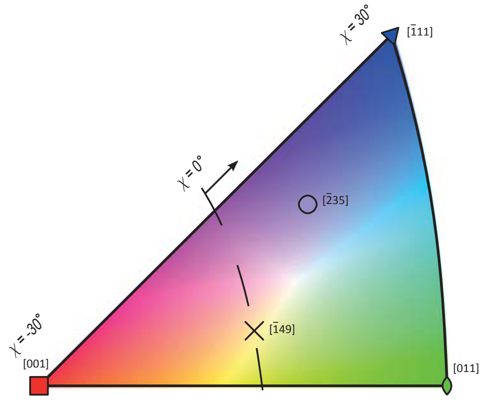

Figure 2: The [001]–[011]–$[\bar{1}11]$ triangle in the [001] stereographic projection of cubic crystals. The selected orientations are indicated in the triangle.

2.2. *Pillar production*

Nano- and micro pillar specimens were milled and imaged using a FIB/SEM DualBeam™ system (FEI Helios NanoLab™). The pillars were manufactured in two steps with an acceleration voltage of 30 kV. The first step use a bitmap milling pattern to mill out an array of iron stumps at a high milling current (between 3 and 9 nA) inside grains. Some of the stumps were produced from circular milling patterns. The second step use a circular milling pattern at a lower current (93 to 920 pA) to refine the final shape, see Fig. 3. The second step is essential to minimize the sputtering rate and the energy spread of the beam. Consequently, this reduces the material redeposition and the size of the ion beam so that a well-defined pillar shape with a small taper angle (α) can be produced. The aspect ratio (H/D_t), defined as the ratio between the pillar height (H) and diameter at the top (D_t) of the pillar were kept between 2 and 4, except for some few cases of the largest specimens that had a slightly lower aspect ratio. α varied from 1 to 5° and increased with decreasing pillar size.

2.3. *Nanomechanical testing*

After manufacturing, the sample was transferred to a Hysitron TI 750 Ubi™ nanoindentation system with a Performech® controller unit. The pillars were loaded with a flat-punch diamond indenter from Synton-MDP in the open-loop load control mode. The flat punch tip have a 5 µm large diameter and a 60° cone angle. Before loading, the tip was positioned over the pillar from the optical position of the instrument and further adjusted by using the tip scan mode to identify the accurate position of the pillar [45]. The well-defined array of pillars made it possible to load a fraction of the samples without using the tip scanning prior compression. The logged force (F) and displacement (Δ) output was converted to engineering stress (σ) and engineering strain (ε) by using the pillar height H and the diameter D_t in the calculations. The load functions consisted of a constant loading rate ($\dot{F}$) up to a maximum load followed by a rapid unloading. The applied $\dot{F}$ varied from 6 to 160 μN s^{-1} and was chosen so that the stress rate ($\dot{\sigma}$), $\dot{\sigma} = \dot{F}/A$, where $A = (\pi/4)D_t{}^2$, was close to 200 MPa s^{-1}. The corresponding strain rate ($\dot{\varepsilon}$) was about 1×10^{-3} s^{-1}, assuming that $\dot{\varepsilon} = E/\dot{\sigma}$, with a Young's modulus (E) of 200 GPa.

3. Results

3.1. *Crystallographic slip*

A selection of compressed pillars were investigated to determine whether the favoured slip system was of type $\{110\}\langle111\rangle$ or $\{112\}\langle111\rangle$. The pillars had a diameter of about 1 µm and were only deformed to a few percent of strain, Fig. 4. Slip traces, or slip bands, at the pillar surface where compared with slip trace locations calculated from EBSD scan and identified, see [39] for details. Within the [001]–[011]–$[\bar{1}11]$ triangle (excluding the edges of the triangle), Fig. 2, the

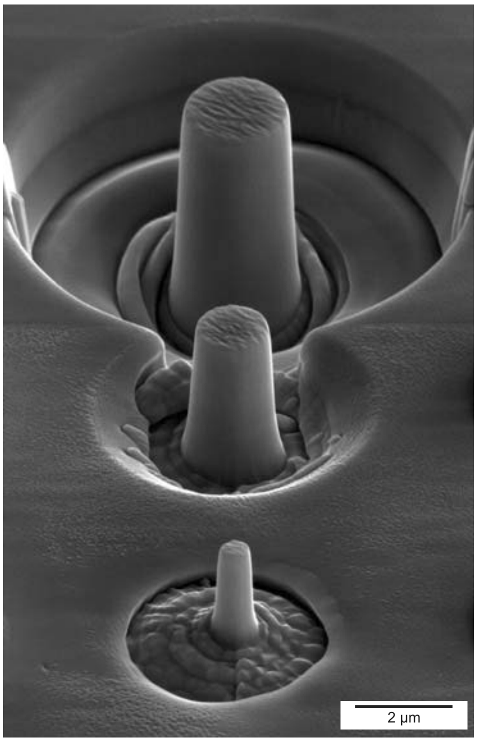

Figure 3: SEM micrograph of $[\bar{1}49]$ oriented pillar samples after the second low current milling step, before compression testing.

preferred direction of slip is the [111] direction. Due to crystal symmetry several equivalent slip directions encounter the same stress conditions at the edges. If we only consider the slip planes along the [111] direction there are three slip planes that encounter the highest resolved shear stresses. These are the planes $(\bar{1}01)$, $(\bar{2}11)$ and $(\bar{1}\bar{1}2)$. In the centre of the triangle ($\chi \approx 0°$) the $(\bar{1}01)[111]$ system becomes the highest stressed one. In orientations towards the $[011]$–$[\bar{1}11]$ line ($\chi \lesssim 30°$) the $(\bar{2}11)[111]$ becomes the highest stressed one, and near [001] ($\chi \gtrsim -30°$) it changes to $(\bar{1}\bar{1}2)[111]$. An overview of the Schmid factor (S) of the different orientations and slip systems is given in Table 2.

In orientation $[\bar{1}49]$ the $(\bar{1}01)[111]$ slip system is the most highly stressed. Along the preferred [111] direction, the primary slip direction, the $(\bar{1}01)$ slip plane, with a Schmid factor of $S^{[\bar{1}49]}_{(\bar{1}01)[111]} = 0.50$, is followed by the $(\bar{2}11)$ and $(\bar{1}\bar{1}2)$ planes which have slightly lower shear stresses, $S^{[\bar{1}49]}_{(\bar{2}11)[111]} = S^{[\bar{1}49]}_{(\bar{1}\bar{1}2)[111]} = 0.43$. In pillars with this orientation we identified slip along the $(\bar{1}01)[111]$ system as well as along the secondary $[\bar{1}11]$ direction. In the latter case the slip system was identified to $(101)[\bar{1}11]$. Further in the text we will refer to the $(\bar{1}01)[111]$ as the primary slip system and to the $(101)[\bar{1}11]$ as the secondary. In Fig. 4(a) the slip was activated along the secondary slip direction, however the primary slip system was observed more frequently.

Orientation $[\bar{2}35]$ have both the $(\bar{1}01)[111]$ and $(\bar{2}11)[111]$ system with the same high $S^{[\bar{2}35]}_{(\bar{1}01)[111]} = S^{[\bar{2}35]}_{(\bar{2}11)[111]} = 0.45$. If one of the two slip systems is preferred it should be easy to identify it. From the slip traces on the pillar surface, see Fig. 4(b), it is evident that the $(\bar{1}01)$ slip plane carries out the majority of the deformation.

Orientation [001] has four symmetric $\langle 111 \rangle$ glide directions and for each direction there are two equivalent $\{110\}$ planes and one $\{112\}$ plane where the latter one has the highest Schmid factor. The dominating slip system, according to [39] and Fig. 4(c), is the $\{110\}\langle 111 \rangle$ system and the slip happens on two non-parallel slip planes of type $\{110\}$ along each slip directions. The difference in Schmid factor indicates that a higher stress is needed to activate slip along the $(2\bar{1}\bar{1})$ plane than $(\bar{1}01)$ plane under the current experimental conditions.

Orientation [011], Fig. 4(d), deforms similar to orientation [001], but only along two slip directions with two non-parallel $\{110\}$ planes.

Orientation $[\bar{1}11]$, Fig. 4(e), deforms along three symmetrical $\langle 111 \rangle$ directions and the slip traces on the surface are typically fairly evenly distributed and diffi-

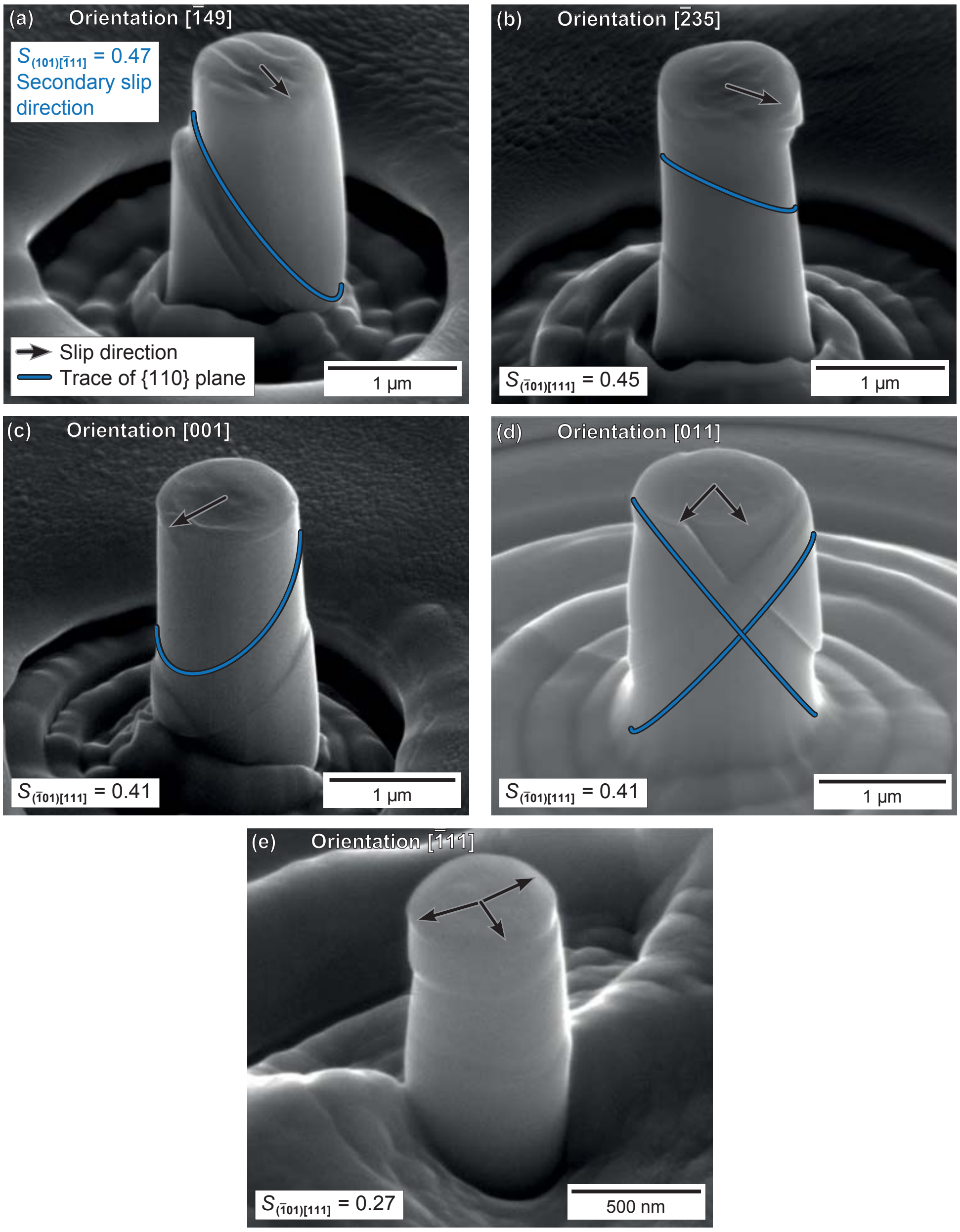

Figure 4: Post compression SEM micrographs of pillars with diameters close to 1 µm. The deformation was limited to a few percent strain. The identified active slip planes are illustrated by lines in the figure. The pillars are loaded along the (a) $[\bar{1}49]$, (b) $[\bar{2}35]$, (c) [001], (d) [011] and (e) $[\bar{1}11]$ axis. Slip planes, slip directions and the corresponding Schmid factor (S) are indicated in the figures and summarized in Table 2.

Table 2: Slip systems observed after compression of pillars, see Fig. 4. Values for loading direction [001] were obtained from [39] for comparison.

Orientation	Number of equivalent slip directions	Schmid factor (S)			Observed slip system
		$S_{(\bar{1}01)[111]}$	$S_{(\bar{2}11)[111]}$	$S_{(\bar{1}\bar{1}2)[111]}$	
$[\bar{1}49]$	1	0.50	0.43	0.43	$(\bar{1}01)[111]$ and $(101)[\bar{1}11]$ [a]
$[\bar{2}35]$	1	0.45	0.45	0.33	$(\bar{1}01)[111]$
[001]	4	0.41	0.24	0.47	$(\bar{1}01)[111]$
[011]	2	0.41	0.47	0.24	$(\bar{1}01)[111]$
$[\bar{1}11]$	3	0.27	0.31	0.16	

[a] Along the $[\bar{1}11]$ direction $S^{[\bar{1}49]}_{(101)[\bar{1}11]} = 0.47$, $S^{[\bar{1}49]}_{(211)[\bar{1}11]} = 0.37$ and $S^{[\bar{1}49]}_{(1\bar{1}2)[\bar{1}11]} = 0.44$.

cult to interpret. From the chaotic slip traces, and the observations from the other orientations, we speculates that the slip occurs along two non-parallel {110} planes for each direction. If the slip had happened solely along the fewer {112} planes it should have been possible to identify their slip traces.

For all multiple slip orientations it is frequently seen that one of the slip directions governs the plastic deformation. For all orientations it appears that other slip planes, with lower S, are activated after some initial plasticity. This is presumably a consequence of geometrical changes during plasticity.

3.2. Flow curves

Stress–strain curves from the 4 orientations are shown in Fig. 5. The largest pillars show smooth σ–ε curves and the smaller pillars deform in a stochastic manner with strain bursts separated by linear elastic segments.

The σ–ε curves for the smallest pillars differ for the different orientations. In the single slip orientations, $[\bar{1}49]$ and $[\bar{2}35]$, the stain bursts are larger and start at smaller strains than those in the multiple slip orientations, [001], [011] and $[\bar{1}11]$.

3.3. The power law relation

The appearance of several strain bursts makes it challenging to compare the σ–ε curves directly. In order to analyse the flow stresses as function of the pillar diameter we plotted the flow stress at $\varepsilon = 2.5\%$ ($\sigma_{2.5\%}$) and the flow stress at $\varepsilon = 5\%$ ($\sigma_{2.5\%}$) as a function of D_t in the double logarithmic plots in Fig. 6. The datapoints in Fig. 6 were further analysed by fitting them to the power law relation in Eq. (1). The power law exponent n, that quantifies the strengthening, together with the power law coefficient K are summarized in Table 3. The subscript indicates if the constants were calculated from flow stresses at $\varepsilon = 2.5\%$ and $\varepsilon = 5\%$. n varies between 0.51–0.80 and $n_{2.5\%} < n_{5\%}$ for the same orientation.

The coefficient K has unit MPa μm^n, Table 3, hence, it essentially represents the average flow stress of the pillars with 1 µm in diameter. $K_{2.5\%} < K_{5\%}$ indicates that the pillars of this size strain hardens slightly between 2.5% and 5% strain. In order to incorporate the effect of loading directions we use Schmid's law

$$\tau = S\sigma \tag{2}$$

to calculate the resolved shear stress (τ). S is here the Schmid factor and σ is the applied compressive stresses. Alternatively, by combining Eqs. (1) and (2) yields

$$\tau = SKD_\text{t}^{-n} \tag{3}$$

, we can than directly estimate τ from S, K, D_t and n.

The resolved shear stress τ was calculated for $D_\text{t} =$ 1 µm at $\varepsilon = 2.5\%$ ($\tau_{2.5\%}$) and $\varepsilon = 5\%$ ($\tau_{5\%}$), Table 3, by applying Eq. (3). In the calculations we use the Schmid factor S that corresponded to the observed $(\bar{1}01)[111]$ slip system, $S_{(\bar{1}01)[111]}$, see Section 3.1. The magnitude of τ are ordered as [001], $[\bar{1}49]$, $[\bar{2}35]$, $[\bar{1}11]$ and [011], where orientation [001] obtains the highest values. The order corresponds to moving from left to right in the standard [001] stereographic projection in Fig. 2, where orientation $[\bar{1}11]$ get slightly higher τ than [011].

4. Discussion

4.1. Slip traces

In the previous paper [39] we reported that the slip traces on the pillar surface corresponded to the $\{110\}\langle111\rangle$ slip system for the [001] oriented pillars. In the current work similar deformation behaviour was observed. In loading directions $[\bar{1}49]$, $[\bar{2}35]$ and [011] the slip traces on the surface of the pillars were identified to follow the $\{110\}\langle111\rangle$ slip system. The slip traces

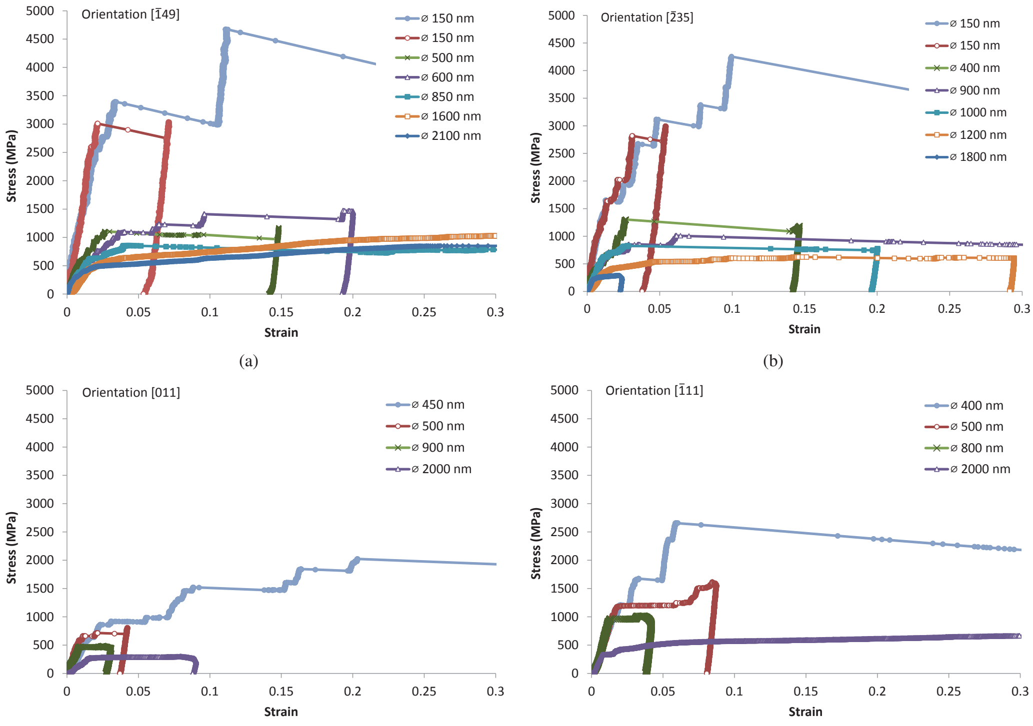

(a) (b)

(c) (d)

Figure 5: Stress–strain curves of pillars loaded along the (a) [$\bar{1}$49], (b) [$\bar{2}$35], (c) [011] and (d) [$\bar{1}$11] axis. The diameter of each pillar is indicated in the legends.

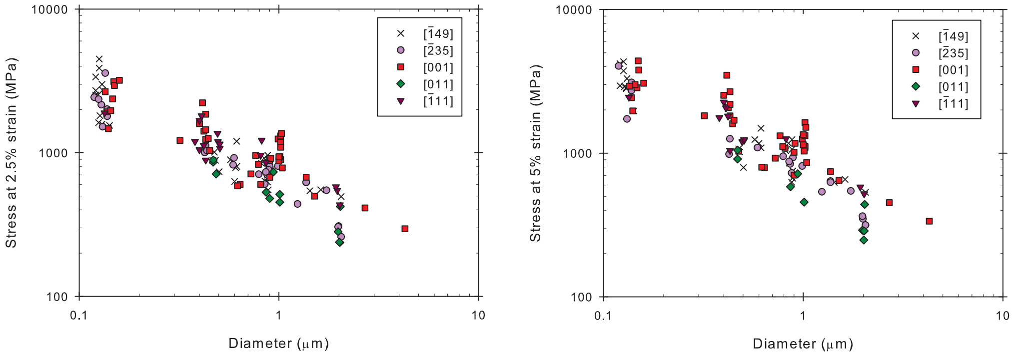

(a) (b)

Figure 6: Plot of (a) the stress at 2.5% strain ($\sigma_{2.5\%}$) and (b) the stress at 5% strain ($\sigma_{5\%}$) as a function of pillar diameter (D_t) for the five orientations.

Table 3: Overview of the power law exponent n, power law coefficient K (MPa µm^n) and the resolved shear stress τ (MPa) calculated at 2.5% and 5% strain. τ are calculated for $D_t = 1$ µm and values from orientation [001] were obtained from [39] for comparison.

Loading direction	$n_{2.5\%}$	$n_{5\%}$	$K_{2.5\%}$ (MPa µm^n)	$K_{5\%}$ (MPa µm^n)	$\tau_{2.5\%}$ (MPa)	$\tau_{5\%}$ (MPa)
[$\bar{1}$49]	0.63	0.65	659	804	329	402
[$\bar{2}$35]	0.64	0.70	613	695	276	313
[001]	0.55	0.60	808	1023	331	419
[011]	0.73	0.80	490	541	201	222
[$\bar{1}$11]	0.51	0.60	803	907	217	245

on [$\bar{1}$11] oriented pillars were not identified because of less distinct traces on the sample surface. In pillars with orientation [$\bar{1}$49] the primary or secondary slip system were observed as the only operating slip system early in the deformation.

4.1.1. *Activation of the secondary slip system in orientation* [$\bar{1}$49]

The evidence of the secondary (101)[$\bar{1}$11] slip system instead of the primary ($\bar{1}$01)[111] slip system in orientation [$\bar{1}$49] can be explained as follows. Small misalignments between the indenter tip surface and the pillar top-surface or a roughness at the pillar top-surface can causes a stress distribution that is beneficial for the secondary slip system. In the current experiments there is a small ripple-like roughness on the top-surface after the sample preparation, Fig. 3. For the largest pillars this roughness is small compared to the pillar diameter and the local stress concentrations can easily be redistributed early under the top-surface. For small pillars the roughness becomes large compared to the diameter and the local stress concentrations can become high enough to trigger deformation on a secondary slip system. The distance between the ripples on the surface is about 200 nm.

Alternatively a favourable dislocation segment, that needs a lower stress to move, can be located on the slightly less stressed plane when it starts to glide. If it is so, one should expect a size dependent factor in the selection of slip plane. Large pillars will include several dislocations on each available plane and consequently the highest stressed plane will determine where the deformation starts. As the size of the pillar is reduced it will become less likely to find a favourable dislocation segment on the highest stressed plane. Hence, a secondary plane with a more favourable oriented dislocation segment might initiate the plastic deformation. This transition from a stress controlled regime to a regime controlled by the available dislocation segments should be possible to determine from the experiments. The source truncation model by Parthasarathy et al. [12] uses the dislocation density (ρ) prior FIB milling to predict the number of dislocation segments that is left in the pillar after the truncation by the FIB milling. The predicted number of dislocation segments, or dislocation pinning points, inside the pillar becomes scarcely as the pillar size approaches the average distance between dislocations ($l_\rho = 1/\sqrt{\rho}$). If we assume that $\rho = 1 \times 10^{12}$ m^{-2} we should expect the transition to happen when the pillar diameter approaches $l_\rho = 1$ µm. For very small pillars it becomes less likely to find dislocation segments from the original dislocation structure and the deformation have to initiate from the available FIB damage near the surface.

In order to examine if the secondary slip system had a size dependent factor we extended the post-compression analysis from the 1 µm pillars to also include pillars ranging from 120 nm to 2.1 µm in diameter, Fig. 7. The deformation in the three largest pillars, with $D_t > 1$µm, are governed by slip along the primary slip system. When the diameter decreases below 1 µm we observe that the secondary slip system dominates the deformation in some samples, Fig. 7(b). The secondary slip system is most frequently seen at diameters of about 800 nm. Figs. 7(d) to (f) shows examples among the smallest pillars where the primary, the secondary and both of the slip systems are activated, respectively. The primary slip system dominated in about 65 % and the secondary slip system in about 10 % of the investigated pillars. The remaining pillars had a mix of the primary and secondary slip system. With the rather small dataset that was analysed we can only speculate that a size-dependent transition exists.

4.2. *Orientation and strain dependent power law relation*

From the calculated power law exponent n and coefficient K in Table 3 we observe that $n_{2.5\%} < n_{5\%}$ and $K_{2.5\%} < K_{5\%}$ for all of the orientations. The increase of n and K indicates a systematic change as the strain

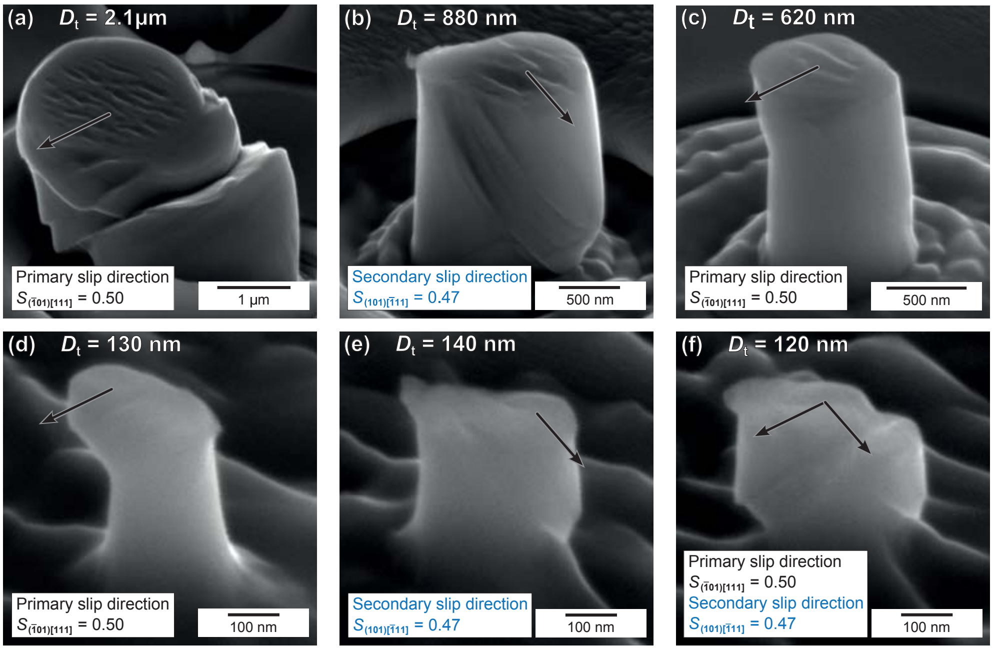

Figure 7: Post compression SEM micrographs of pillars loaded along the [$\bar{1}49$] axis. The pillar diameters are 2.1 µm in (a), 880 nm in (b), 620 nm in (c) and about 130 nm in (d) to (f). The primary slip system is activated in (a), (c) and (d), and the secondary slip system is activated in (b) and (e), while both the primary and secondary slip system are activated in (f).

increase. To further clarify the evolution of n, K and τ we calculated them as a function of strain. The ressults are plotted in Fig. 8 where subfigures (a), (c) and (e) corresponds to n, K and τ, respectively, and subfigures (b), (d) and (f) shows detailed curves between 2% and 5% strain. At least 8 datapoints were used in each curve fitting to achieve reliable values.

The power law exponent n in Figs. 8(a) and (b) increases rapidly at small strains, $\varepsilon < 0.02$, and becomes almost constant early in the plastic flow, $\varepsilon = 0.03$–0.05, before it starts to decrease again. The reduction of n is presumably happening when large strain bursts, with corresponding load drops, appear in the stress–strain curves of the smallest pillars. The large strain bursts, see Fig. 5, happens earlier and are longer for the single slip orientations, $[\bar{1}49]$ and $[\bar{2}35]$. Consequently the reduction of n can be expected to start at smaller strains and decline more for the single slip orientations compared to the multiple slip orientations. In general the exponents are in the upper range of the earlier reported values for bcc metals (n typically in the range 0.2 to 0.5) and in the lower range for fcc metals (0.6 to 1.0).

The power law coefficient K, Figs. 8(c) and (d), shows a behaviour similar to that of the σ–ε curves. Since the units are in MPa $\mu\mathrm{m}^n$ they essentially represent the average flow stress of the pillars with an 1 μm in diameter. The K–ε curves are relatively similar in shape but K varies in magnitude between the orientations. A striking difference appear for the $[\bar{1}49]$ orientation, where K increases rapidly as $\varepsilon > 0.25$.

Figs. 8(e) and (f) shows τ as a function of strain. τ is calculated from Eq. (3) by using $S_{(\bar{1}01)[111]}$, $D_{\rm t} = 1$ μm and the fitted parameter K. Resolving K to the $(\bar{1}01)[111]$ slip system allows us to investigate the component acting on the slip plane and direction. Since the single slip orientations typically only deform along one slip system and the multiple slip orientations activates several equivalent slip systems, one should expect a different evolution of τ (and σ) as the strain increases. However, no distinct difference can be observed.

Some general features can be seen in the orientation dependency of τ, and how it is affected by pillar size and strain. It is challenging to determine the relative difference of σ (or τ) for pillars of different diameters from the scattered data in Fig. 6. To quantify this we estimated the τ for different pillar diameters in two ways. The first approach uses the data points directly from Fig. 6(a). Groups of similar sized pillars were averaged into average stresses ($\sigma^{\rm avg}_{2.5\%}$) and average pillar diameters ($D_{\rm t}^{\rm avg}$). $\tau_{2.5\%}$ was calculated by Eq. (2) and presented in Fig. 9(a)(open symbols). The second approach uses $\sigma^{\rm avg}_{2.5\%}$, from the first approach, and fitted values of K and n as input to Eq. (3). The results from these calculations are presented in Fig. 9(a) in relation to χ. In the same fashion, τ was calculated for different strains by Eq. (3) for $D_{\rm t} = 1$ μm and from curve fitted values from Fig. 8. The results are plotted in Fig. 9(b).

The orientation dependencies, in Figs. 9(a) and (b), follow roughly the same trend and are little affected by the pillar size and strain. The measured and power law fitted values in Fig. 9(a) follow the same $\tau_{2.5\%}$–χ relation, with the exeption of the smallest pillars ($D_{\rm t}^{\rm avg} = 134$ nm). However, small differences and inaccuracies are expected in the mesured values since the sets of pillars differ slightly in size for different orientations. On the other hand, the curve fitted values might not give a very accurate measurment over the whole size range. When normalising τ in Fig. 9 to $\tau_{[\bar{1}49]}$ (with the apropriate size or strain), and only excluding the data for the smallest pillars ($D_{\rm t} < 200$ nm), we obtain the ratios:

$$\begin{aligned}
\tau_{[001]}/\tau_{[\bar{1}49]} &= 1.05 \pm 0.09\\
\tau_{[\bar{2}35]}/\tau_{[\bar{1}49]} &= 0.86 \pm 0.06\\
\tau_{[011]}/\tau_{[\bar{1}49]} &= 0.64 \pm 0.07\\
\tau_{[\bar{1}11]}/\tau_{[\bar{1}49]} &= 0.68 \pm 0.07
\end{aligned}$$

Notice that the standard deviations was calculated from averaged and curve fitted values in Fig. 9, hence, they will not fully capture the scatter.

Deformation of bcc metals is known to be complex and does not follow Schmid's law (see for instance Refs. [46–51]). A known deviation from Schmid's law is that the resistance against slip is affected by both the stress conditions and the direction of slip. The observed behaviour is attributed to the properties of the screw dislocations in the bcc crystal structure. During loading of the crystal the core of the screw dislocations with a Burgers vector $\mathbf{b} = 1/2\,\langle 111\rangle$ is influenced by non-glide stresses. The non-glide stresses cannot induce dislocation glide, however, they may modify the core structure and the stresses necessary to drive the motion of the dislocations. In addition, since the $\{111\}$ planes in the bcc crystal are not mirror planes, the dislocation slip along two opposite directions are not generally equivalent and gives rise to the so-called twinning–antitwinning slip asymmetry.

The twinning–antitwinning asymmetry is recognized in Fig. 9, where τ is higher when the crystal is loaded in the antitwinning direction ($\chi < 0$) compared to the twinning direction ($\chi > 0$). When comparing our results to the work of Aono et al. [41], the pillars show decreasing τ as χ increases, while Aono et al. [41] observed a nearly constant shear stress for samples loaded in twinning directions at room temperature. The recent atomistic simulation results by Chen et al. [51] predicts the

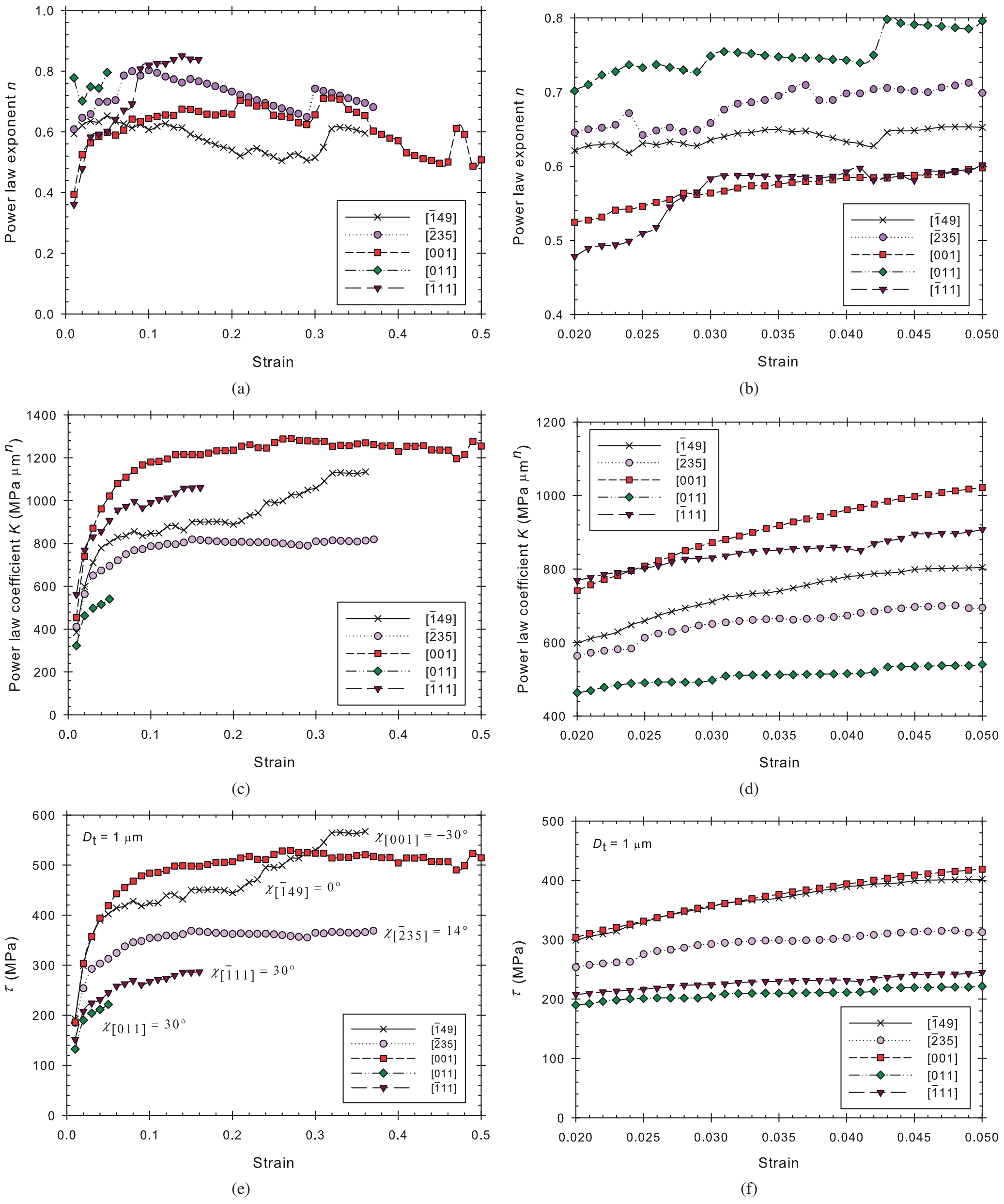

(a) (b) (c) (d) (e) (f)

Figure 8: Plot of (a) the power law exponent n, (c) the power law coefficient K and (e) the shear stress τ, resolved to the $(\bar{1}01)[111]$ slip system, as a function of strain. τ were calculated from Eq. (3) by using D_t = 1 μm and the fitted parameters n and K in the calculations. Plot (b), (d) and (f) shows details at low levels of strain from plot (a), (c) and (e), respectively.

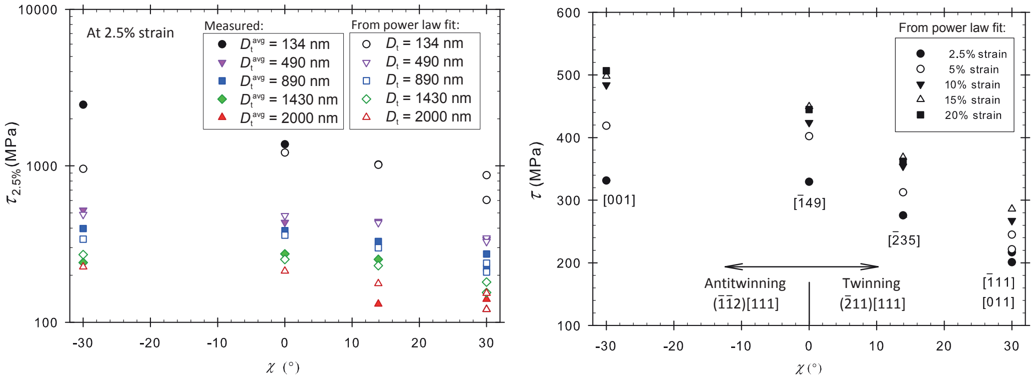

(a) (b)

Figure 9: Relation between the resolved shear stress (τ) and χ for different (a) diameters and (b) strains. The measured values (filled symbols in (a)) was calculated by Eq. (2) from data in Fig. 6(a), where groups of similar pillar sizes were averaged into average stresses ($\sigma_{2.5\%}^{avg}$) and average pillar diameters (D_t^{avg}). The open symbols in (a) and all symbols in (b) were calculated by Eq. (3) with D_t = 1 µm and curve fitted values presented in Fig. 8.

behaviour of the 1/2⟨111⟩ screw dislocation in iron at finite temperature. The atomistic study confirms the importance of the non-glide stresses that change the core structure of the screw dislocation. The changes of the core both increase the stresses necessary to drive the dislocation motion and can also activate deformation on less stressed planes. However, more investigations are necessary to understand the twinning–antitwinning asymmetry as observed in Fig. 9.

5. Conclusions

Pillars with 4 crystallographic orientations from a polycrystalline iron sample were prepared by focused ion beam milling (FIB) and tested in a nanoindentation system. The slip traces on the pillar surface were analysed to determine the operating slip system. Furthermore, the size dependency of the stress–strain curves and flow stresses were evaluated. The power law constants, K and n, as a function of strain was evaluated.

From the slip trace analysis it was concluded that the slip traces most frequently corresponded to slip along the ($\bar{1}$01)[111] slip system for orientation [$\bar{1}$49], [$\bar{2}$35], [001] and [011]. The secondary (101)[$\bar{1}$11] slip system was observed for orientation [$\bar{1}$49].

The size dependency of the flow stresses followed a power law where the power law coefficient n were typically between 0.5–0.8. The power law coefficient K advanced similar to a flow curve as a function of strain, i.e., it underwent strain hardening like behaviour. The K–strain curves were similar in shape for the different loading direction, but varied in magnitude.

The shear stress resolved to the ($\bar{1}$01)[111] slip system showed an orientation dependent relation. Orientations where the resolved shear stress was highest on the ($\bar{1}\bar{1}$2)[111] antitwinning system obtained the highest stresses, while orientations where ($\bar{2}$11)[111] twinning system obtained significantly lower resolved shear stresses. Pillar size and strain appeared to have little effect on the twinning–antitwinning asymmetry.

Acknowledgments

The authors gratefully acknowledge M.Sc. Veronica Haugen for the preparation and testing of the initial pillars. Further we would like to thank Prof. Odd Magne Akselsen and Dr. Inga Gudem Ringdalen from SINTEF and Dr. Afrooz Barnoush from NTNU for interesting discussions. We further acknowledge the cooperation with Saarland University in Germany and for assistance and help with heat-treatment and electropolishing of samples. One of the authors (B.R.S. Rogne) wishes to thank NTNU for the funding of his Ph.D. work. The Research Council of Norway is acknowledged for the support to the Norwegian Micro- and Nano-Fabrication Facility, NorFab (197411/V30).

References

[1] T. L. Altshuler, J. W. Christian, Phil. Trans. R. Soc. Lond. A 261 (1967) 253–287.

[2] D. F. Stein, J. R. Low Jr, Acta Metall. 14 (1966) 1183–1194.
[3] W. Spitzig, A. Keh, Metall. Mater. Trans. B 1 (1970) 2751–2757.
[4] J. W. Christian, Metall. Trans. A 14 (1983) 1237–1256.
[5] M. D. Uchic, D. M. Dimiduk, J. N. Florando, W. D. Nix, Science 305 (2004) 986–989.
[6] M. D. Uchic, D. A. Dimiduk, Mater. Sci. Eng. A 400 (2005) 268–278.
[7] J. R. Greer, W. C. Oliver, W. D. Nix, Acta Mater. 53 (2005) 1821–1830.
[8] M. D. Uchic, P. A. Shade, D. M. Dimiduk, Ann. Rev. Mater. Res. 39 (2009) 361–386.
[9] O. Kraft, P. A. Gruber, R. Mönig, D. Weygand, Ann. Rev. Mater. Res. 40 (2010) 293–317.
[10] R. Krahne, G. Morello, A. Figuerola, C. George, S. Deka, L. Manna, Phys. Rep. 501 (2011) 75–221.
[11] J. R. Greer, J. T. M. De Hosson, Prog. Mater. Sci. 56 (2011) 654–724.
[12] T. A. Parthasarathy, S. I. Rao, D. M. Dimiduk, M. D. Uchic, D. R. Trinkle, Scr. Mater. 56 (2007) 313–316.
[13] J. R. Greer, W. D. Nix, Phys. Rev. B 73 (2006) 245410/1–6.
[14] D. Kiener, A. M. Minor, Nano Lett. 11 (2011) 3816–3820.
[15] D. M. Dimiduk, M. D. Uchic, T. A. Parthasarathy, Acta Mater. 53 (2005) 4065–4077.
[16] C. A. Volkert, E. T. Lilleodden, Phil. Mag. 86 (2006) 5567–5579.
[17] Z. W. Shan, R. K. Mishra, S. A. S. Asif, O. L. Warren, A. M. Minor, Nat. Mater. 7 (2008) 115–119.
[18] J. R. Greer, C. R. Weinberger, W. Cai, Mater. Sci. Eng. A 493 (2008) 21–25.
[19] C. P. Frick, B. G. Clark, S. Orso, A. S. Schneider, E. Arzt, Mater. Sci. Eng. A 489 (2008) 319–329.
[20] S. Brinckmann, J. Y. Kim, J. R. Greer, Phys. Rev. Lett. 100 (2008) 155502/1–4.
[21] D. Kiener, A. M. Minor, Acta Mater. 59 (2011) 1328–1337.
[22] D. Kiener, Z. Zhang, S. Sturm, S. Cazottes, P. J. Imrich, C. Kirchlechner, G. Dehm, Philos. Mag. 92 (2012) 3269–3289.
[23] A. S. Schneider, D. Kiener, C. M. Yakacki, H. J. Maier, P. A. Gruber, N. Tamura, M. Kunz, A. M. Minor, C. P. Frick, Mater. Sci. Eng. A 559 (2013) 147–158.
[24] J. Y. Kim, J. R. Greer, Appl. Phys. Lett. 93 (2008) 101916/1–3.
[25] J.-Y. Kim, D. Jang, J. R. Greer, Scr. Mater. 61 (2009) 300–303.
[26] J.-Y. Kim, J. R. Greer, Acta Mater. 57 (2009) 5245–5253.
[27] A. S. Schneider, B. G. Clark, C. P. Frick, P. A. Gruber, E. Arzt, Mater. Sci. Eng. A 508 (2009) 241–246.
[28] A. S. Schneider, D. Kaufmann, B. G. Clark, C. P. Frick, P. A. Gruber, R. Monig, O. Kraft, E. Arzt, Phys. Rev. Lett. 103 (2009) 105501/1–4.
[29] S. Shim, H. Bei, M. K. Miller, G. M. Pharr, E. P. George, Acta Mater. 57 (2009) 503–510.
[30] A. S. Schneider, B. G. Clark, C. P. Frick, P. A. Gruber, E. Arzt, Philos. Mag. Lett. 90 (2010) 841–849.
[31] J.-Y. Kim, D. Jang, J. R. Greer, Acta Mater. 58 (2010) 2355–2363.
[32] S. M. Han, T. Bozorg-Grayeli, J. R. Groyes, W. D. Nix, Scr. Mater. 63 (2010) 1153–1156.
[33] A. S. Schneider, C. P. Frick, B. G. Clark, P. A. Gruber, E. Arzt, Mater. Sci. Eng. A 528 (2011) 1540–1547.
[34] D. Kaufmann, R. Mönig, C. A. Volkert, O. Kraft, Int. J. Plast. 27 (2011) 470–478.
[35] L. Huang, Q. J. Li, Z. W. Shan, J. Li, J. Sun, E. Ma, Nat. Commun. 2 (2011) 1–6.
[36] J.-Y. Kim, D. Jang, J. R. Greer, Int. J. Plast. 28 (2012) 46–52.
[37] J. L. Stewart, L. Jiang, J. J. Williams, N. Chawla, Mater. Sci. Eng. A 534 (2012) 220–227.
[38] S. M. Han, G. Feng, J. Y. Jung, H. J. Jung, J. R. Groves, W. D. Nix, Y. Cui, Appl. Phys. Lett. 102 (2013) 041910/1–5.
[39] B. R. S. Rogne, C. Thaulow, (Submitted to Philos. Mag.) (2014).
[40] C. R. Weinberger, W. Cai, Proc. Natl. Acad. Sci. U. S. A. 105 (2008) 14304–14307.
[41] Y. Aono, E. Kuramoto, K. Kitajima, Rep. Res. Inst. Appl. Mech. (Kyushu University) 29 (1981) 127–193.
[42] D. Caillard, Acta Mater. 58 (2010) 3493–3503.
[43] G. I. Taylor, Proc. R. Soc. Lond. A 118 (1928) 1–24.
[44] G. Taylor, Prog. Mater. Sci. 36 (1992) 29–61.
[45] N. Kheradmand, H. Vehoff, Adv. Eng. Mater. 14 (2012) 153–161.
[46] D. Hull, D. J. Bacon, Introduction to Dislocations, Butterworth-Heinemann, Oxford, 4 edition, 2001.
[47] K. Ito, V. Vitek, Philos. Mag. A 81 (2001) 1387–1407.
[48] V. Vitek, M. Mrovec, J. L. Bassani, Mater. Sci. Eng. A 365 (2004) 31–37.
[49] V. Vitek, M. Mrovec, R. Gröger, J. L. Bassani, V. Racherla, L. Yin, Mater. Sci. Eng. A 387-389 (2004) 138–142.
[50] C. R. Weinberger, B. L. Boyce, C. C. Battaile, Int. Mater. Rev. 58 (2013) 296–314.
[51] Z. M. Chen, M. Mrovec, P. Gumbsch, Modell. Simul. Mater. Sci. Eng. 21 (2013) 055023/1–18.